

rβ2-subunit alternative splicing stabilizes Cav2.3 Ca²⁺ channel activity during continuous midbrain dopamine neuron-like activity

Anita Siller¹, Nadja T. Hofer¹, Giulia Tomagra³, Nicole Wiederspohn⁴, Simon Hess⁵, Julia Benkert⁴, Aisylu Gaifullina⁴, Desiree Spaich⁴, Johanna Duda⁴, Christina Pötschke⁴, Kristina Vilusic¹, Eva Maria Fritz¹, Toni Schneider², Peter Kloppenburg⁵, Birgit Liss⁴, Valentina Carabelli³, Emilio Carbone³, Nadine J. Ortner^{1*} and Jörg Striessnig^{1*}

¹Department of Pharmacology and Toxicology, Institute of Pharmacy, Center for Molecular Biosciences Innsbruck, University of Innsbruck, Innsbruck, Austria;

²Institute of Neurophysiology, University of Cologne, Cologne, Germany;

³Department of Drug Science, NIS Centre, University of Torino, Torino, Italy;

⁴Institute of Applied Physiology, University of Ulm, Ulm, Germany; Linacre College & New College, University of Oxford, Oxford, UK

⁵Institute for Zoology, Biocenter, CECAD, University of Cologne, Cologne, Germany.

***Correspondence:**

Nadine J. Ortner (nadine.ortner@uibk.ac.at; +43-512-507-58815) or Jörg Striessnig (jorg.striessnig@uibk.ac.at; +43-512-507-58800)

Keywords: Cav2.3, R-type Ca²⁺ channel, β-subunits, alternative splicing, dopaminergic neurons, Parkinson's disease

Number of words: 12010

Number of figures: 7 (plus 6 figure supplements)

Abstract

In dopaminergic (DA) substantia nigra (SN) neurons Cav2.3 R-type Ca^{2+} -currents contribute to somatodendritic Ca^{2+} -oscillations. This activity may contribute to the selective degeneration of these neurons in Parkinson's disease (PD) since Cav2.3-knockout is neuroprotective in a PD mouse model. Here we show that in tsA-201-cells the membrane-anchored β 2-splice variants β 2a and β 2e are required to stabilize Cav2.3 gating properties allowing sustained Cav2.3 availability during simulated pacemaking and enhanced Ca^{2+} -currents during bursts. We confirmed the expression of β 2a- and β 2e-subunit transcripts in the mouse SN and in identified SN DA neurons. Patch-clamp recordings of mouse DA midbrain neurons in culture and SN DA neurons in brain slices revealed SNX-482-sensitive R-type Ca^{2+} -currents with voltage-dependent gating properties that suggest modulation by β 2a- and/or β 2e-subunits. Thus, β -subunit alternative splicing may prevent a fraction of Cav2.3 channels from inactivation in continuously active, highly vulnerable SN DA neurons, thereby also supporting Ca^{2+} signals contributing to the (patho)physiological role of Cav2.3 channels in PD.

46

47

48 Introduction

49 Parkinson's disease (PD) is one of the most common neurodegenerative disorders. Its motor
 50 symptoms are characterized by progressive degeneration of dopamine (DA)-releasing
 51 neurons in the substantia nigra (SN), while neighboring DA neurons in the ventral tegmental
 52 area (VTA) remain largely unaffected (Damier et al., 1999; Giguere et al., 2018; Surmeier et
 53 al., 2017). Current PD therapy is only symptomatic and primarily based on the substitution of
 54 striatal DA by administration of L-DOPA or dopamine D2 receptor agonists. Unfortunately,
 55 none of the existing therapeutic approaches for PD patients is disease-modifying and can
 56 prevent disease progression (for review see Liss & Striessnig, 2019; Surmeier et al., 2011;
 57 Surmeier et al., 2017).

58 The development of novel neuroprotective strategies for the treatment of early PD requires
 59 the understanding of the cellular mechanisms responsible for the high vulnerability of SN DA
 60 neurons. Among these mechanisms elevated metabolic stress appears to play a central role
 61 (for review see Liss & Striessnig, 2019), eventually triggering lysosomal, proteasomal and
 62 mitochondrial dysfunction (Burbulla et al., 2017; Surmeier et al., 2017). Intrinsic physiological
 63 properties of SN DA neurons, in particular increased cytosolic DA levels and high energy
 64 demand due to large axonal arborisation favour metabolic stress (Bolam & Pissadaki, 2012;
 65 Liss & Striessnig, 2019). In addition, these neurons must handle a constant intracellular Ca^{2+} -
 66 load resulting from dendritic and somatic Ca^{2+} -oscillations triggered during their continuous
 67 electrical activity (Ortner et al., 2017; Surmeier et al., 2011). Dendritic Ca^{2+} -transients largely
 68 depend on the activity of voltage-gated Ca^{2+} channels, in particular Cav1.3 L-type (LTCCs)
 69 and T-type channels (Guzman et al., 2018). Cav1.3 channels can activate at subthreshold
 70 membrane potentials (Koschak et al., 2001; Lieb et al., 2014; Xu & Lipscombe, 2001) and do
 71 not completely inactivate during continuous pacemaking activity (Guzman et al., 2018;
 72 Guzman et al., 2009; Ortner et al., 2017). Some, but not all, in vivo studies (Liss & Striessnig,
 73 2019) showed neuroprotection by the systemic administration of dihydropyridine (DHP)
 74 LTCC blockers in 6-OHDA and MPTP animal models of PD thus further supporting a role of
 75 LTCCs as potential neuroprotective drug target. Based on these preclinical data and
 76 supporting observational clinical evidence (Liss & Striessnig, 2019), the neuroprotective
 77 potential of the DHP isradipine (ISR) was tested in a double-blind, placebo-controlled,
 78 parallel-group phase 3 clinical trial ("STEADY-PD III", NCT02168842; Biglan et al., 2017).
 79 This trial reported no evidence for neuroprotection by ISR. Several explanations have been
 80 offered for this negative outcome (Investigators, 2020). One likely explanation is that voltage-
 81 gated Ca^{2+} -channels (Cavs) other than LTCCs also contribute to Ca^{2+} -transients in SN DA
 82 neurons. This is supported by the observation that only about 50% of the Ca^{2+} -transients are
 83 blocked by ISR in the dendrites of SN DA neurons (Guzman et al., 2018) and that action
 84 potential-associated Ca^{2+} -transients in the soma appear to be even resistant to ISR (Ortner

et al., 2017). Therefore, in addition to L-type, other types of Caves expressed in SN DA neurons (Branch et al., 2014; Evans et al., 2017; Philippart et al., 2016) may also contribute to Ca^{2+} -induced metabolic stress in SN DA neurons. Cav2.3 (R-type) Ca^{2+} -channels are very promising candidates. We have recently shown that SN DA neurons in mice lacking Cav2.3 channels were fully protected from neurodegeneration in the chronic MPTP-model of PD. Moreover, we found that Cav2.3 is the most abundant Cav expressed in SN DA neurons, and substantially contributes to activity-related somatic Ca^{2+} -oscillations (Benkert et al., 2019). These findings make Cav2.3 R-type Ca^{2+} channels a promising target for neuroprotection in PD.

SN DA neurons are spontaneously active, pacemaking neurons, either firing in a low-frequency single-spike mode or transiently in a high-frequency burst mode (Grace & Bunney, 1984; Paladini & Roeper, 2014). During regular pacemaking their membrane potential is, on average, rather depolarized ranging from about -70 mV after an action potential (AP) to about -40 mV at firing threshold (Gantz et al., 2018; Guzman et al., 2018; Ortner et al., 2017). The contribution of a particular Cav channel to Ca^{2+} -entry is largely determined by its steady-state inactivation properties, which determines its availability at these depolarized voltages. Therefore, in SN DA neurons steady-state inactivation of Cav2.3 channels must occur within a voltage-range preventing inactivation of a substantial fraction of channels during the positive operating range of these continuously firing neurons. However, Cav2.3 $\alpha 1$ -subunits have originally been cloned as a low-voltage gated channel with a negative steady-state inactivation voltage range ($V_{0.5, \text{inact}}$ -78 mV; Soong et al., 1993) with almost complete inactivation at voltages positive to -50 mV. Interestingly, SNX-482-sensitive R-type currents mediated by Cav2.3 $\alpha 1$ subunits (Newcomb et al., 1998) recorded from different neuronal cell types reveal a wide voltage range of steady-state inactivation despite similar recording conditions (5-10 mM Ba^{2+} as charge carrier): half-maximal voltages for steady-state inactivation ($V_{0.5, \text{inact}}$) range from -90 to -70 mV in cerebellar, cortical and myenteric neurons (Bian et al., 2004; Sochivko et al., 2002; Tottene et al., 2000) to -58 mV in neurohypophyseal terminals (Wang et al., 1999) and to even as positive as -40 mV in GnRH-releasing neurons or GT1-7 cells (Kato et al., 2003; Watanabe et al., 2004). This raises the important question about potential molecular mechanisms accounting for this heterogeneity and its role for stabilization of R-type currents in SN DA neurons.

While alternative splicing of Cav2.3 $\alpha 1$ subunits is unlikely to account for such large shifts in steady-state inactivation (Pereverzev et al., 2002), accessory β -subunits appear as obvious candidates for several reasons. First, like for other high-voltage-activated Ca^{2+} channels (including Cav2.1 and Cav2.2, Liu et al., 1996; Scott et al., 1996) they form part of the Cav2.3 channel complex and thus affect its membrane targeting and gating properties (Zamponi et al., 2015). Second, previous work has shown that β -subunits tightly control

$V_{0.5,inact}$ of Cav2 channels, including Cav2.3. While all cytosolic β -subunit isoforms ($\beta 1 - \beta 4$ and cytosolic splice variants of $\beta 2$) induce steady-state inactivation at negative potentials, being almost complete at voltages positive to -50 mV, the membrane-anchored $\beta 2$ subunit splice variants $\beta 2a$ and $\beta 2e$ induce strong positive shifts of $V_{0.5,inact}$ of Cav2.3 channels and slow the time course of voltage-dependent inactivation (Jones et al., 1998; Pereverzev et al., 2002; Soong et al., 1993; Williams et al., 1994; Yasuda et al., 2004). However, a specific physiological role for this modulatory effect has so far not been reported and the relative abundance of $\beta 2a$ and $\beta 2e$ subunits in neurons, including SN DA neurons, is unknown.

Here we directly addressed the question if association of Cav2.3 channels with $\beta 2a$ or $\beta 2e$ but not with cytosolic β -subunits can prevent channel inactivation during SN DA activity patterns and could therefore serve as a mechanism allowing these channels to contribute to SN DA function. When co-expressed together with auxiliary $\alpha 2\delta 1$ -subunits in tsA-201 cells we indeed found that during simulated SN DA neuron-like continuous tonic pacemaking or brief burst activity (Ortner et al., 2017) Cav2.3 channels remained active only when associated with $\beta 2a$ or $\beta 2e$, but not the cytosolic $\beta 3$ and $\beta 4$ subunits. In contrast, steady-state inactivation of Cav1.3 channels was largely unaffected by $\beta 2a$, suggesting that Cav1.3 availability is much less dependent on the presence of $\beta 2a$ subunits. Using RNAScope we confirmed the presence of both, $\beta 2a$ and $\beta 2e$ transcripts in identified mouse SN and VTA DA neurons and quantitative PCR analysis showed that $\beta 2$ -subunits represent about 25% of all β -subunit transcripts in the mouse SN and VTA with about 50% comprising $\beta 2a$ and $\beta 2e$ variants. In patch-clamp recordings of SN DA neurons in mouse brain slices we detected SNX-482-sensitive R-type Ca^{2+} -currents with voltage-dependent inactivation properties suggesting a contribution of $\beta 2a$ - or $\beta 2e$ -stabilized Cav2.3-currents. Recordings in cultured DA midbrain neurons confirmed R-type current activity during the pacemaking cycle. Taken together, our data further support a role of Cav2.3 in SN DA neuron Ca^{2+} -signaling and imply a potential (patho)physiological role of β -subunit alternative splicing.

Results

To explore how Cav2.3 channels can contribute to DA neuron Ca^{2+} -entry during sustained neuronal activity we expressed Cav2.3 $\alpha 1$ -subunits together with its accessory $\alpha 2\delta 1$ and different β -subunits in tsA-201 cells under near-physiological conditions (Figure 1). For this purpose we employed physiological extracellular Ca^{2+} (2 mM), weak intracellular Ca^{2+} -buffering (0.5 mM EGTA, see methods), and, in addition to square pulse protocols, used typical AP waveforms previously recorded from SN DA neurons in mouse midbrain slices (2.5 Hz) or simulated bursts as command voltages as described (Ortner et al., 2017; see methods). Moreover, we specifically employed the Cav2.3e $\alpha 1$ -subunit splice variant for our recordings, which among the 6 major Cav2.3 $\alpha 1$ -subunit splice variants, was the only one detected in UV laser-microdissected mouse SN DA neurons in experiments using a qualitative single-cell RT-qPCR approach (Figure 1-figure supplement 1A,B).

β -subunit isoform-dependent regulation of Cav2.3 channel gating

We first used standard square pulse protocols to quantify the effect of different β -subunits on the voltage-dependence of channel gating under our experimental conditions. In addition to $\beta 3$, $\beta 4$, and $\beta 2a$ analyzed in previous studies (Jones et al., 1998; Yasuda et al., 2004), we also included membrane-anchored $\beta 2e$ and $\beta 2d$, a cytosolic $\beta 2$ splice variant, in our head-to-head comparison (Figure 1). In agreement with earlier studies (Jones et al., 1998; Yasuda et al., 2004), we found that recombinant Cav2.3 channels when associated with cytosolic $\beta 3$ or $\beta 4$ subunits inactivate at negative voltages ($V_{0.5, \text{inact}} < -70$ mV) and with a rapid inactivation time course ($\geq 50\%$ within 50 ms, Figure 1B-C, Table 1). The cytosolic $\beta 2d$ splice variant also showed a gating behavior very similar to $\beta 4$. In contrast, $\beta 2a$, which is anchored to the plasma membrane through N-terminal palmitoylation, slowed the inactivation time course and shifted Cav2.3 voltage-dependent inactivation by ~ 30 mV to more positive potentials compared to $\beta 4$ (and $\beta 3$). Likewise, with co-expressed $\beta 2e$, which is membrane anchored through N-terminal phospholipid interaction (Buraei & Yang, 2010; Miranda-Laferte et al., 2014), gating properties were similar to $\beta 2a$ -containing Cav2.3 channel complexes (Figure 1A-C, Table 1). In the case of $\beta 2a$, the shift in the voltage-dependence of inactivation, but not the slowing of the inactivation time course, was largely dependent on N-terminal palmitoylation as shown with the palmitoylation-deficient mutant $\text{C3S/C4S}\beta 2a$ (Figure 1-figure supplement 2). The voltage-dependence of activation was similar for all tested β -subunits (Figure 1A, Table 1). Due to the voltage-dependent inactivation at more depolarized potentials and the resulting overlap of the steady-state activation and inactivation curves (Figure 1B), $\beta 2a$ and $\beta 2e$ subunits induce window currents, i.e. steady-state Ca^{2+} influx, at negative potentials (Figure 1D). Our findings confirm and extend previous observations that

membrane-anchored $\beta 2$ subunits give rise to slowly inactivating Cav2.3 currents available at more positive voltages that could participate in the formation of such SNX-482-sensitive current components in neurons.

Since Cav2.3 $\alpha 1$ -subunits have also been reported to mediate I_{Ca} even when expressed in the absence of β -subunits (Jones et al., 1998; Yasuda et al., 2004) we also tested to which extent β -subunit modulated channels are expected to contribute to Cav2.3 currents. In our experiments, all five tested β -subunits ($\beta 2a$, $\beta 2d$, $\beta 2e$, $\beta 3$, $\beta 4$) caused a robust and highly significant (6-12-fold; Figure 1A, Table 1) increase in current densities. This implies that β -associated Cav2.3 channels contribute more to overall Cav2.3-mediated currents than channel complexes devoid of β -subunits and thus can be subject to differential modulation by β -subunits.

Taken together, these data suggest that through their effect on inactivation gating $\beta 2a$ - and $\beta 2e$ -subunits could contribute to sustained Cav2.3 activity and AP-associated Ca^{2+} transients previously recorded in SN DA neurons (Benkert et al., 2019).

β -subunit transcripts in mouse SN and VTA

This prompted us to investigate if $\beta 2a$ and $\beta 2e$ splice variants are indeed expressed in SN tissue. First, we investigated $\beta 1$ - $\beta 4$ subunit expression patterns in the SN (and VTA for comparison, Figure 2A) dissected from brain slices of 12-14 weeks old male C57Bl/6N mice (Figure 2C) using a standard curve-based absolute RT-qPCR assay (Schlick et al., 2010; Figure 2-figure supplement 1, Supplementary files 1-3). In both SN and VTA tissue $\beta 4$ (SN: ~64%; VTA: ~57%) and $\beta 2$ (SN: ~27%; VTA: ~29%) represented the most abundant β -subunit transcripts, followed by $\beta 1$ and $\beta 3$ (~4 - 7%) (Figure 2A). Our findings are in excellent agreement ($\beta 2$: 31-35%, $\beta 4$: 41-45%) with cell-type specific RNA sequencing data from identified mouse midbrain DA neurons (Brichta et al., 2015; Shin, 2015).

Since the relative abundance of $\beta 2$ -subunit splice variants in the brain is unknown, we used our standard curve-based RT-qPCR assay to specifically quantify their expression in the SN and VTA (Figure 2B; for alignment of N-terminal $\beta 2$ splice variants see Figure 2-figure supplement 1A). Assays were designed to specifically discriminate between $\beta 2a$, $\beta 2b$, and $\beta 2e$. $\beta 2c$ and $\beta 2d$ N-termini were detected together (the $\beta 2d$ N-terminus is also present in $\beta 2c$ but with different alternative splicing in the HOOK region; Buraei & Yang, 2010; see methods). In SN and VTA, $\beta 2a$ (~30%) and $\beta 2e$ (~26%) transcripts together comprised about half of all tested $\beta 2$ -subunit splice variants, cytosolic $\beta 2c$ and $\beta 2d$ -species about 42% and $\beta 2b$ only about 3% (Figure 2B). Therefore, $\beta 2a$ and $\beta 2e$ together should be able to form a substantial fraction of Cav2.3 channel complexes in these neurons.

We further confirmed the presence of the various N-terminal $\beta 2$ splice variants in individual UV-laser microdissected mouse SN DA neurons at the mRNA level using a qualitative PCR approach (Figure 2-figure supplement 2, Supplementary files 4 and 5). Moreover, quantitative RNAScope analysis confirmed the expression of $\beta 2e$ and $\beta 2a$ in identified mouse SN and VTA DA neurons with $\beta 2e$ more abundantly expressed compared to $\beta 2a$ (Figure 2-figure supplement 2B).

$\beta 2$ splice variant-dependent regulation of Cav2.3 activity during SN DA neuron-like regular pacemaking activity

To test a possible role of β -subunits for Cav2.3 channel availability in SN DA neurons, we mimicked their electrical activity in tsA-201 cells because individual Ca^{2+} -current components arising from Cav2.3 channel complexes associated with different β -subunits or even different splice variants cannot be isolated during continuous pacemaking in patch-clamp recordings of identified SN DA neurons. With co-expressed $\beta 3$ and $\beta 4$ isoforms simulated SN DA neuron regular pacemaker activity (initiated from a holding potential, hp, of -89 mV) induced large inward currents in response to single AP waveforms (Figure 3A,B). Cav2.3 channels conducted I_{Ca} during the repolarization phase of the AP (I_{AP}) without evidence for inward current during the interspike interval (ISI, Figure 3A,B bottom inset). However, I_{AP} decreased rapidly during continuous activity and almost completely disappeared after 1 (co-transfected $\beta 3$) - 2 min (co-transfected $\beta 4$; Figure 3A,B,E,F). The time course of I_{AP} decrease was best fitted by a bi-exponential function (see legend to Figure 3). Our data, therefore, suggest that Cav2.3e $\alpha 1$ -subunits, in complex with $\alpha 2\delta 1$ and $\beta 3$ or $\beta 4$, cannot support substantial inward currents during continuous SN DA neuron pacemaking activity. This is in contrast to our previously published finding of stable Cav1.3 Ca^{2+} -channel activity persisting under near identical experimental conditions (Cav1.3 $\alpha 1/\alpha 2\delta 1/\beta 3$ previously published data; Ortner et al., 2017; illustrated for comparison in Figure 3E,F, in grey).

In contrast, the depolarizing shifts in steady-state inactivation and the slowing of inactivation kinetics by $\beta 2a$ and $\beta 2e$ subunits are sufficient to stabilize Cav2.3e currents during simulated regular pacemaking activity. When analyzed in parallel under identical experimental conditions I_{AP} decreased with a much slower time course with about 40% of the maximal initial I_{AP} still remaining even after 5 min of continuous activity (Figure 3C-F). The time course of I_{AP} decrease could be fitted by a bi-exponential function predicting a steady-state reached at $32.3 \pm 0.77\%$ ($n=12$) of the initial I_{AP} for $\beta 2a$ and $25.0 \pm 0.12\%$ ($n=9$) for $\beta 2e$ (see legend to Figure 3). Similar to co-transfected $\beta 3$ or $\beta 4$ subunits, $\beta 2a$ or $\beta 2e$ supported Cav2.3 I_{Ca} predominantly during the repolarization phase after the AP spike. However, in accordance with enhanced window currents at negative voltages (Figure 1D) these subunits also

supported an inward current during the interspike interval (ISI) as evident from the first few sweeps (with the largest current amplitudes) (Figure 3C,D, bottom insets). I_{AP} persisting after 2 min ($\beta 3$, $\beta 4$) or 5 min ($\beta 2a$, $\beta 2e$) of pacemaking was completely blocked by 100 μM Cd^{2+} with almost complete recovery upon washout (Figure 3A-E).

Irreversible loss of I_{Ca} , a phenomenon also known as current "run-down" widely described for both native and recombinant Caves (Kepplinger et al., 2000; Ortner et al., 2017; Schneider et al., 2018) during patch-clamp recordings, may also contribute to the current decay observed during simulated pacemaking. We, therefore, quantified the contribution of current run-down for Cav2.3 co-expressed with $\alpha 2\delta 1$ and $\beta 2a$ or $\beta 3$ subunits first by applying short (20 ms) square pulses to V_{max} (hp -89 mV) with a frequency of 0.1 Hz (Figure 4A). With this protocol (short pulse, long inter-sweep interval, hyperpolarized hp) activity- and voltage-dependent inactivation of Cav2.3 channels should be minimized. While $\beta 3$ co-transfected Cav2.3 channels showed a time-dependent current run-down to about 60% of the peak I_{Ca} after 5 min, $\beta 2a$ prevented the current decline during this period (Figure 4A). To further quantify the current run-down during simulated pacemaking we interrupted the pacemaking protocol after different time periods by 20 s long pauses at -89 mV to allow channel recovery from inactivation (Figure 4B). Thus, the percent run-down can be estimated from the non-recovering current component (Figure 4B, horizontal dashed lines). After 30 s of pacemaking the current amplitude during the first AP after the pause was similar to I_{AP} during the initial AP with both β -subunits ($\beta 3$: $96.9 \pm 3.63\%$, 95% CI: 86.8-107.0, $n=5$, $N=2$; $\beta 2a$: $107.3 \pm 3.66\%$, 95% CI: 99.3-115.4, $n=12$, $N=2$, of the initial I_{AP}). After the pause that followed another 1 min of pacemaking, $83.6 \pm 7.33\%$ (95% CI: 63.2-103.9) of the initial current was still recovered with co-transfected $\beta 3$ but after 2 more minutes of pacemaking recovery decreased to $54.7 \pm 6.27\%$ (95% CI: 34.7-74.7, Figure 4B; $\sim 45\%$ run-down after 4.5 min in total, $n=5$). This time course is in good agreement with values obtained using the square-pulse protocol (Figure 4A). Again, run-down was largely prevented by co-expressed $\beta 2a$ -subunits (Figure 4B; $\sim 16\%$ run-down after 4.5 min in total, $n=12$).

These data clearly demonstrate that the I_{AP} decrease in response to simulated SN DA neuron pacemaking (2.5 Hz) is almost completely due to the reversible accumulation of Cav2.3 channels in inactivated states, an effect partially prevented by $\beta 2a$ and $\beta 2e$.

Cav2.3 Ca^{2+} currents during simulated SN DA burst firing activity

In addition to regular pacemaking activity (in vitro) or irregular single spike mode (in vivo), burst firing with transient increases in intracellular Ca^{2+} -load has been associated with neurodegeneration and selective neuronal vulnerability in Parkinson's disease (Dragicevic et

al., 2015; Schiemann et al., 2012). Thus, we investigated to which extent Cav2.3 Ca^{2+} -channels can contribute to Ca^{2+} -entry during bursts and after post-burst hyperpolarizing pauses of SN DA neurons. After reaching steady-state I_{AP} during simulated SN DA neuron pacemaking ($\beta 4$: 1-2 min, $\beta 2a/\beta 2e$: 5-6 min, see also Figure 3E,F) we applied a computer modeled typical three-spike burst, followed by a 1.5 s long afterhyperpolarization-induced pause at more negative potentials as a command voltage as previously described (Ortner et al., 2017) (Figure 5A). First, we quantified to which extent total burst Ca^{2+} -charge, i.e. I_{Ca} integrated over the duration of the burst, changes as compared to total Ca^{2+} -charge during the same duration of a single AP in steady-state (calculated as the mean of 3 APs preceding the burst). Integrated I_{Ca} during the burst was 4-6-fold higher than the mean integrated I_{Ca} during a steady-state AP with all co-expressed β -subunits ($\beta 2a$, $\beta 2e$, $\beta 4$) (Figure 5B, left panel). However, it has to be considered that with co-expressed $\beta 4$ only ~6% of the initial I_{AP} remained in steady-state during regular pacemaking (Figure 3E,F). Therefore, this relative increase will cause a much smaller rise in absolute Ca^{2+} charge compared to $\beta 2a/\beta 2e$ -associated Cav2.3 where ~40% of I_{AP} persisted in steady-state (Figure 5B, Figure 3E,F).

We also investigated if post-burst afterhyperpolarizations would allow Cav2.3 channels to recover from inactivation and thus mediate increased Ca^{2+} -entry during the first APs after the burst. We first determined the recovery from inactivation of Cav2.3 channels co-expressed with $\alpha 2\delta 1$ and $\beta 4$ or $\beta 2a$ using a square-pulse protocol (Figure 5C, Table 2; 1-s conditioning prepulse to V_{max} to inactivate Cav2.3 channels followed by a 10 ms step to V_{max} after different time periods at -89 mV). About 30% of currents recovered under these experimental conditions after 1.5 seconds at -89 mV with both co-expressed $\beta 4$ and $\beta 2a$ (~6-fold increase of the remaining I_{Ca} after 1s at V_{max}). In contrast, recovery during the hyperpolarizing pause after the burst of the AP protocol was much less pronounced ($\beta 4$) or absent ($\beta 2a$, $\beta 2e$) (Figure 5B, right panel). This may be due to the different pulse protocols inducing channel inactivation over different time periods and may stabilize inactivated states with different recovery times.

Taken together, these data predict that $\beta 2a$ - and $\beta 2e$ -associated Cav2.3 channels can contribute to enhanced Ca^{2+} -entry during brief burst activity but not during post-burst APs.

Steady-state activation and inactivation of R-type currents in mouse DA neurons

We have recently shown in whole-cell patch-clamp recordings that 100 nM SNX-482 inhibit ~30% of total Cav currents in mouse SN DA neurons (Benkert et al., 2019) when stimulated from a negative holding potential of -70 mV. If $V_{0.5,\text{inact}}$ of Cav2.3 channels in SN DA neurons is indeed stabilized at more positive potentials, then the voltage-dependent inactivation of the

R-type currents should allow a fraction of channels to be available even at voltages positive to -40 mV.

Using whole-cell patch-clamp recordings (Figure 6), we therefore measured the steady-state inactivation of R-type I_{Ca} in identified SN DA neurons in mouse midbrain slices. First, R-type current (i.e. current remaining after blocking other Cav channels) was isolated as reported in previous publications by preincubation of slices with selective inhibitors of Cav1 (1 μ M ISR), Cav2 (Cav2.1, Cav2.2; 1 μ M ω -conotoxin MVIIC) and Cav3 (10 μ M Z941) (Figure 6A, blue traces/symbols, see also methods section). R-type current evoked from -100 mV activated at ~8 mV more positive voltages than total I_{Ca} (Figure 6A, Table 3 for statistics). This observation is in accordance with the positive activation voltage range of Cav2.3e channels measured in tsA-201 cells. The R-type current $V_{0.5,inact}$ was ~5 mV more positive compared to total I_{Ca} (-47.5 mV vs. -52.7 mV; Figure 6A, Table 3) and therefore ~7 mV more negative than recombinant Cav2.3 currents expressed with β 2a or β 2e subunits (~ -40 mV, Table 1) and ~23-29 mV more positive than recombinant Cav2.3 currents expressed with β 4 or β 3. Since R-type currents may include current components not mediated by Cav2.3 (Newcomb et al., 1998; Sochivko et al., 2002; Tottene et al., 2000; Wilson et al., 2000), we also isolated SNX-482-sensitive currents, which must be mediated by Cav2.3 (Zamponi et al., 2015) by subtracting current remaining in the presence of SNX-482 from control current (Figure 6B). Although the slope of the voltage-dependence of activation was different for the SNX-482-sensitive current as compared to R-type current, steady-state inactivation was again observed at significantly more positive voltages as compared to control current (-44.6 mV vs. -52.9 mV, Figure 6B, Table 3), and ~5 mV more negative than recombinant Cav2.3 currents associated with β 4 or β 3 (Table 3). Although these experiments do not directly prove the contribution of β 2a and/or β 2e to R-type current in SN DA neurons, the strong requirement of β -subunits for Cav2.3 channel activity and the inability of other cytosolic β -subunit variants to account for the observed voltage-dependence of R-type current (Figure 1A,B) strongly suggests a contribution of these membrane-associated β -subunits for preventing complete inactivation of Cav2.3-mediated currents during typical activity patterns in these cells.

We independently also tested the availability of SNX-482-sensitive R-type currents at more depolarized voltages using perforated patch recordings (Figure 6-figure supplement 1), which allow very stable recordings in identified SN DA neurons ((Figure 6-figure supplement 1I,J). We held cells at a more positive holding potential of -60 mV, a voltage within the spontaneous depolarization phase of the ISI, where a substantial fraction of Cav2.3 channels must already be inactivated (Figure 6). Indeed, under these conditions still about 13% of the total I_{Ca} was inhibited by acute bath application of SNX-482 and inhibition was partially reversible upon washout (Figure 6-figure supplement 1A-D, Supplementary file 7). Under

these conditions about 10% of current were blocked reversibly by the L-type channel blocker nifedipine (10 μ M, Figure 6-figure supplement 1E-H).

To further confirm the presence of inactivation-resistant R-type currents, we also recorded SNX-482-sensitive Ca^{2+} currents elicited from a hp of -70 mV in primary cultures of mouse DA midbrain neurons after 8 – 9 days in vitro. When added after the complete block of LTCC currents by 3 μ M isradipine (comprising 24.7 ± 4.2 % of total Ca^{2+} -current, $n=15$), 100 nM SNX-482 significantly reduced non-LTCC currents by 41 ± 4 % (95% CI: 33-49, $n=20$, $N=4$, paired Student's t-test; $p<0.001$) (Figure 7A-D). All residual I_{Ca} components were blocked by adding 2 μ M Cd^{2+} to the bath solution (Figure 7A,B).

We also determined the voltage-dependence of steady-state activation (Figure 7E) and inactivation (Figure 7F) before (non-L, control) and during application of 100 nM SNX-482 and calculated parameters for the SNX-482-sensitive R-type current by subtracting the current resistant to 100 nM SNX-482 from the control current (legend to Figure 7 for details). SNX-482-sensitive currents (blue) activated with a half maximal activation voltage ($V_{0.5,\text{act}}$ - 9.2 ± 0.6 mV) slightly more positive than non-LTCC current ($V_{0.5,\text{inact}}$ = -12.5 ± 0.6 mV). To determine the steady-state inactivation, test pulses of 50 ms to 0 mV were preceded by 1 min prepulses to voltages from -80 to -10 mV (Figure 7F). SNX-482-sensitive current inactivation was best fit with a $V_{0.5,\text{inact}}$ of -58.1 ± 0.6 mV, which was 12-18 mV more positive than recombinant Cav2.3 currents expressed with $\beta 4$ or $\beta 3$ (Table 1). Despite an ~ 13 mV more negative inactivation range compared to SN DA neurons (Figure 6, Table 3), this still allowed substantial channel availability at voltages positive to -50 mV (Figure 7F, in contrast to currents with co-expressed cytosolic β -subunits (Figure 1D)).

Finally, we tested if SNX-482 also affects the spontaneous AP firing of these cultured midbrain neurons. In current-clamp recordings 100 nM SNX-482 significantly reduced the spontaneous firing frequency from 4.1 ± 0.8 Hz (control, $n=10$, $N=3$; 95% CI: 2.1-6.1) to 1.1 ± 0.2 Hz (SNX-482, $n=10$, 95% CI: 0.2-2.1, $p=0.0036$, paired Student's t-test; Figure 7-figure supplement 1A, B), decreased the regularity of pacemaking and also caused changes in AP shape (Figure 7-figure supplement 1A-C). Cav2.3-mediated currents may therefore also contribute to the pacemaking cycle in cultured DA neurons.

Discussion

Although the modulation of Caves by β -subunits and the characteristic gating changes induced by N-terminally membrane-anchored β 2-subunit splice variants have been well described in the literature, the physiological significance of these findings remained underexplored. Here we provide strong evidence for an important role of β -subunit alternative splicing for Cav2.3 Ca^{2+} -channel signaling during continuous SN DA neuron-like regular pacemaking activity. We show that only membrane-bound β 2a and β 2e stabilize Cav2.3 channel complexes with voltage-dependent inactivation properties preventing complete inactivation during the on-average depolarized membrane potentials encountered during the pacemaking cycle. This cannot only explain our previous finding of a substantial contribution of SNX-482-sensitive R-type currents to activity-dependent somatic Ca^{2+} -oscillations in SN DA neurons in brain slices (Benkert et al., 2019) but also to pacemaking in cultured DA neurons. We also provide evidence for the expression of β 2a and β 2e subunit splice variants in highly vulnerable mouse SN DA and in more resistant VTA DA neurons. Together with our finding that R-type currents in SN DA neurons are available within a voltage range more positive than expected for association with β 4-, β 3- or other cytosolic β 2-subunits, our data strongly suggest that β 2a and β 2e contribute to non-inactivating Cav2.3 R-type currents required for normal DA neuron function. This may therefore also be of pathophysiological relevance given the previously reported pathogenic potential of Cav2.3 Ca^{2+} -channels in PD pathophysiology (Benkert et al., 2019).

The large shift of $V_{0.5, \text{inact}}$ of Cav2.3 R-type current by membrane-anchored β 2a and β 2e subunits would predict that Cav2.3 channel availability can be adjusted along a wide range of potentials (about 30 mV; $V_{0.5, \text{inact}}$ -40 to -70 mV, Table 1) just by varying the abundance and local availability of these subunits relative to cytosolic β -subunits within a cell or nanodomain. This range is also reflected by an ~11 - 14 mV difference in $V_{0.5, \text{inact}}$ of R-type currents in our recordings from mouse midbrain DA neurons in culture and ex vivo slice recordings from SN DA neurons. However, the voltage-range of steady-state inactivation in both preparations is clearly more positive than predicted from heterologous expression with β 4- or β 3-subunits. This could be due to a different contribution of β 2a and/or β 2e to Cav2.3 channel complexes in these preparations. Our data predict that this contribution is higher in SN DA neurons than in cultured cells.

Our quantitative PCR analysis of β -subunit expression demonstrate that, although β 4 (60%) is the predominant one in the SN and VTA, β 2-subunit transcripts are also abundant and comprise about 27% of all β -subunits. These data are in excellent agreement with RNAseq data from mouse midbrain DA neurons with expression levels of about 33% for β 2 and 43% for β 4 (Brichta et al., 2015; Shin, 2015) and transcriptomic analysis of laser-captured SN DA

neurons from 18 human postmortem brains (30% $\beta 2$, 45% $\beta 4$; 15% $\beta 3$, 8% $\beta 1$; Aguila et al., 2021). While these transcriptomic data do not provide quantitative information about the expression of $\beta 2$ -splice variants, we clearly demonstrated the presence of both membrane-bound isoforms in identified SN DA neurons using PCR and RNAscope analysis.

Our transcript data (and confirmatory RNAseq data) show that $\beta 2a$ and $\beta 2e$ are present in SN DA neurons but still represent only a small fraction of all β -subunits present. However, our experimental data find a positive inactivation voltage-range suggesting that a majority of SNX-482-sensitive channels is associated with these β -subunits. At present biochemical data regarding preferential targeting of β -subunits to specific subcellular neuronal compartments and/or Cav-subtypes is absent but cannot be excluded. For example, $\beta 4$ -subunits may extensively target to channels at axonal presynaptic locations (as reported in cultured hippocampal neurons) or even to the nucleus (where they regulate gene transcription) and thus contribute less to Cav2.3 channel complexes at somatodendritic sites (Etemad et al., 2014). Moreover, differences in the affinity of β -subunits for their $\alpha 1$ -subunit interaction domain in the I-II-linker may also support preferential association with $\beta 2$ (De Waard et al., 1995).

Based on the finding that β -subunit association is required for expression of robust Cav2.3 channel currents (Figure 1A, Table 1), they must also play a key role in determining the gating properties of individual channel complexes. However, this does not exclude a modulatory role of other posttranslational modifications of Cav2.3 channels or protein interaction partners expressed at somatodendritic locations of SN DA neurons that could enhance Cav2.3 availability at more positive membrane potentials (such as Rab3-interacting proteins at axonal sites, Kiyonaka et al., 2007; Robinson et al., 2019).

A limitation of our work is that we cannot provide direct proof for a role of $\beta 2$ -subunit splice variants for R-type current modulation in DA neurons. Direct proof for the existence of such complexes would require biochemical studies requiring immunoprecipitation of Cav2.3 complexes from laser-dissected SN DA neurons. However, such studies, as well as other approaches, such as proximity ligation assays are hampered by the fact, that suitable $\beta 2$ -splice variant-specific antibodies are not available. We also found no suitable combination of antibodies raised in different species for such studies. Two mouse anti- $\beta 2$ (not even splice variant-specific) antibodies that could be combined with our previously used rabbit anti-Cav2.3 $\alpha 1$ subunit antibody turned out to bind to other nonspecific bands or cross-reacted with $\beta 3$ (not shown, data available upon request). Alternatively, direct proof for a role of $\beta 2$ -subunit splice variants could be obtained by a splice variant-specific gene knockout or siRNA-mediated knock-down of both $\beta 2a$ and $\beta 2e$ subunits in SN DA neurons, followed by isolation of Cav2.3 current components or Ca^{2+} transients of which only a fraction would be

mediated by $\beta 2a/\beta 2e$ -associated channels. This would be methodologically extremely challenging in these neurons.

We have previously shown that Cav2.3-knockout mice are protected from the selective loss of SN DA neurons in the chronic MPTP/probenecid PD model (Benkert et al., 2019). At least in this rodent model of PD, the observed protection provides strong evidence for a role of these channels in PD pathology. Pharmacological inhibition of Cav2.3 alone or together with other Caves may therefore confer beneficial disease-modifying effects and a novel approach for neuroprotection in PD. The recent failure of the LTCC blocker ISR in the STEADY-PD III trial (Investigators, 2020) to prevent disease progression in early PD patients indicates that inhibition of LTCCs alone may not be sufficient for neuroprotection. Our previous preclinical findings identified also Cav2.3 channels as novel drug targets for neuroprotective PD-therapy. Therefore, the inhibition of Cav2.3 in addition to Cav1.3 may be required for clinically meaningful neuroprotection. However, Cav2.3-mediated R-type currents are notoriously drug-resistant (Schneider et al., 2013), and so far no selective potent small-molecule Cav2.3/R-type blocker has been reported.

Our findings reported here provide the rationale for exploring novel neuroprotective strategies based on Cav2.3 channel inhibition. These could take advantage of the predicted strong dependence of continuous Cav2.3 channel activity on gating properties such as those stabilized by $\beta 2a$ and/or $\beta 2e$. Rather than inhibiting Ca^{2+} -entry through the pore-forming $\alpha 1$ -subunit, such a strategy could aim at reducing its contribution to the R-type current component persisting during continuous activity in SN DA neurons by interfering with the association of $\beta 2a$ and $\beta 2e$ subunits. Even if other β -subunits would replace them in the channel complex and ensure its stable expression, our data suggest that they would not be able to shift the steady-state inactivation voltage into the operating voltage range of SN DA neurons like $\beta 2a$ and $\beta 2e$. Such an approach appears realistic due to the availability of novel genetically encoded Ca^{2+} -channel inhibitors for a cell-type-specific gene therapeutic intervention. One such approach (CaVablator) has elegantly been used to specifically target Ca^{2+} -channel β -subunits for degradation by fusing β -specific nanobodies with the catalytic HECT domain of Nedd4L, an E3 ubiquitin ligase (Morgenstern et al., 2019). This strongly reduces Cav1- and Cav2-mediated Ca^{2+} -currents in different cell types. At present, it is unclear to which extent other high-voltage activated Cav2 channels (Cav2.1, Cav2.2) also contribute to the high vulnerability of SN DA neurons. However, our recent quantitative RNAScope analyses in mature SN DA neurons (Benkert et al., 2019) clearly demonstrate that Cav2.3 $\alpha 1$ -subunit (*Cacna1e*) transcripts are the most abundant $\alpha 1$ -subunit expressed in these cells, in excellent agreement with cell type-specific RNAseq data of identified midbrain DA neurons (Brichta et al., 2015; Shin, 2015).

We also show that in cultured mouse DA neurons, 100 nM SNX-482 slows pacemaking. While SNX-482 is highly suitable to isolate Cav2.3-mediated Ca^{2+} current components, effects on pacemaking also must take into account that this toxin is also a potent blocker of Kv4.3 channels (Kimm & Bean, 2014) underlying A-type K^{+} -currents (I_A). 60 nM nearly fully block reconstituted Kv4.3 currents in HEK cells ($\text{IC}_{50} \sim 3$ nM). Therefore, one can argue that in current-clamp recordings, 50-300 nM SNX-482 could alter pacemaking or the AP shape by effectively blocking Kv4.3 channels. However, the observed SNX-482-induced shortening of APs and the reduction of spontaneous firing are difficult to reconcile with a block of I_A channels, which typically induces a broadening of APs in several neuronal preparations (Kim et al., 2005) and an increased frequency in DA neurons (Liss et al., 2001).

Therefore, the observed SNX-482 effects in cultured neurons proved no final answer to the question about a potential role of Cav2.3 on pacemaking. In brain slices of Cav2.3 knockout mice, small changes in AP spike waveforms were observed, without major changes in pacemaking activity (Benkert et al., 2019). Similarly, inconsistent findings for the contribution of LTCC currents for pacemaking in slice recordings (Dragicevic et al., 2014; Guzman et al., 2009; Mercuri et al., 1994; Ortner et al., 2017) and cultured neurons (Puopolo et al., 2007) have been reported but the reasons for this remain unclear.

Despite providing no direct biochemical evidence, we here show the first example for a potential physiological and perhaps even pathophysiological role of $\beta 2$ -subunit alternative splicing emphasizing a need for further investigation in other types of neurons.

521 **Materials and Methods**

Key Resources Table				
Reagent type (species) or resource	Designation	Source or reference	Identifiers	Additional information
mouse strain:C57Bl/6N	C57Bl/6N	Charles River	C57Bl/6N	
mouse strain:C57Bl/6-TH-GFP mice	C57Bl/6-TH-GFP)	Matsushita et al., 2002; Sawamoto et al., 2001		GFP-expression under TH-promotor
transfected construct	human Cav1.3 _L α1-subunit (C-terminally long Cav1.3 splice variant)	Koschak et al., 2001	GenBank accession number EU363339	cloned into proprietary vector lacking GFP ("GFP ^{minus} "), described in Grabner et al., 1998
transfected construct	human Cav2.3 α1-subunit	Pereverzev et al., 2002)	Pereverzev et al., 2002)	cloned into pcDNA3 vector
transfected construct	rat β3-subunit	Koschak et al., 2001	GenBank: NM_012828,	cloned into pCMV6 vector
transfected construct	rat β2a-subunit	Koschak et al., 2001	GenBank: M80545	cloned into pCMV6 vector
transfected construct	mouse β2d-subunit	β2aN1, Link et al., 2009	GenBank: FM872408.1	cloned into pCAGGS vector
transfected construct	mouse β2e-subunit	β2aN5, Link et al., 2009	GenBank: FM872407	cloned into pCAGGS vector

transfected construct	C3S/C4S β 2a	(cysteine residues in position 3 and 4 of β 2a replaced by serines,	Gebhart et al., 2010	cloned into pCMV6 vector
transfected construct	rat β 4-subunit (splice variant β 4e)	Etemad et al., 2014		cloned into p β A vector
cell line (<i>Homo-sapiens</i>)	TsA-201 cells	European Collection of Authenticated Cell Cultures	ECACC, catalogue # 96121229, lot # 13D034	tested Mycoplasma negative
antibody	anti-tyrosine hydroxylase (TH; rabbit polyclonal)	Merck Millipore	Cat#: 657012,	1:1000
commercial assay or kit	RNeasy® Lipid Tissue Mini Kit	Qiagen GmbH, Germany	catalog # 1023539	
commercial assay or kit	phenol/guanidine-based Qiazol lysis reagent	Qiagen GmbH, Germany,	catalog # 79306	
commercial assay or kit	Maxima H Minus First Strand cDNA synthesis kit	Thermo Fisher Scientific, Waltham, MA, USA	catalog # K1682	
commercial assay or kit	Quant-IT PicoGreen dsDNA Assay Kit	Thermo Fisher Scientific, Waltham, MA, USA	catalog # P7589	
commercial assay or kit	Mycoplasma Detection Kit	ATCC	Universal Mycoplasma Detection Kit 30-1012K	
commercial assay or kit	TaqMan Universal PCR Master Mix	Thermo Fisher Scientific, Waltham, MA, USA		

commercial assay or kit	RNAScope® technology	Advanced Cell Diagnostics (ACD)	RNAScope Fluorescent Multiplex Detection Kit (ACD, Cat# 320851)	
chemical compound	neurobiotin-labeling reagent: Streptavidin Alexa Fluor conjugate 647	Thermo Fisher Scientific, Waltham, MA, USA	catalog # S21374	1:1000
chemical compound	SNX-482	Alomone Labs, Jerusalem, Israel	catalog # RTS-500	
Software, algorithm	Clampfit	Clampfit	Version 10.0 or 10.7, RRID:SCR_011323	
Software, algorithm	QuantStudio TM	Thermo Fisher Scientific, Waltham, MA, USA	Quantstudio 3 Software	
software, algorithm	Fiji	https://imagej.net/Fiji	Schindelin et al., 2012	
software, algorithm	GraphPad Prism	GraphPad	GraphPad Prism Ver 5, 7.04 and 8 (RRID:SCR_002798)	
software, algorithm	SigmaPlot	Systat Software, Germany	SigmaPlot Ver 14, RRID:SCR_003210	

522

523 **Animals**

524 For quantitative real-time PCR (RT-qPCR) experiments, male C57Bl/6N mice were bred in
525 the animal facility of the Centre for Chemistry and Biomedicine (CCB) of the University of
526 Innsbruck (approved by the Austrian Animal Experimentation Ethics Board). For
527 electrophysiological experiments of cultured midbrain DA neurons, C57Bl/6 TH-GFP mice
528 (Matsushita et al., 2002; Sawamoto et al., 2001) were kept heterozygous via breeding them

with C57Bl/6 mice (in accordance with the European Community's Council Directive 2010/63/UE and approved by the Italian Ministry of Health and the Local Organism responsible for animal welfare at the University of Torino; authorization DGSAF 0011710-P-26/07/2017). All animals were housed under a 12 hours light/dark cycle with food and water ad libitum. For whole cell voltage-clamp recordings of SN DA neurons in acute brain slices, as well as single-cell RT-qPCR, juvenile male C57Bl/6 mice (PN11-13) were bred at the animal facility of Ulm University. For RNAScope analysis, adult male C57Bl/6 mice and Cav2.3 WT mice were bred at the animal facility of Ulm University. Animal procedures at the Universities of Ulm (Regierungspräsidium Tübingen, Ref: 35/9185.81-3; Reg. Nr. o.147) and Cologne (LANUV NRW, Recklinghausen, Germany (84-02.05.20.12.254) were approved by the local authorities.

RNA isolation and cDNA synthesis for tissue RT-qPCR

Tissue was dissected after mice had been sacrificed by cervical dislocation under isoflurane (Vetflurane, Vibac UK, 1000 mg/g) anesthesia. The freshly extracted mouse brains from 12-14 weeks old male mice were snap-frozen in isopentane (Carl Roth, catalog #3926.2) that was pre-cooled with dry ice (~-40°C). To dissect VTA and SN tissue, 100 µm thick sections were cut on a cryostat (CM1950, Leica, Germany) and collected on glass coverslips. After cooling the coverslips on dry ice, regions of interest were punched under a dissection microscope using a pre-cooled sample corer (Fine Science Tools, Germany) (VTA: inner diameter 0.8 mm, 1 punch per hemisphere; SN: inner diameter 0.5 mm, 2 punches per hemisphere). For each brain region, tissue punches from both hemispheres of 7-8 successive 100 µm sections between Bregma -3.00 mm and -3.80 mm (according to Paxinos & Franklin, 2004) were collected in the sample corer. The tissue punches were transferred into an Eppendorf tube and again snap-frozen in liquid nitrogen. The punched brain sections were stained with cresyl violet (Nissl's staining) for histological verification. Briefly, the slides with the punched sections were incubated in 4% PFA overnight. On the next day, the sections were rinsed in H₂O and the following staining steps were performed: H₂O 1 min, 70% ethanol 5 min, 100% EtOH 5 min, 0.5% cresyl violet solution pH 3.9 (2.5 g cresyl violet acetate, 30 ml 1M Na-acetate*3 H₂O and 170 ml 1M acetic acid) 10 min, 70% ethanol 2 min, 100% ethanol 2 min, Xylol 1 min. The sections were coverslipped immediately with Eukitt (Sigma-Aldrich, catalog #03989), left to harden overnight and imaged on a bright field microscope at 2x.

RNeasy® Lipid Tissue Mini Kit (Qiagen GmbH, Germany, catalog #1023539) was used to isolate total RNA from brain tissues. Briefly, the tissue was disrupted and homogenized by vortexing samples for 5-10 minutes in 500 µl (SN, VTA) of phenol/guanidine-based Qiazol lysis reagent (Qiagen GmbH, Germany, catalog #79306) and passing the lysate ten times

through a 21-gauge needle. All further steps, including purification of RNA with QIAGEN silica gel membrane technology (Qiagen GmbH, Germany), were performed according to the manufacturer's protocol. For the final elution 15 µl of RNase-free water were used twice. An optional on-column DNase digestion (Qiagen GmbH, Germany, catalog #79254) was performed to reduce genomic DNA contamination. The RNA concentration was determined photometrically yielding approximately 20 ng/µl for VTA and SN or 1-2 µg/µl for whole brain.

RNA was reverse transcribed using Maxima H Minus First Strand cDNA synthesis kit with random hexamer primers following the manufacturer's instructions (Thermo Fisher Scientific, Waltham, MA, USA). 1 µg or 13 µl of total RNA were used as template for reverse transcription. 1 µl cDNA corresponds to 0.65 x the amount of RNA equivalent.

Standard curve method-based RT-qPCR for quantification of β -subunit expression in SN and VTA

In order to generate DNA templates of known concentrations for RT-qPCR standard curves, the concentration of the digested fragments was determined using the Quant-IT PicoGreen dsDNA Assay Kit (Invitrogen, Carlsbad, CA, USA). Subsequently, standard curves were generated using a serial dilution ranging from 10^7 to 10^1 DNA molecules in water containing 1 µg/ml of poly-dC DNA (Midland Certified Reagent Company Inc., Midland, TX, USA). RT-qPCRs of standard curves and samples were performed as described previously (Ortner et al., 2020; Schlick et al., 2010). Samples for RT-qPCR quantification (50 cycles) contained 5 ng of total RNA equivalent of cDNA, the respective TaqMan gene expression assay, and TaqMan Universal PCR Master Mix (Thermo Fisher Scientific). Specificity of all assays was confirmed using different DNA ratios of corresponding and mismatched DNA fragments for the $\beta 1$ -4 and for the $\beta 2a$ -2e assays, respectively. Importantly, all assays specifically recognized the corresponding fragment even in the presence of a 10-fold higher concentration of other splice variants (Figure 2-figure supplement 1). RT-qPCR was performed in duplicates from three independent RNA preparations from three biological replicates. Samples without template served as negative controls. No RT RNA controls could not be included since all obtained RNA was transcribed into cDNA due to low yields. The expression of seven different endogenous control genes was routinely measured and used for data normalization as previously described (Vandesompele et al., 2002) (Figure 2-figure supplement 1, Supplementary file 1): *Actb* (β -actin), *B2m* ($\beta 2$ -microglobulin), *Gapdh* (Glyceraldehyde 3-phosphate dehydrogenase), *Hprt1* (Hypoxanthine phosphoribosyltransferase 1), *Tbp* (TATA box-binding protein), *Tfrc* (Transferrin receptor) and *Sdha* (Succinate dehydrogenase subunit A) (Ortner et al., 2020; Schlick et al., 2010). Briefly, data were normalized to the most stably expressed endogenous control genes (*Gapdh* and *Tfrc*) determined by geNorm (Figure 2-figure supplement 1, Supplementary file

1). Normalized molecule numbers were calculated for each assay based on their respective standard curve. Standard curve parameters are given in (Supplementary file 3). qPCR analyses were performed using the 7500 Fast System (Applied Biosystems, Foster Systems, CA, USA).

Quantitative RT-qPCR of mouse brain tissue samples

Fragments of β -subunits and $\beta 2$ splice variants were amplified from mouse whole brain cDNA utilizing specific primers (Supplementary file 2) and subcloned into the Cav1.3 8a 42 pGFP^{minus} vector after restriction enzyme digestion using Sall and HindIII. Primer sequences for $\beta 1$ - $\beta 4$ have been described previously (Schlick et al., 2010), but additional Sall and HindIII restriction enzyme sites (underlined in Supplementary file 2) were inserted to allow subsequent ligation of fragments into the digested vector. TaqMan gene expression assays (Thermo Fisher Scientific, Waltham, MA, USA) and custom-made TaqMan gene expression assays were designed to span exon-exon boundaries (Supplementary file 2) as already described (Ortner et al., 2020).

The expression of $\beta 1$, $\beta 2$, $\beta 3$, $\beta 4$, $\beta 2a$, $\beta 2b$, $\beta 2c$ -d, and $\beta 2e$ was assessed using a standard curve method-based on PCR fragments of known concentration (Ortner et al., 2020; Schlick et al., 2010). $\beta 2c$ and $\beta 2d$ were detected by a common assay as selective primer design failed due to high sequence similarity. This assay binds at the exon-exon boundary of exons 2A and 3 of $\beta 2c$ and $\beta 2d$ and also recognizes a number of splice variants comprising the $\beta 2d$ N-terminus but with different alternative splicing in the HOOK region of the subunit (Buraei & Yang, 2010). Details about assay specificity are given in Figure 2-figure supplement 1 and Supplementary file 3.

cDNA constructs

For transient transfections hCav2.3e (cloned into pcDNA3, Pereverzev et al., 2002) or hCav1.3_L (human C-terminally long Cav1.3 splice variant; GenBank accession number EU363339) $\alpha 1$ subunits were transfected together with the previously described accessory subunit constructs: $\beta 3$ (rat, NM_012828, Koschak et al., 2001), $\beta 2a$ (rat, M80545, Koschak et al., 2001), $\beta 2d$ (mouse, $\beta 2aN1$, FM872408.1; Link et al., 2009), $\beta 2e$ (mouse, $\beta 2aN5$, FM872407; Link et al., 2009, where $\beta 2d$ and $\beta 2e$ were kindly provided by V. Flockerzi, Saarland University, Homburg), $C3S/C4S\beta 2a$ (cysteine residues in position 3 and 4 of $\beta 2a$ replaced by serines, Gebhart et al., 2010) or $\beta 4$ (rat, splice variant $\beta 4e$, kindly provided by Dr. Bernhard Flucher, Medical University Innsbruck; Etemad et al., 2014) and $\alpha 2\delta 1$ (rabbit, NM_001082276, Koschak et al., 2001).

Cell culture and transfection

TsA-201 cells were obtained from the European Collection of Authenticated Cell Cultures (ECACC, catalogue number 96121229, lot number 13D034) at passage 6. Cell stocks of passage 8 were frozen and cultures were re-expanded from stocks for not more than 20 passages. Cell cultures were tested negative (Universal Mycoplasma Detection Kit 30-1012K, American Type Culture Collection) for mycoplasma infection. TsA-201 cells were cultured as described (Ortner et al., 2020) in Dulbecco's modified Eagle's medium (DMEM; Sigma-Aldrich, catalog #D6546) that was supplemented with 10% fetal bovine serum (FBS, Gibco, catalog #10270-106), 2 mM L-glutamine (Gibco, catalog #25030-032), penicillin (10 units/ml, Sigma, P-3032) and streptomycin (10 µg/ml, Sigma, S-6501). Cells were maintained at 37°C and 5% CO₂ in a humidified incubator and were subjected to a splitting procedure after reaching ~80% confluency. For splitting, cells were dissociated using 0.05% trypsin after implementing a washing step using 1 x phosphate buffered saline (PBS). TsA-201 cells were replaced and freshly thawed when they exceeded passage no. 21. For electrophysiology, cells were plated on 10-cm culture dishes and subjected to transient transfections on the following day. Cells were transiently transfected using Ca²⁺-phosphate as previously described (Ortner et al., 2014) with 3 µg of α1 subunits, 2 µg of β subunits, 2.5 µg of α2δ1 subunits and 1.5 µg of eGFP to visualize transfected cells. On the next day, cells were plated onto 35-mm culture dishes that were coated with poly-L-lysine, kept at 30°C and 5% CO₂ and were then subjected to whole-cell patch-clamp experiments after 24-72 hours.

Primary cell culture of midbrain DA neurons

As described in Tomagra et al., 2019, the methods for the primary culture of mesencephalic dopamine neurons from substantia nigra (SN) were adapted from Pruszek et al., 2009. Briefly, the ventral mesencephalon area was dissected from embryonic (E15) C57Bl/6 TH-GFP mice (Matsushita et al., 2002; Sawamoto et al., 2001) that were kept heterozygous via breeding them with C57Bl/6J mice. HBSS (Hank's balanced salt solution, without CaCl₂ and MgCl₂), enriched with 0.18% glucose, 1% BSA, 60% papain (Worthington, Lakewood, NJ, United States), 20% DNase (Sigma-Aldrich) was stored at 4°C and used as digestion buffer. Neurons were plated at final densities of 600 cells per mm² on Petri dishes. Cultured neurons were used at 8 - 9 days in vitro (DIV) for current-clamp and voltage-clamp experiments. Petri dishes were coated with poly-L-Lysine (0.1 mg/ml) as substrate adhesion. Cells were incubated at 37°C in a 5% CO₂ atmosphere, with Neurobasal Medium containing 1% pen-strep, 1% ultra-glutamine, 2% B-27, and 2.5% FBS dialyzed (pH 7.4) (as previously described in Tomagra et al., 2019).

Whole-cell patch-clamp recordings in tsA-201 cells

For whole-cell patch-clamp recordings, patch pipettes with a resistance of 1.5-3.5 MΩ were pulled from glass capillaries (Borosilicate glass, catalog #64-0792, Harvard Apparatus, USA)

using a micropipette puller (Sutter Instruments) and fire-polished with a MF-830 microforge (Narishige, Japan). Recordings were obtained in the whole-cell configuration using an Axopatch 200B amplifier (Axon Instruments, Foster City, CA), digitized (Digidata 1322A digitizer, Axon Instruments) at 50 kHz, low-pass filtered at 5 kHz and subsequently analyzed using Clampfit 10.7 Software (Molecular Devices). Linear leak and capacitive currents were subtracted online using the P/4 protocol (20ms I-V protocol) or offline using a 50 ms hyperpolarizing voltage step from -89 to -99 mV or -119 to -129 mV. All voltages were corrected for a liquid junction potential (JP) of -9 mV (Lieb et al., 2014). Compensation was applied for 70-90% of the series resistance.

The pipette internal solution for recordings of Cav2.3 contained (in mM): 144.5 CsCl, 10 HEPES, 0.5 Cs-EGTA, 1 MgCl₂, 4 Na₂ATP adjusted to pH 7.4 with CsOH (299 mOsm/kg). The pipette internal solution for recordings of Cav1.3 contained (in mM): 135 CsCl, 10 HEPES, 10 Cs-EGTA, 1 MgCl₂, 4 Na₂ATP adjusted to pH 7.4 with CsOH (275 mOsm/kg). The bath solution for recordings of Cav2.3 contained (in mM): 2 CaCl₂, 10 HEPES, 170 Choline-Cl and 1 MgCl₂ adjusted to pH 7.4 with CsOH. The bath solution for recordings of Cav1.3 contained (in mM): 15 CaCl₂, 10 HEPES, 150 Choline-Cl and 1 MgCl₂ adjusted to pH 7.4 with CsOH.

Current-voltage (I-V) relationships were obtained by applying a 20 ms long square pulse protocol to various test potentials (5 mV voltage steps) starting from a holding potential (hp) of -119 mV or -89 mV (recovery of inactivation). The resulting I-V curves were fitted to the following equation:

$$I = G_{max}(V - V_{rev})/(1 + \exp\left[-\frac{V - V_{0.5}}{k}\right]),$$

where I is the peak current amplitude, G_{max} is the maximum conductance, V is the test potential, V_{rev} is the extrapolated reversal potential, V_{0.5} is the half-maximal activation voltage, and k is the slope factor. The voltage dependence of Ca²⁺-conductance was fitted using the following Boltzmann relationship:

$$G = G_{max}/(1 + \exp\left[-\frac{V - V_{0.5}}{k}\right])$$

The voltage dependence of inactivation was assessed by application of 20 ms test pulses to the voltage of maximal activation (V_{max}) before and after holding the cell at various conditioning test potentials for 5 s (30 s inter-sweep interval; 10 mV voltage steps; hp -119 mV). Inactivation was calculated as the ratio between the current amplitudes of the 20 ms test pulses. Steady-state inactivation parameters were obtained by fitting the data to a modified Boltzmann equation:

703
$$I = (1 - I_{ni}) / (1 + \exp \left[\frac{V - V_{0.5, \text{inact}}}{k_{\text{inact}}} \right] + I_{ni}),$$

704 where $V_{0.5, \text{inact}}$ is the half-maximal inactivation voltage, k_{inact} is the inactivation slope factor
 705 and I_{ni} is the fraction of non-inactivating current in steady-state.

706 The amount of inactivation during a 5 s depolarizing pulse from a hp of -119 mV to the V_{max}
 707 was quantified by calculating the remaining current fraction after 50, 100, 250, 500, 1000 and
 708 5000 ms. Recovery from inactivation was determined by 10 ms test pulses to V_{max} at different
 709 time-points (in s: 0.001, 0.003, 0.01, 0.03, 0.1, 0.3, 0.6, 1, 1.5, 2, 3, 4, 6, 8, 10, 15, 20) after a
 710 1-s conditioning pulse to V_{max} (hp -89 mV). Window current was determined by multiplying
 711 mean current densities by fractional currents from steady-state inactivation curves to obtain
 712 the fraction of available channels at a given potential as described previously (Hofer et al.,
 713 2020). The SN DA regular pacemaking command voltage protocol obtained from an
 714 identified TH⁺ SN DA neuron in a mouse brain slice (male, P12) and the SN DA burst firing
 715 protocol were generated as previously described (Ortner et al., 2017). Cells were perfused
 716 by an air pressure-driven perfusion system (BPS-8 Valve Control System, ALA Scientific
 717 Instruments) with bath solution and a flow rate of 0.6 ml/min. For Cd²⁺-block, cells were
 718 perfused with 100 μM Cd²⁺ to achieve full block, followed by wash-out with bath solution. A
 719 complete exchange of the solution around the cell was achieved within <50 ms. All
 720 experiments were performed at room temperature (~22°C).

721 **Voltage- and current-clamp recordings in cultured midbrain DA neurons**

722 Macroscopic whole-cell currents and APs were recorded using an EPC 10 USB HEKA
 723 amplifier and Patchmaster software (HEKA Elektronik GmbH) following the procedures
 724 described previously (Baldelli et al., 2005; Gavello et al., 2018). Traces were sampled at 10
 725 kHz and filtered using a low-pass Bessel filter set at 2 kHz. Borosilicate glass pipettes
 726 (Kimble Chase life science, Vineland, NJ, USA) with a resistance of 7-8 M Ω were used.
 727 Uncompensated capacitive currents were reduced by subtracting the averaged currents in
 728 response to P/4 hyperpolarizing pulses. Off-line data analysis was performed with pClamp
 729 10.0 software for current clamp recordings. Ca²⁺ currents were evoked by applying a single
 730 depolarization step (50 ms duration), from a holding of -70 mV to 0 mV. Fast capacitive
 731 transients due to the depolarizing pulse were minimized online by the patch-clamp analog
 732 compensation. Series resistance was compensated by 80% and monitored during the
 733 experiment.

734 For current-clamp experiments the pipette internal solution contained in mM: 135 gluconic
 735 acid (potassium salt: K-gluconate), 10 HEPES, 0.5 EGTA, 2 MgCl₂, 5 NaCl, 2 ATP-Tris and
 736 0.4 Tris-GTP (Tomagra et al., 2019). For voltage-clamp recordings the pipette internal
 737 solution contained in mM: 90 CsCl, 20 TEA-Cl, 10 EGTA, 10 glucose, 1 MgCl₂, 4 ATP, 0.5

GTP and 15 phosphocreatine adjusted to pH 7.4. The extracellular solution for current/voltage-clamp recordings (Tyrode's solution) contained in mM: 2 CaCl₂, 10 HEPES, 130 NaCl, 4 KCl, 2 MgCl₂, 10 glucose adjusted to pH 7.4. Patch-clamp experiments were performed using pClamp software (Molecular Devices, Silicon Valley, CA, United States). All experiments were performed at a temperature of 22–24°C. Data analysis was performed using Clampfit software. To study the contribution of Cav2.3 channels to the total Ca²⁺ current, cells were perfused with recording solution (containing in mM: 135 TEA, 2 CaCl₂, 2 MgCl₂, 10 HEPES, 10 glucose adjusted to pH 7.4) complemented with 300 nM TTX and 3 µM ISR to block voltage-dependent Na⁺ and L-type Ca²⁺ channels. SNX-482 (100 nM) was used in current- and voltage-clamp experiments. Furthermore, kynurenic acid (1 mM), 6,7-dinitroquinoxaline-2,3-dione (DNQX) (20 µM) and picrotoxin (100 µM) were present in the extracellular solution for current- and voltage-clamp experiments.

Whole cell voltage-clamp recordings of SN DA neurons in acute brain slices

Whole-cell patch-clamp recordings were performed essentially as previously described (Benkert et al., 2019). In brief, murine (PN11-13) coronal midbrain slices were prepared in ice-cold ACSF using a VibrosliceTM (Campden Instruments). Chemicals were obtained from Sigma Aldrich unless stated otherwise. ACSF contained in mM: 125 NaCl, 25 NaHCO₃, 2.5 KCl, 1.25 NaH₂PO₄, 2 CaCl₂, 2 MgCl₂ and 25 glucose, and was gassed with Carbogen (95% O₂, 5% CO₂, pH 7.4, osmolarity was 300 - 310 mOsm/kg). Slices were allowed to recover for 30 min at room temperature (22-25°C) before use for electrophysiology. Recordings were carried out in a modified ACSF solution containing in mM: 125 NaCl, 25 NaHCO₃, 2.5 KCl, 1.25 NaH₂PO₄, 2.058 MgCl₂, 1.8 CaCl₂, 2.5 glucose, 5 CsCl, 15 tetraethylammonium, 2.5 4-aminopyridine, 600 nM TTX (Tocris), 20 µM CNQX (Tocris), 4 µM SR 95531 (Tocris) and 10 µM DL-AP5 (Tocris), pH adjusted to 7.4, osmolarity was 300 - 315 mOsm/kg. Data were digitalised with 2 kHz, and filtered with Bessel Filter 1: 10 kHz; Bessel Filter 2: 5 kHz. All recordings were performed at a bath temperature of 33°C ± 1. Patch pipettes (2.5-3.5 MΩ) were filled with internal solution containing in mM: 180 N-Methyl-D-glucamine, 40 HEPES, 0.1 EGTA, 4 MgCl₂, 5 Na-ATP, 1 Lithium-GTP, 0.1% neurobiotin tracer (Vector Laboratories); pH was adjusted to 7.35 with H₂SO₄, osmolarity was 285 - 295 mOsm/kg. Neurons were filled with neurobiotin during the recording, fixed with a 4% PFA solution and stained for tyrosine hydroxylase (TH; rabbit anti-TH, 1:1000, Cat#: 657012, Merck Millipore) and neurobiotin (Streptavidin Alexa Fluor conjugate 647, 1:1000, Cat# S21374, Thermo Fisher Scientific). Only TH and neurobiotin positive cells were used for the statistical analysis.

Steady-state activation was measured by applying 150 ms depolarizing square pulses to various test potentials (10 mV increments) starting from -90 mV with a 10 sec interpulse

interval. Holding potential between the pulses was -100 mV. Voltage at maximal Ca^{2+} current amplitude (V_{max}) was determined during the steady-state activation recordings. Voltage-dependence of the steady-state inactivation was measured by applying a 20 ms control test pulse (from holding potential -100 mV to V_{max}) followed by 5-s conditioning steps to various potentials (10 mV increments) and a subsequent 20 ms test pulse to V_{max} with a 10 sec interpulse interval. Inactivation was calculated as the ratio between the current amplitudes of the test versus control pulse. Currents were leak subtracted on-line using the P/5 subtraction. The series resistance was compensated by 60-90%. Data were not corrected for liquid junction potential (-5 mV, measured according to Neher, 1992). Midbrain slices were preincubated (bath-perfusion) at least 30 min in selective T-type (10 μM Z941; Tringham et al., 2012), L-type (1 μM isradipine, ISR; www.guidetopharmacology.org), N- and P/Q-type (1 μM ω -conotoxin-MV1IC; www.guidetopharmacology.org) or R-type (100 nM SNX-482; www.guidetopharmacology.org, Newcomb et al., 1998) Ca^{2+} channel blockers; except Z941, which was kindly obtained from T. Snutch (University of British Columbia, Canada), all Cav blocker were from Tocris.

Steady-state activation and inactivation curves were fitted as described above.

Perforated patch recordings in SN DA neurons

Animals were anesthetized with isoflurane (B506; AbbVie Deutschland GmbH and Co KG, Ludwigshafen, Germany) and subsequently decapitated. The brain was rapidly removed and a block of tissue containing the mesencephalon was immediately dissected. Coronal slices (250 - 300 μm) containing the SN were cut with a vibration microtome (HM-650 V; Thermo Scientific, Walldorf, Germany) under cold (4°C), carbogenated (95% O_2 and 5% CO_2), glycerol-based modified artificial cerebrospinal fluid (GACSF; Ye et al., 2006) containing (in mM): 250 glycerol, 2.5 KCl, 2 MgCl_2 , 2 CaCl_2 , 1.2 NaH_2PO_4 , 10 HEPES, 21 NaHCO_3 , 5 glucose adjusted to pH 7.2 (with NaOH) resulting in an osmolarity of ~ 310 mOsm. Brain slices were transferred into carbogenated artificial cerebrospinal fluid (ACSF). First, they were kept for 20 min in a 35°C 'recovery bath' and then stored at room temperature (24°C) for at least 30 min prior to recording. ACSF contained (in mM): 125 NaCl, 2.5 KCl, 2 MgCl_2 , 2 CaCl_2 , 1.2 NaH_2PO_4 , 21 NaHCO_3 , 10 HEPES, and 5 Glucose adjusted to pH 7.2 (with NaOH) resulting in an osmolarity of ~ 310 mOsm.

SN dopaminergic neurons were identified according to their sag component / slow I_h -current (hyperpolarization-activated cyclic nucleotide-gated cation current), broad action potentials or post hoc by TH/DAT-immunohistochemistry (Lacey et al., 1989; Neuhoff et al., 2002; Richards et al., 1997) (Figure 6-figure supplement 1I,J). Biocytin-streptavidin labeling was combined with TH-immuno-histochemistry (Hess et al., 2013).

After preparation, brain slices were transferred to a recording chamber (~1.5 ml volume) and initially superfused with carbogenated ACSF at a flow rate of ~2 ml/min. During the perforation process, the electrophysiological identification of the neuron was performed in current clamp mode. Afterwards, the ACSF was exchanged for the Ca^{2+} current recording solution which contained in mM: 66.5 NaCl, 2 MgCl_2 , 3 CaCl_2 , 21 NaHCO_3 , 10 HEPES, 5 Glucose adjusted to pH 7.2 (with HCl). Sodium currents were blocked by 1 μM tetrodotoxin (TTX). Potassium currents and the I_h current were blocked by: 40 mM TEA-Cl, 0.4 mM 4-AP, 1 μM M phrixotoxin-2 (Alomone, Cat # STP-710; Subramaniam et al., 2014) and 20 mM CsCl. Experiments were carried out at ~28°C. Recordings were performed with an EPC10 amplifier (HEKA, Lambrecht, Germany) controlled by the software PatchMaster (version 2.32; HEKA). In parallel, data were sampled at 10 kHz with a CED 1401 using Spike2 (version 7) (both Cambridge Electronic Design, UK) and low-pass filtered at 2 kHz with a four-pole Bessel filter. The liquid junction potential between intracellular and extracellular solution was compensated (12 mV; calculated with Patcher's Power Tools plug-in for Igor Pro 6 (Wavemetrics, Portland, OR, USA)).

Perforated patch recordings were performed using protocols modified from (Horn & Marty, 1988) and (Akaike & Harata, 1994). Electrodes with tip resistances between 2 and 4 M Ω were fashioned from borosilicate glass (0.86 mm inner diameter; 1.5 mm outer diameter; GB150- 8P; Science Products) with a vertical pipette puller (PP-830; Narishige, London, UK). Patch recordings were performed with ATP and GTP free pipette solution containing (in mM): 138 Cs-methanesulfonate, 10 CsCl_2 , 2 MgCl_2 , 10 HEPES and adjusted to pH 7.2 (with CsOH). ATP and GTP were omitted from the intracellular solution to prevent uncontrolled permeabilization of the cell membrane (Lindau & Fernandez, 1986). The patch pipette was tip filled with internal solution and back filled with 0.02% tetraethylrhodamine-dextran (D3308, Invitrogen, Eugene, OR, USA) and amphotericin-containing internal solution (~400 $\mu\text{g/ml}$; G4888; Sigma-Aldrich, Taufkirchen, Germany) to achieve perforated patch recordings. Amphotericin was dissolved in dimethyl sulfoxide (final concentration: 0.2 - 0.4%; DMSO; D8418, Sigma-Aldrich) (Rae et al., 1991), and was added to the modified pipette solution shortly before use. The used DMSO concentration had no obvious effect on the investigated neurons. During the recordings access resistance (R_a) was constantly monitored and experiments were started after R_a was < 20 M Ω . In the analyzed recordings R_a was comparable, did not change significantly over recording time, and was not significantly different between the distinct experimental groups. A change to the whole-cell configuration was indicated by a sudden change in R_a and diffusion of tetraethylrhodamine-dextran into the neuron. Such experiments were rejected. GABAergic and glutamatergic synaptic input was reduced by addition of 0.4 mM picrotoxin (P1675; Sigma-Aldrich), 50 μM D-AP5 (A5282; Sigma-Aldrich), and 10 μM CNQX (C127; Sigma-Aldrich) to the ACSF. For inhibition

experiments, 100 nM SNX-482 (Alomone, Cat # RTS-500 dissolved in ACSF) or 10 μ M nifedipine (Alomone, Cat # N-120 diluted into ACSF from a freshly prepared 10 mM stock solution in DMSO) was bath applied (in ACSF).

Identification of β -subunit transcripts in identified SN DA and VTA DA neurons

RNAScope *in situ* hybridization

In situ hybridization experiments were performed on fresh frozen mouse brain tissue using the RNAScope® technology (Advanced Cell Diagnostics, ACD), according to the manufacturer's protocol under RNase-free conditions and essentially as described (Benkert et al., 2019). Briefly, 12 μ m coronal cryosections were prepared (Duda et al., 2018), mounted on SuperFrost® Plus glass slides, and dried for one hour at -20°C. Directly before starting the RNAScope procedure, sections were fixed with 4% PFA for 15 min at 4°C and dehydrated using an increasing ethanol series (50%, 75%, 100%), for 5 min each. After treatment with protease IV (ACD, Cat# 322336) for 30 min at room temperature, sections were hybridized with the respective target probes for 2 h at 40°C in a HybEZ II hybridization oven (ACD). Target probe signals were amplified using the RNAScope Fluorescent Multiplex Detection Kit (ACD, Cat# 320851). All amplifier solutions were dropped on respective sections, incubated at 40°C in the HybEZ hybridization oven, and washed twice with wash buffer (ACD) between each amplification step for 2 min each. Nuclei were counterstained with DAPI ready-to-use solution (ACD, included in Kit) and slides were coverslipped with HardSet mounting medium (VectaShield, Cat# H-1400) and dried overnight. Target probes were either obtained from the library of validated probes provided by Advanced Cell Diagnostics (ACD) or self-designed in cooperation with ACD to specifically discriminate between two splice variants of β 2, namely β 2a and β 2e. Target probes (RNAScope assays) used for analysis were as follows: Tyrosine hydroxylase (TH) (*Th*), Cat No. (ACD) 317621, Assay target region: 483 – 1603 of NM_009377.1; β 2a (*Cacnb2*), Cat No. (ACD) 590951-C2, Assay target region: 2-296 of XM_011238946.2; β 2e (*Cacnb2*), Cat No. (ACD) 823221-C2, Assay target region: 2-285 of NM_001309519.1.

Target genes, visualized with Atto550 fluorophore, were co-stained with Tyrosine hydroxylase (TH), visualized with AlexaFluor488, as a marker for dopaminergic neurons. The gene peptidyl-prolyl isomerase B (PPIB) was used as positive control.

Fluorescent images of midbrain sections were acquired by a Leica CTR6 LED microscope using a Leica DFC365FX camera as z-stacks, covering the full depth of cells at 63x magnification. Z-stacks were reduced to maximum intensity Z-projections using Fiji (<http://imagej.net/Fiji>) and images were analyzed by utilizing a custom-designed algorithm (Wolution, Munich, Germany). The algorithm delineates cell shapes according to the TH

marker gene signal and quantifies the area of fluorescent staining. According to Advanced Cell Diagnostics (ACD), target probe hybridization results in a small fluorescent dot for each mRNA molecule, allowing quantification of absolute number of mRNA molecules independent from fluorescent signal intensity.

Multiplex-nested PCR, qualitative and quantitative PCR analysis in individual laser-microdissected DA neurons

Cryosectioning, laser-microdissection, reverse transcription: Cryosectioning, UV-laser microdissection (UV-LMD) and reverse transcription were carried out similarly as previously described in detail (Benkert et al., 2019; Duda et al., 2018; Grundemann et al., 2011; Liss, 2002). Briefly, coronal 12 μ m mouse midbrain cryosections were cut with a cryomicrotome CM3050 S (Leica), mounted on PEN-membrane slides (Mirodissect), stained with a cresyl-violet (CV) ethanol solution and fixed with an ascending ethanol series. UV-LMD of SN dopaminergic neurons from cresyl-violet-stained midbrain sections from juvenile mice was carried out using an LMD7000 system (Leica Microsystems). Reverse transcription was carried out directly without a separate RNA isolation step in a one-tube procedure.

All cDNA samples were precipitated as described (Liss, 2002). Qualitative multiplex-nested PCR and quantitative qPCRs were carried out essentially as described (Benkert et al., 2019; Duda et al., 2018; Grundemann et al., 2011). Briefly, qualitative multiplex-nested PCR was performed with the GeneAmp PCR System 9700 (Thermo Fisher Scientific) using 1/3 of each individual cDNA sample, corresponding to ~3 SN DA neurons, for marker gene expression analysis: tyrosine hydroxylase (*Th*) as a marker for dopaminergic midbrain neurons, the glutamic acid decarboxylase isoforms *Gad₆₅* and *Ga₆₇* as markers for GABAergic neurons, the glial fibrillary acidic protein (*Gfap*) as a marker for astroglia cells and calbindin (*Calb1*) d28k (CBd28k), that is strongly expressed only in less vulnerable dopaminergic midbrain neurons. Only cDNA pools expressing the correct marker gene profile (i.e., *Th*-positive, *Gad*-, *Gfap*-, *CBd28k*-negative) were further analyzed via qualitative and quantitative PCR. Qualitative PCR for β 2 (*Cacnb2*) splice variant expression analysis was performed with the QuantStudio 3 System (Thermo Fisher Scientific) using ~3 SN DA neurons. Qualitative PCR products were analyzed in a QIAxcel Advanced System (Qiagen).

Details of multiplex PCR (outer) and nested PCR (inner) primers for qualitative PCR are shown in Supplementary file 5.

For Cav2.3 (*Cacna1e*) splice variant analysis via qualitative RT-PCR, two cDNA fragments (mCav2.3 II-III loop and mCav2.3 C-terminus) covering the three respective splice sites were amplified in a duplex PCR, followed by two individual nested PCR reactions. PCR conditions: 15 min 95°C; 35 cycles: 30 s 94°C; 1 min 61°C; 3 min 72°C; 7 min 72°C for duplex PCR; and

3 min 94°C; 35 cycles: 30 s 94°C; 1 min 61°C; 1 min 72°C; 7 min 72°C for nested PCRs. Primer sequences are given in Supplementary file 2. Outer duplex primer pairs were chosen using Oligo7.60 software (possible PCR amplicon sizes for mCav2.3 II-III loop: 816 bp, 795 bp and 759 bp; for mCav2.3 C-terminus: 770 bp and 641 bp). For the nested PCRs, primer sequences from Weiergraber et al., 2005 were used (possible PCR amplicon sizes for mCav2.3 II-III 980 loop: 420 bp, 399 bp and 363 bp; for mCav2.3 C-terminus: 498 bp and 369 bp). Nested PCR products were separated in a 4% agarose gel (MetaPhor agarose, Biozym), and expressed splice variants in individual SN DA neurons were identified according to the amplicon sizes of the nested PCR products (cDNA from mouse whole-brain tissue was used as positive control) as follows (II-III-loop + C-terminus): Cav2.3a: 363 + 369 bp; Cav2.3b: 399+369 bp; Cav2.3c: 420+369 bp; Cav2.3d: 420+498; Cav2.3e: 363 + 498 bp; Cav2.3f: 399 + 498 bp.

Quantitative real time PCR (qPCR) was performed with the QuantStudio 3 System (Thermo Fisher Scientific). qPCR assays (TaqMan®), were marked with a 3' BHQ (black hole quencher) and 5' FAM (Carboxyfluorescein). TaqMan assays were carefully established and performance was evaluated by generating standard curves, using defined amounts of cDNA (derived from midbrain tissue mRNA), over four magnitudes of 10-fold dilutions as templates, in at least three independent experiments, as described (Duda et al., 2018; Liss, 2002).

Details of all qPCR assays (TaqMan®), and standard curve parameters used for analysis are provided in Supplementary file 4.

Relative qPCR quantification data are given as cDNA amount [pg/cell] with respect to midbrain-tissue cDNA standard curves, calculated according to the following formula, and were normalized to the respective cell size by dividing respective expression values to the corresponding area of the individual microdissected neurons.

$$DNA \text{ amount per cell } \left[\frac{pg}{cell} \right] = \frac{S^{[(Ct - Y_{intercept})/slope]}}{No_{cells} \cdot cDNA \text{ fraction}}$$

With S = serial dilution factor of the standard curve (i.e. 10), No_{cells} = number of SN DA neurons per sample (i.e. 10 here), cDNA fraction = fraction of the cDNA reaction used as template in the qPCR reaction (i.e. 5/17) and the Y-intercept and slope of the relative standards (see Supplementary file 4).

β2 (*Cacnb2*) TaqMan qPCR assay and standard curve information, used for relative qPCR-based transcript quantification: Note that the amplicon is very small (70 bp). The probe is 5'-FAM (6-carboxyfluorescein) and 3'-NFQ (non-fluorescent quencher) labelled. The assay Mm01333550_m1 (assay-ID) was used (assay location 583) spanning exon-boundary 4-5 of the mouse β2 gene (*Cacnb2*). Assay parameters were as follows: threshold for analysis:

949 0.05, Y-intercept of standard curve: 43.5 ± 0.2 , slope: -3.43 ± 0.04 , R^2 : 1.0 ± 0.0 : means \pm
950 SEM, n=5.

951 **Statistics**

952 Data were analyzed using Clampfit 10.7 (Axon Instruments), Microsoft Excel, SigmaPlot 14.0
953 (Systat Software, Inc), and GraphPad Prism 5, 7.04 or 8 software (GraphPad software, Inc).
954 Data were analyzed by appropriate statistical testing as indicated in detail for all experiments
955 in the text, figure and table legends. Statistical significance was set at $p < 0.05$. Brain slice
956 patch-clamp data were also analyzed with FitMaster (v2x90.5, HEKA Elektronik). RNAScope
957 and single-cell RT-qPCR data data were analyzed by Fiji (<https://imagej.net/Fiji>),
958 QuantStudio™ Design and Analysis Software (Applied Biosystems) and GraphPad Prism
959 7.04. All values are presented as mean \pm SEM (95% confidence interval) for the indicated
960 number of experiments (n) from N independent experiments (biological replications) in the
961 text and Figures unless stated otherwise.

962

963 **Acknowledgements**

964 We thank Dr. Veit Flockerzi for cDNA of $\beta 2$ splice variants, and Jennifer Müller and Gospava
965 Stojanovic for expert technical assistance.

966

967 **Competing interests**

968 The authors declare that they have no financial and non-financial competing interests.

References

- Aguila, J., Cheng, S., Kee, N., Cao, M., Wang, M., Deng, Q., & Hedlund, E. (2021). Spatial RNA Sequencing Identifies Robust Markers of Vulnerable and Resistant Human Midbrain Dopamine Neurons and Their Expression in Parkinson's Disease. *Front Mol Neurosci*, 14. <https://doi.org/10.3389/fnmol.2021.699562>
- Akaike, N., & Harata, N. (1994). Nystatin perforated patch recording and its applications to analyses of intracellular mechanisms. *Jpn J Physiol*, 44 (5), 433-473. <https://doi.org/10.2170/jjphysiol.44.433>
- Baldelli, P., Hernandez-Guijo, J. M., Carabelli, V., & Carbone, E. (2005). Brain-derived neurotrophic factor enhances GABA release probability and nonuniform distribution of N- and P/Q-type channels on release sites of hippocampal inhibitory synapses. *J Neurosci*, 25 (13), 3358-3368. <https://doi.org/10.1523/JNEUROSCI.4227-04.2005>
- Benkert, J., Hess, S., Roy, S., Beccano-Kelly, D., Wiederspohn, N., Duda, J., Simons, C., Patil, K., Gaifullina, A., Mannal, N., Dragicevic, E., Spaich, D., Muller, S., Nemeth, J., Hollmann, H., Deuter, N., Mousba, Y., Kubisch, C., Poetschke, C., Striessnig, J., Pongs, O., Schneider, T., Wade-Martins, R., Patel, S., Parlato, R., Frank, T., Kloppenburg, P., & Liss, B. (2019). Cav2.3 channels contribute to dopaminergic neuron loss in a model of Parkinson's disease. *Nat Commun*, 10 (1), 5094. <https://doi.org/10.1038/s41467-019-12834-x>
- Bian, X., Zhou, X., & Galligan, J. J. (2004). R-type calcium channels in myenteric neurons of guinea pig small intestine. *Am J Physiol Gastrointest Liver Physiol*, 287 (1), G134-G142. <https://doi.org/10.1152/ajpgi.00532.2003>
- Biglan, K. M., Oakes, D., Lang, A. E., Hauser, R. A., Hodgeman, K., Greco, B., Lowell, J., Rockhill, R., Shoulson, I., Venuto, C., Young, D., Simuni, T., & Investigators, P. S. G. S. P. I. (2017). A novel design of a Phase III trial of isradipine in early Parkinson disease (STEADY-PD III). *Ann Clin Transl Neurol*, 4, 360-368. <https://doi.org/10.1002/acn3.412>
- Bijlmakers, M. J., & Marsh, M. (2003). The on-off story of protein palmitoylation. *Trends Cell Biol*, 13 (1), 32-42. [https://doi.org/10.1016/s0962-8924\(02\)00008-9](https://doi.org/10.1016/s0962-8924(02)00008-9)
- Bock, G., Gebhart, M., Scharinger, A., Jangsangthong, W., Busquet, P., Poggiani, C., Sartori, S., Mangoni, M. E., Sinnegger-Brauns, M. J., Herzig, S., Striessnig, J., & Koschak, A. (2011). Functional properties of a newly identified C-terminal splice variant of Cav1.3 L-type Ca²⁺ channels. *J Biol Chem*, 286 (49), 42736-42748. <https://doi.org/10.1074/jbc.M111.269951>

- 1004 Bolam, J. P., & Pissadaki, E. K. (2012). Living on the edge with too many mouths to feed:
1005 why dopamine neurons die. *Mov Disord*, 27, 1478-1483.
1006 <https://doi.org/10.1002/mds.25135>
- 1007 Bourinet, E., Stotz, S. C., Spaetgens, R. L., Dayanithi, G., Lemos, J., Nargeot, J., & Zamponi,
1008 G. W. (2001). Interaction of SNX482 with domains III and IV inhibits activation gating
1009 of $\alpha(1E)$ (CaV)2.3 calcium channels. *Biophys J*, 81 (1), 79-88.
1010 [https://doi.org/10.1016/s0006-3495\(01\)75681-0](https://doi.org/10.1016/s0006-3495(01)75681-0)
- 1011 Branch, S. Y., Sharma, R., & Beckstead, M. J. (2014). Aging decreases L-type calcium
1012 channel currents and pacemaker firing fidelity in substantia nigra dopamine neurons.
1013 *J Neurosci*, 34, 9310-9318. <https://doi.org/10.1523/JNEUROSCI.4228-13.2014>
- 1014 Brichta, L., Shin, W., Jackson-Lewis, V., Blesa, J., Yap, E. L., Walker, Z., Zhang, J.,
1015 Roussarie, J. P., Alvarez, M. J., Califano, A., Przedborski, S., & Greengard, P. (2015).
1016 Identification of neurodegenerative factors using translational-regulatory network
1017 analysis. *Nat Neurosci*, 18 (9), 1325-1333. <https://doi.org/10.1038/nn.4070>
- 1018 Buraei, Z., & Yang, J. (2010). The β subunit of voltage-gated Ca^{2+} channels. *Physiol Rev*, 90
1019 (4), 1461-1506. <https://doi.org/10.1152/physrev.00057.2009>
- 1020 Burbulla, L. F., Song, P., Mazzulli, J. R., Zampese, E., Wong, Y. C., Jeon, S., Santos, D. P.,
1021 Blanz, J., Obermaier, C. D., Strojny, C., Savas, J. N., Kiskinis, E., Zhuang, X., Krüger,
1022 R., Surmeier, D. J., & Krainc, D. (2017). Dopamine oxidation mediates mitochondrial
1023 and lysosomal dysfunction in Parkinson's disease. *Science (New York, N.Y.)*.
1024 <https://doi.org/10.1126/science.aam9080>
- 1025 Calorio, C., Gavello, D., Guarina, L., Salio, C., Sassoè-Pognetto, M., Riganti, C., Bianchi, F.
1026 T., Hofer, N. T., Tuluc, P., Obermaier, G. J., Defilippi, P., Balzac, F., Turco, E., Bett, G.
1027 C., Rasmusson, R. L., & Carbone, E. (2019). Impaired chromaffin cell excitability and
1028 exocytosis in autistic Timothy syndrome TS2-neo mouse rescued by L-type calcium
1029 channel blockers. *J Physiol*, 597 (6), 1705-1733. <https://doi.org/10.1113/JP277487>
- 1030 Damier, P., Hirsch, E. C., Agid, Y., & Graybiel, A. M. (1999). The substantia nigra of the
1031 human brain. II. Patterns of loss of dopamine-containing neurons in Parkinson's
1032 disease. *Brain*, 122 (Pt 8), 1437-1448.
1033 <http://www.ncbi.nlm.nih.gov/pubmed/10430830>
- 1034 De Waard, M., Witcher, D. R., Pragnell, M., Liu, H., & Campbell, K. P. (1995). Properties of
1035 the $\alpha 1$ - β anchoring site in voltage-dependent calcium channels. *J Biol Chem*, 270,
1036 12056-12064. <https://doi.org/10.1074/jbc.270.20.12056>
- 1037 Dragicevic, E., Poetschke, C., Duda, J., Schlaudraff, F., Lammel, S., Schiemann, J., Fauler,
1038 M., Hetzel, A., Watanabe, M., Lujan, R., Malenka, R. C., Striessnig, J., & Liss, B.
1039 (2014). Cav1.3 channels control D2-autoreceptor responses via NCS-1 in substantia

- nigra dopamine neurons. *Brain*, 137, 2287-2302.
<https://doi.org/10.1093/brain/awu131>
- Dragicevic, E., Schiemann, J., & Liss, B. (2015). Dopamine midbrain neurons in health and Parkinson's disease: Emerging roles of voltage-gated calcium channels and ATP-sensitive potassium channels. *Neuroscience*, 284, 798-814.
<https://doi.org/10.1016/j.neuroscience.2014.10.037>
- Duda, J., Fauler, M., Grundemann, J., & Liss, B. (2018). Cell-Specific RNA Quantification in Human SN DA Neurons from Heterogeneous Post-mortem Midbrain Samples by UV-Laser Microdissection and RT-qPCR. *Methods Mol Biol*, 1723, 335-360.
https://doi.org/10.1007/978-1-4939-7558-7_19
- Etemad, S., Obermair, G. J., Bindreither, D., Benedetti, A., Stanika, R., Di Biase, V., Bartscher, V., Koschak, A., Kofler, R., Geley, S., Wille, A., Lusser, A., Flockerzi, V., & Flucher, B. E. (2014). Differential neuronal targeting of a new and two known calcium channel beta4 subunit splice variants correlates with their regulation of gene expression. *J Neurosci*, 34 (4), 1446-1461. <https://doi.org/10.1523/jneurosci.3935-13.2014>
- Evans, R. C., Zhu, M., & Khaliq, Z. M. (2017). Dopamine Inhibition Differentially Controls Excitability of Substantia Nigra Dopamine Neuron Subpopulations through T-Type Calcium Channels. *J Neurosci*, 37 (13), 3704-3720.
<https://doi.org/10.1523/JNEUROSCI.0117-17.2017>
- Gantz, S. C., Ford, C. P., Morikawa, H., & Williams, J. T. (2018). The Evolving Understanding of Dopamine Neurons in the Substantia Nigra and Ventral Tegmental Area. *Annu Rev Physiol*, 80, 219-241. <https://doi.org/10.1146/annurev-physiol-021317-121615>
- Gavello, D., Calorio, C., Franchino, C., Cesano, F., Carabelli, V., Carbone, E., & Marcantoni, A. (2018). Early Alterations of Hippocampal Neuronal Firing Induced by Abeta42. *Cereb Cortex*, 28 (2), 433-446. <https://doi.org/10.1093/cercor/bhw377>
- Gebhart, M., Juhasz-Vedres, G., Zuccotti, A., Brandt, N., Engel, J., Trockenbacher, A., Kaur, G., Obermair, G. J., Knipper, M., Koschak, A., & Striessnig, J. (2010). Modulation of Cav1.3 Ca2+ channel gating by Rab3 interacting molecule. *Mol Cell Neurosci*, 44 (3), 246-259. <https://doi.org/10.1016/j.mcn.2010.03.011>
- Giguere, N., Burke Nanni, S., & Trudeau, L. E. (2018). On Cell Loss and Selective Vulnerability of Neuronal Populations in Parkinson's Disease. *Front Neurol*, 9, 455.
<https://doi.org/10.3389/fneur.2018.00455>
- Grabner, M., Dirksen, R. T., & Beam, K. G. (1998). Tagging with green fluorescent protein reveals a distinct subcellular distribution of L-type and non-L-type Calcium channels expressed in dysgenic myotubes. *Proc Natl Acad Sci U S A*, 95 (4), 1903-1908.
<https://doi.org/10.1073/pnas.95.4.1903>

- 1077 Grace, A. A., & Bunney, B. S. (1984). The control of firing pattern in nigral dopamine
1078 neurons: single spike firing. *J Neurosci*, 4, 2866-2876.
1079 <https://doi.org/10.1523/JNEUROSCI.04-11-02877.1984>
- 1080 Grundemann, J., Schlaudraff, F., & Liss, B. (2011). UV-laser microdissection and mRNA
1081 expression analysis of individual neurons from postmortem Parkinson's disease
1082 brains. *Methods Mol Biol*, 755, 363-374. [https://doi.org/10.1007/978-1-61779-163-](https://doi.org/10.1007/978-1-61779-163-5_30)
1083 [5_30](https://doi.org/10.1007/978-1-61779-163-5_30)
- 1084 Guarina, L., Calorio, C., Gavello, D., Moreva, E., Traina, P., Battiato, A., Ditalia Tchernij, S.,
1085 Forneris, J., Gai, M., Picollo, F., Olivero, P., Genovese, M., Carbone, E., Marcantoni,
1086 A., & Carabelli, V. (2018). Nanodiamonds-induced effects on neuronal firing of mouse
1087 hippocampal microcircuits. *Sci Rep*, 8 (1), 2221. [https://doi.org/10.1038/s41598-018-](https://doi.org/10.1038/s41598-018-20528-5)
1088 [20528-5](https://doi.org/10.1038/s41598-018-20528-5)
- 1089 Guzman, J. N., Ilijic, E., Yang, B., Sanchez-Padilla, J., Wokosin, D., Galtieri, D., Kondapalli,
1090 J., Schumacker, P. T., & Surmeier, D. J. (2018). Systemic isradipine treatment
1091 diminishes calcium-dependent mitochondrial oxidant stress. *J Clin Invest*, 128 (6),
1092 2266-2280. <https://doi.org/10.1172/JCI95898>
- 1093 Guzman, J. N., Sanchez-Padilla, J., Chan, C. S., & Surmeier, D. J. (2009). Robust
1094 pacemaking in substantia nigra dopaminergic neurons. *J Neurosci*, 29 (35), 11011-
1095 11019. <https://doi.org/10.1523/JNEUROSCI.2519-09.2009> [doi]
- 1096 Hess, M. E., Hess, S., Meyer, K. D., Verhagen, L. A., Koch, L., Bronneke, H. S., Dietrich, M.
1097 O., Jordan, S. D., Saletore, Y., Elemento, O., Belgardt, B. F., Franz, T., Horvath, T.
1098 L., Ruther, U., Jaffrey, S. R., Kloppenburg, P., & Bruning, J. C. (2013). The fat mass
1099 and obesity associated gene (Fto) regulates activity of the dopaminergic midbrain
1100 circuitry. *Nat Neurosci*, 16 (8), 1042-1048. <https://doi.org/10.1038/nn.3449>
- 1101 Hofer, N. T., Tuluc, P., Ortner, N. J., Nikonishyna, Y. V., Fernandes-Quintero, M. L., Liedl, K.
1102 R., Flucher, B. E., Cox, H., & Striessnig, J. (2020). Biophysical classification of a
1103 CACNA1D de novo mutation as a high-risk mutation for a severe
1104 neurodevelopmental disorder. *Mol Autism*, 11 (1), 4. [https://doi.org/10.1186/s13229-](https://doi.org/10.1186/s13229-019-0310-4)
1105 [019-0310-4](https://doi.org/10.1186/s13229-019-0310-4)
- 1106 Horn, R., & Marty, A. (1988). Muscarinic activation of ionic currents measured by a new
1107 whole-cell recording method. *J Gen Physiol*, 92 (2), 145-159.
1108 <https://doi.org/10.1085/jgp.92.2.145>
- 1109 Investigators, P. S. G.-S.-P. (2020). Isradipine Versus Placebo in Early Parkinson Disease: A
1110 Randomized Trial. *Ann Intern Med*, 172 (9), 591-598. [https://doi.org/10.7326/M19-](https://doi.org/10.7326/M19-2534)
1111 [2534](https://doi.org/10.7326/M19-2534)

- 1112 Jones, L. P., Wei, S. K., & Yue, D. T. (1998). Mechanism of auxiliary subunit modulation of
1113 neuronal α_1E calcium channels. *J Gen Physiol*, 112 (2), 125-143.
1114 <http://www.ncbi.nlm.nih.gov/pubmed/9689023>
- 1115 Kato, M., Ui-Tei, K., Watanabe, M., & Sakuma, Y. (2003). Characterization of Voltage-Gated
1116 Calcium Currents in Gonadotropin-Releasing Hormone Neurons Tagged with Green
1117 Fluorescent Protein in Rats. *Endocrinology*, 144 (11), 5118-5125.
1118 <https://doi.org/10.1210/en.2003-0213>
- 1119 Kepplinger, K. J., Forstner, G., Kahr, H., Leitner, K., Pammer, P., Groschner, K., Soldatov, N.
1120 M., & Romanin, C. (2000). Molecular determinant for run-down of L-type Ca^{2+}
1121 channels localized in the carboxyl terminus of the 1C subunit. *J Physiol*, 529 Pt 1,
1122 119-130. <https://doi.org/10.1111/j.1469-7793.2000.00119.x>
- 1123 Kim, J., Wei, D. S., & Hoffman, D. A. (2005). Kv4 potassium channel subunits control action
1124 potential repolarization and frequency-dependent broadening in rat hippocampal CA1
1125 pyramidal neurones. *J Physiol*, 569 (Pt 1), 41-57.
1126 <https://doi.org/10.1113/jphysiol.2005.095042>
- 1127 Kimm, T., & Bean, B. P. (2014). Inhibition of A-type potassium current by the peptide toxin
1128 SNX-482. *J Neurosci*, 34 (28), 9182-9189. [https://doi.org/10.1523/JNEUROSCI.0339-](https://doi.org/10.1523/JNEUROSCI.0339-14.2014)
1129 [14.2014](https://doi.org/10.1523/JNEUROSCI.0339-14.2014)
- 1130 Koschak, A., Reimer, D., Huber, I., Grabner, M., Glossmann, H., Engel, J., & Striessnig, J.
1131 (2001). α_1D (Cav1.3) subunits can form L-type Ca^{2+} channels activating at
1132 negative voltages. *J Biol Chem*, 276, 22100-22106.
1133 <https://doi.org/10.1074/jbc.M101469200>
- 1134 Lacey, M. G., Mercuri, N. B., & North, R. A. (1989). Two cell types in rat substantia nigra
1135 zona compacta distinguished by membrane properties and the actions of dopamine
1136 and opioids. *J Neurosci*, 9 (4), 1233-1241.
1137 <https://www.ncbi.nlm.nih.gov/pubmed/2703874>
- 1138 Lieb, A., Ortner, N., & Striessnig, J. (2014). C-terminal modulatory domain controls coupling
1139 of voltage-sensing to pore opening in Cav1.3 L-type calcium channels. *Biophys J*,
1140 106 (7), 1467-1475. <https://doi.org/10.1016/j.bpj.2014.02.017>
- 1141 Lindau, M., & Fernandez, J. M. (1986). IgE-mediated degranulation of mast cells does not
1142 require opening of ion channels. *Nature*, 319 (6049), 150-153.
1143 <https://doi.org/10.1038/319150a0>
- 1144 Link, S., Meissner, M., Held, B., Beck, A., Weissgerber, P., Freichel, M., & Flockerzi, V.
1145 (2009). Diversity and developmental expression of L-type calcium channel β_2
1146 proteins and their influence on calcium current in murine heart. *J Biol Chem*, 284 (44),
1147 30129-30137. <https://doi.org/10.1074/jbc.M109.045583>

- 1148 Liss, B. (2002). Improved quantitative real-time RT-PCR for expression profiling of individual
 1149 cells. *Nucleic Acids Res*, 30 (17), e89. <https://doi.org/10.1093/nar/gnf088>
- 1150 Liss, B., Franz, O., Sewing, S., Bruns, R., Neuhoﬀ, H., & Roeper, J. (2001). Tuning
 1151 pacemaker frequency of individual dopaminergic neurons by Kv4.3L and KChip3.1
 1152 transcription. *EMBO J*, 20 (20), 5715-5724. <https://doi.org/10.1093/emboj/20.20.5715>
- 1153 Liss, B., & Striessnig, J. (2019). The Potential of L-Type Calcium Channels as a Drug Target
 1154 for Neuroprotective Therapy in Parkinson's Disease. *Annu Rev Pharmacol Toxicol*,
 1155 59, 263-289. <https://doi.org/10.1146/annurev-pharmtox-010818-021214>
- 1156 Liu, H., De Waard, M., Scott, V. E., Gurnett, C. A., Lennon, V. A., & Campbell, K. P. (1996).
 1157 Identification of three subunits of the high affinity omega-conotoxin MVIIIC-sensitive
 1158 Ca²⁺ channel. *J Biol Chem*, 271 (23), 13804-13810.
- 1159 Matsushita, N., Okada, H., Yasoshima, Y., Takahashi, K., Kiuchi, K., & Kobayashi, K. (2002).
 1160 Dynamics of tyrosine hydroxylase promoter activity during midbrain dopaminergic
 1161 neuron development. *J Neurochem*, 82 (2), 295-304. <https://doi.org/10.1046/j.1471-4159.2002.00972.x>
- 1162
- 1163 Matt, L., Kim, K., Chowdhury, D., & Hell, J. W. (2019). Role of Palmitoylation of Postsynaptic
 1164 Proteins in Promoting Synaptic Plasticity. *Front Mol Neurosci*, 12, 8.
 1165 <https://doi.org/10.3389/fnmol.2019.00008>
- 1166 Mercuri, N. B., Bonci, A., Calabresi, P., Stratta, F., Stefani, A., & Bernardi, G. (1994). Effects
 1167 of dihydropyridine calcium antagonists on rat midbrain dopaminergic neurones. *Br J*
 1168 *Pharmacol*, 113 (3), 831-838. 7858874
- 1169 Miranda-Laferte, E., Ewers, D., Guzman, R. E., Jordan, N., Schmidt, S., & Hidalgo, P.
 1170 (2014). The N-terminal domain tethers the voltage-gated calcium channel beta2e-
 1171 subunit to the plasma membrane via electrostatic and hydrophobic interactions. *J Biol*
 1172 *Chem*, 289 (15), 10387-10398. <https://doi.org/10.1074/jbc.M113.507244>
- 1173 Morgenstern, T. J., Park, J., Fan, Q. R., & Colecraft, H. M. (2019). A potent voltage-gated
 1174 calcium channel inhibitor engineered from a nanobody targeted to auxiliary Cavbeta
 1175 subunits. *Elife*, 8. <https://doi.org/10.7554/eLife.49253>
- 1176 Neher, E. (1992). Correction for liquid junction potentials in patch clamp experiments.
 1177 *Methods Enzymol*, 207, 123-131. [https://doi.org/10.1016/0076-6879\(92\)07008-c](https://doi.org/10.1016/0076-6879(92)07008-c)
- 1178 Neuhoﬀ, H., Neu, A., Liss, B., & Roeper, J. (2002). I(h) channels contribute to the different
 1179 functional properties of identified dopaminergic subpopulations in the midbrain. *J*
 1180 *Neurosci*, 22 (4), 1290-1302. <https://www.ncbi.nlm.nih.gov/pubmed/11850457>
- 1181 Newcomb, R., Szoke, B., Palma, A., Wang, G., Chen, X., Hopkins, W., Cong, R., Miller, J.,
 1182 Urge, L., Tarczy-Hornoch, K., Loo, J. A., Dooley, D. J., Nadasdi, L., Tsien, R. W.,
 1183 Lemos, J., & Miljanich, G. (1998). Selective peptide antagonist of the class E calcium

- channel from the venom of the tarantula *Hysterocrates gigas*. *Biochemistry*, 37 (44), 15353-15362. <https://doi.org/10.1021/bi981255g>
- Ortner, N. J., Bock, G., Dougalis, A., Kharitonova, M., Duda, J., Hess, S., Tuluc, P., Pomberger, T., Stefanova, N., Pitterl, F., Ciossek, T., Oberacher, H., Draheim, H. J., Kloppenburg, P., Liss, B., & Striessnig, J. (2017). Lower Affinity of Isradipine for L-Type Ca^{2+} Channels during Substantia Nigra Dopamine Neuron-Like Activity: Implications for Neuroprotection in Parkinson's Disease. *J Neurosci*, 37 (28), 6761-6777. <https://doi.org/10.1523/JNEUROSCI.2946-16.2017>
- Ortner, N. J., Bock, G., Vandael, D. H., Mauersberger, R., Draheim, H. J., Gust, R., Carbone, E., Tuluc, P., & Striessnig, J. (2014). Pyrimidine-2,4,6-triones are a new class of voltage-gated L-type Ca^{2+} channel activators. *Nat Commun*, 5, 3897. <https://doi.org/10.1038/ncomms4897>
- Ortner, N. J., Pinggera, A., Hofer, N. T., Siller, A., Brandt, N., Raffeiner, A., Vilusic, K., Lang, I., Blum, K., Obermair, G. J., Stefan, E., Engel, J., & Striessnig, J. (2020). RBP2 stabilizes slow Cav1.3 Ca^{2+} channel inactivation properties of cochlear inner hair cells. *Pflugers Arch*, 472 (1), 3-25. <https://doi.org/10.1007/s00424-019-02338-4>
- Paladini, C. A., & Roeper, J. (2014). Generating bursts (and pauses) in the dopamine midbrain neurons. *Neuroscience*, 282, 109-121. <https://doi.org/10.1016/j.neuroscience.2014.07.032>
- Paxinos, G., & Franklin, K. B. J. (2004). *The Mouse Brain in Stereotaxic Coordinates*.
- Pereverzev, A., Leroy, J., Krieger, A., Malecot, C. O., Hescheler, J., Pfitzer, G., Klockner, U., & Schneider, T. (2002). Alternate splicing in the cytosolic II-III loop and the carboxy terminus of human E-type voltage-gated Ca^{2+} channels: electrophysiological characterization of isoforms. *Mol Cell Neurosci*, 21 (2), 352-365. <https://doi.org/10.1006/mcne.2002.1179>
- Philippart, F., Destreel, G., Merino-Sepulveda, P., Henny, P., Engel, D., & Seutin, V. (2016). Differential Somatic Ca^{2+} Channel Profile in Midbrain Dopaminergic Neurons. *J Neurosci*, 36 (27), 7234-7245. <https://doi.org/10.1523/jneurosci.0459-16.2016>
- Pinggera, A., Lieb, A., Benedetti, B., Lampert, M., Monteleone, S., Liedl, K. R., Tuluc, P., & Striessnig, J. (2015). CACNA1D de novo mutations in autism spectrum disorders activate Cav1.3 L-type calcium channels. *Biol Psychiatry*, 77 (9), 816-822. <https://doi.org/10.1016/j.biopsych.2014.11.020>
- Pruszek, J., Just, L., Isacson, O., & Nikkhah, G. (2009). Isolation and culture of ventral mesencephalic precursor cells and dopaminergic neurons from rodent brains. *Curr Protoc Stem Cell Biol*, Chapter 2, Unit 2D.5. <https://doi.org/10.1002/9780470151808.sc02d05s11>

- 1220 Puopolo, M., Raviola, E., & Bean, B. P. (2007). Roles of subthreshold calcium current and
 1221 sodium current in spontaneous firing of mouse midbrain dopamine neurons. *J*
 1222 *Neurosci*, 27 (3), 645-656. <https://doi.org/10.1523/JNEUROSCI.4341-06.2007>
- 1223 Qin, N., Platano, D., Olcese, R., Costantin, J. L., Stefani, E., & Birnbaumer, L. (1998). Unique
 1224 regulatory properties of the type 2a Ca²⁺ channel beta subunit caused by
 1225 palmitoylation. *Proc Natl Acad Sci U S A*, 95 (8), 4690-4695.
- 1226 Rae, J., Cooper, K., Gates, P., & Watsky, M. (1991). Low access resistance perforated patch
 1227 recordings using amphotericin B. *J Neurosci Methods*, 37 (1), 15-26.
 1228 [https://doi.org/10.1016/0165-0270\(91\)90017-t](https://doi.org/10.1016/0165-0270(91)90017-t)
- 1229 Richards, C. D., Shiroyama, T., & Kitai, S. T. (1997). Electrophysiological and
 1230 immunocytochemical characterization of GABA and dopamine neurons in the
 1231 substantia nigra of the rat. *Neuroscience*, 80 (2), 545-557.
 1232 [https://doi.org/10.1016/s0306-4522\(97\)00093-6](https://doi.org/10.1016/s0306-4522(97)00093-6)
- 1233 Sawamoto, K., Nakao, N., Kobayashi, K., Matsushita, N., Takahashi, H., Kakishita, K.,
 1234 Yamamoto, A., Yoshizaki, T., Terashima, T., Murakami, F., Itakura, T., & Okano, H.
 1235 (2001). Visualization, direct isolation, and transplantation of midbrain dopaminergic
 1236 neurons. *Proc Natl Acad Sci U S A*, 98 (11), 6423-6428.
 1237 <https://doi.org/10.1073/pnas.111152398>
- 1238 Schiemann, J., Schlaudraff, F., Klose, V., Bingmer, M., Seino, S., Magill, P. J., Zaghloul, K.
 1239 A., Schneider, G., Liss, B., & Roeper, J. (2012). K-ATP channels in dopamine
 1240 substantia nigra neurons control bursting and novelty-induced exploration. *Nat*
 1241 *Neurosci*, 15 (9), 1272-1280. <https://doi.org/10.1038/nn.3185>
- 1242 Schindelin, J., Arganda-Carreras, I., Frise, E., Kaynig, V., Longair, M., Pietzsch, T.,
 1243 Preibisch, S., Rueden, C., Saalfeld, S., Schmid, B., Tinevez, J.-Y., White, D. J.,
 1244 Hartenstein, V., Eliceiri, K., Tomancak, P., & Cardona, A. (2012). Fiji: an open-source
 1245 platform for biological-image analysis. *Nature Methods*, 9 (7), 676-682.
 1246 <https://doi.org/10.1038/nmeth.2019>
- 1247 Schlick, B., Flucher, B. E., & Obermair, G. J. (2010). Voltage-activated calcium channel
 1248 expression profiles in mouse brain and cultured hippocampal neurons. *Neuroscience*,
 1249 167 (3), 786-798. <https://doi.org/10.1016/j.neuroscience.2010.02.037>
- 1250 Schneider, T., Alpdogan, S., Hescheler, J., & Neumaier, F. (2018). In vitro and in vivo
 1251 phosphorylation of the Cav2.3 voltage-gated R-type calcium channel. *Channels*
 1252 *(Austin)*, 12 (1), 326-334. <https://doi.org/10.1080/19336950.2018.1516984>
- 1253 Schneider, T., Dibue, M., & Hescheler, J. (2013). How "Pharmacoresistant" is Cav2.3, the
 1254 Major Component of Voltage-Gated R-type Ca²⁺ Channels? *Pharmaceuticals*
 1255 *(Basel)*, 6 (6), 759-776. <https://doi.org/10.3390/ph6060759>

- 1256 Scott, V. E. S., De Waard, M., Liu, H., Gurnett, C. A., Venzke, D. P., Lennon, V. A., &
 1257 Campbell, K. P. (1996). Beta subunit heterogeneity in N-type calcium channels. *J Biol*
 1258 *Chem*, 271, 3207-3212. <https://doi.org/10.1074/jbc.271.6.3207>
- 1259 Shin, W. (2015). *RNASeq of DA neurons from SNpc and VTA. Dataset posted on*
 1260 *04.03.2015, 16:01 by William Shin.*
 1261 https://figshare.com/articles/RNASeq_of_DA_neurons_from_SNpc_and_VTA/926519
- 1262
- 1263 Sochivko, D., Pereverzev, A., Smyth, N., Gissel, C., Schneider, T., & Beck, H. (2002). The
 1264 Ca(V)2.3 Ca(2+) channel subunit contributes to R-type Ca(2+) currents in murine
 1265 hippocampal and neocortical neurones. *J Physiol*, 542 (Pt 3), 699-710.
 1266 <https://doi.org/10.1113/jphysiol.2002.020677>
- 1267 Soong, T. W., Stea, A., Hodson, C. D., Dubel, S. J., Vincent, S. R., & Snutch, T. P. (1993).
 1268 Structure and functional expression of a member of the low voltage-activated calcium
 1269 channel family. *Science*, 260 (5111), 1133-1136.
 1270 <https://doi.org/10.1126/science.8388125>
- 1271 Subramaniam, M., Althof, D., Gispert, S., Schwenk, J., Auburger, G., Kulik, A., Fakler, B., &
 1272 Roeper, J. (2014). Mutant α -synuclein enhances firing frequencies in dopamine
 1273 substantia nigra neurons by oxidative impairment of A-type potassium channels. *J*
 1274 *Neurosci*, 34, 13586-13599. <https://doi.org/10.1523/JNEUROSCI.5069-13.2014>
- 1275 Surmeier, D. J., Guzman, J. N., Sanchez-Padilla, J., & Goldberg, J. A. (2011). The origins of
 1276 oxidant stress in Parkinson's disease and therapeutic strategies. *Antioxid Redox*
 1277 *Signal*, 14 (7), 1289-1301. <https://doi.org/10.1089/ars.2010.3521>
- 1278 Surmeier, D. J., Obeso, J. A., & Halliday, G. M. (2017). Selective neuronal vulnerability in
 1279 Parkinson disease. *Nat Rev Neurosci*, 18, 101-113.
 1280 <https://doi.org/10.1038/nrn.2016.178>
- 1281 Tomagra, G., Picollo, F., Battiato, A., Picconi, B., De Marchis, S., Pasquarelli, A., Olivero, P.,
 1282 Marcantoni, A., Calabresi, P., Carbone, E., & Carabelli, V. (2019). Quantal Release of
 1283 Dopamine and Action Potential Firing Detected in Midbrain Neurons by
 1284 Multifunctional Diamond-Based Microarrays. *Front Neurosci*, 13, 288.
 1285 <https://doi.org/10.3389/fnins.2019.00288>
- 1286 Tottene, A., Volsen, S., & Pietrobon, D. (2000). α 1E subunits form the pore of three
 1287 cerebellar R-type calcium channels with different pharmacological and permeation
 1288 properties. *J Neurosci*, 20 (1), 171-178. [https://doi.org/10.1523/JNEUROSCI.20-01-](https://doi.org/10.1523/JNEUROSCI.20-01-00171.2000)
 1289 [00171.2000](https://doi.org/10.1523/JNEUROSCI.20-01-00171.2000)
- 1290 Tringham, E., Powell, K. L., Cain, S. M., Kuplast, K., Mezeyova, J., Weerapura, M., Eduljee,
 1291 C., Jiang, X., Smith, P., Morrison, J. L., Jones, N. C., Braine, E., Rind, G., Fee-Maki,
 1292 M., Parker, D., Pajouhesh, H., Parmar, M., O'Brien, T. J., & Snutch, T. P. (2012). T-

- 1293 type calcium channel blockers that attenuate thalamic burst firing and suppress
 1294 absence seizures. *Sci Transl Med*, 4 (121), 121ra119.
 1295 <https://doi.org/10.1126/scitranslmed.3003120>
- 1296 Vandesompele, J., De Preter, K., Pattyn, F., Poppe, B., Van Roy, N., De Paepe, A., &
 1297 Speleman, F. (2002). Accurate normalization of real-time quantitative RT-PCR data
 1298 by geometric averaging of multiple internal control genes. *Genome Biol*, 3 (7),
 1299 research0034.0031. <https://doi.org/10.1186/gb-2002-3-7-research0034>
- 1300 Wang, G., Dayanithi, G., Newcomb, R., & Lemos, J. R. (1999). An R-type Ca(2+) current in
 1301 neurohypophysial terminals preferentially regulates oxytocin secretion. *J Neurosci*, 19
 1302 (21), 9235-9241. <https://doi.org/10.1523/JNEUROSCI.19-21-09235.1999>
- 1303 Watanabe, M., Sakuma, Y., & Kato, M. (2004). High Expression of the R-Type Voltage-
 1304 Gated Ca²⁺ Channel and Its Involvement in Ca²⁺-Dependent Gonadotropin-
 1305 Releasing Hormone Release in GT1-7 Cells. *Endocrinology*, 145 (5), 2375-2383.
 1306 <https://doi.org/10.1210/en.2003-1257>
- 1307 Weiergraber, M., Henry, M., Sudkamp, M., de Vivie, E. R., Hescheler, J., & Schneider, T.
 1308 (2005). Ablation of Ca(v)2.3 / E-type voltage-gated calcium channel results in cardiac
 1309 arrhythmia and altered autonomic control within the murine cardiovascular system.
 1310 *Basic Res Cardiol*, 100 (1), 1-13. <https://doi.org/10.1007/s00395-004-0488-1>
- 1311 Williams, M. E., Marubio, L. M., Deal, C. R., Hans, M., Brust, P. F., Philipson, L. H., Miller, R.
 1312 J., Johnson, E. C., Harpold, M. M., & Ellis, S. B. (1994). Structure and functional
 1313 characterization of neuronal alpha1E calcium channel subtypes. *J Biol Chem*, 269,
 1314 22347-22357.
- 1315 Wilson, S. M., Toth, P. T., Oh, S. B., Gillard, S. E., Volsen, S., Ren, D., Philipson, L. H., Lee,
 1316 E. C., Fletcher, C. F., Tessarollo, L., Copeland, N. G., Jenkins, N. A., & Miller, R. J.
 1317 (2000). The status of voltage-dependent calcium channels in alpha 1E knock-out
 1318 mice. *J Neurosci*, 20 (23), 8566-8571. <https://doi.org/10.1523/JNEUROSCI.20-23-08566.2000>
- 1320 Xu, W., & Lipscombe, D. (2001). Neuronal Ca_v1.3α1 L-type channels activate at relatively
 1321 hyperpolarized membrane potentials and are incompletely inhibited by
 1322 dihydropyridines. *J Neurosci*, 21 (16), 5944-5951.
 1323 <https://doi.org/10.1523/JNEUROSCI.21-16-05944.2001>
- 1324 Yasuda, T., Chen, L., Barr, W., McRory, J. E., Lewis, R. J., Adams, D. J., & Zamponi, G. W.
 1325 (2004). Auxiliary subunit regulation of high-voltage activated calcium channels
 1326 expressed in mammalian cells. *Eur J Neurosci*, 20 (1), 1-13.
 1327 <https://doi.org/10.1111/j.1460-9568.2004.03434.x>
- 1328 Ye, J. H., Zhang, J., Xiao, C., & Kong, J. Q. (2006). Patch-clamp studies in the CNS illustrate
 1329 a simple new method for obtaining viable neurons in rat brain slices: glycerol

- 1330 replacement of NaCl protects CNS neurons. *J Neurosci Methods*, 158 (2), 251-259.
1331 <https://doi.org/10.1016/j.jneumeth.2006.06.006>
1332 Zamponi, G. W., Striessnig, J., Koschak, A., & Dolphin, A. C. (2015). The Physiology,
1333 Pathology, and Pharmacology of Voltage-Gated Calcium Channels and Their Future
1334 Therapeutic Potential. *Pharmacol Rev*, 67 (4), 821-870.
1335 <https://doi.org/10.1124/pr.114.009654>
1336

Figure legends

Figure 1. Biophysical properties of Cav2.3 channels co-transfected with different β -subunits (and $\alpha 2\delta 1$) in tsA-201 cells.

A. Current densities (pA/pF) with or without (gray) co-transfection of indicated β -subunits. Color code and n-numbers are given in the graphs. **B.** Voltage-dependence of steady-state activation (normalized conductance G , right axis, solid lines) and inactivation (normalized I_{Ca} of test pulses, left axis, dashed lines, left n-numbers in parentheses). **C.** Inactivation time course during 5 s depolarizing pulses to V_{max} starting from a holding potential of -119 mV. Inset shows the first 200 ms of the 5 s pulse. Respective stimulation protocols are shown above each graph. The curves represent the means \pm SEM for the indicated number of experiments ($N = \beta 2a: 5; \beta 2d, \beta 2e: 2; \beta 3, \beta 4, \text{no } \beta: 3$). For statistics see Table 1. V_{max} , voltage of maximal inward current. **D.** Window currents measured in the presence of the indicated β -subunits were calculated by multiplying mean current densities (pA/pF) of I - V -relationships by the fractional current inactivation from steady-state inactivation curves at the indicated voltages. Data represent the means \pm SEM for the indicated number of experiments ($N = \beta 2a: 5; \beta 2d, \beta 2e: 2; \beta 3, \beta 4: 3$). Statistical significance was determined using one-way ANOVA with Bonferroni post-hoc test and is indicated: *** $p < 0.001$; ** $p < 0.01$; * $p < 0.05$. Source data provided in Figure 1-Source Data 1.xlsx.

Figure 2. Transcript expression of various β -subunits and $\beta 2$ -subunit splice variants in mouse SN and VTA tissue.

A. Expression of $\beta 1$ - $\beta 4$ subunit transcripts in SN ($n=3, N=3$) (left) and VTA ($n=3, N=3$) (right) determined by RT-qPCR as described in Methods. **B.** Expression of $\beta 2a$ - $\beta 2e$ subunit transcripts in SN ($n=3, N=3$) (left) and VTA ($n=3, N=3$) (right). Data are shown as the mean \pm SEM. Statistical significance was determined using one-way ANOVA followed by Bonferroni post-hoc test: *** $p < 0.001$; ** $p < 0.01$; * $p < 0.05$. Data was normalized to *Gapdh* and *Tfrc* determined by geNorm.

C. Example for four SN (left) and two VTA (right) tissue punches obtained for cDNA preparation with diameters of 0.5 mm each (left) or 0.8 mm each (right) from 7-8 successive 100- μ m-sections between Bregma -3.00 mm and -3.80 mm, stained with Cresyl violet.

Source data provided in Figure 2-Source Data 1.xlsx.

Figure 3. Activity-dependent inactivation of Cav2.3 channels co-transfected with different β subunits (and $\alpha 2\delta 1$) during simulated SN DA neuron regular pacemaking activity in tsA-201 cells.

A-D. Top panel: The SN DA neuron-derived command voltage was applied with a frequency of 2.5 Hz (only a time interval around the AP-spike is shown). Middle panel: Corresponding representative Ca^{2+} current traces (2 mM charge carrier) for Cav2.3 channels co-expressed with $\alpha 2\delta 1$ and $\beta 3$ (A, green), $\beta 4$ (B, purple), $\beta 2a$ (C, orange) or $\beta 2e$ (D, blue) are shown for the indicated sweep number (1st, 10th, 100th, 295th, 720th). Cav2.3 currents were completely blocked by 100 μM Cadmium (Cd^{2+}), and remaining Cd^{2+} -insensitive current components were subtracted off-line (bottom panel). ISI, interspike interval. **E.** Current decay during simulated 2.5 Hz SN DA neuron pacemaking. Normalized peak inward current during APs (I_{AP}) is plotted against time as mean \pm SEM for the indicated number of experiments. I_{AP} amplitudes were normalized to the I_{AP} amplitude of the first AP after holding the cell at -89 mV. Cav1.3_L co-expressed with $\alpha 2\delta 1$ and $\beta 3$ (gray, mean only) is shown for comparison (data taken from Ortner et al., 2017). The I_{AP} decay was fitted to a bi-exponential function (Cav2.3 $\beta 3$: $A_{\text{slow}} = 39.4 \pm 0.65\%$, $\tau_{\text{slow}} = 22.2 \pm 0.15$ min, $A_{\text{fast}} = 54.2 \pm 0.76\%$, $\tau_{\text{fast}} = 2.86 \pm 0.07$ min, non-inactivating = $4.47 \pm 0.13\%$; $\beta 4$: $A_{\text{slow}} = 48.5 \pm 0.26\%$, $\tau_{\text{slow}} = 90.3 \pm 1.07$ min, $A_{\text{fast}} = 41.8 \pm 0.40\%$, $\tau_{\text{fast}} = 8.39 \pm 0.16$ min, non-inactivating = $5.12 \pm 0.12\%$; $\beta 2a$: $A_{\text{slow}} = 52.6 \pm 0.47\%$, $\tau_{\text{slow}} = 299.3 \pm 10.2$ min, $A_{\text{fast}} = 13.4 \pm 0.53\%$, $\tau_{\text{fast}} = 18.2 \pm 1.47$ min, non-inactivating = $32.3 \pm 0.77\%$; $\beta 2e$: $A_{\text{slow}} = 67.7 \pm 0.11\%$, $\tau_{\text{slow}} = 294.1 \pm 1.77$ min, $A_{\text{fast}} = 7.10 \pm 0.27\%$, $\tau_{\text{fast}} = 16.6 \pm 1.24$ min, non-inactivating = $25.0 \pm 0.12\%$). Curves represent the means \pm SEM for the indicated number of experiments (independent transfections, N = Cav2.3/ $\beta 3$: 4; Cav2.3/ $\beta 4$: 2; Cav2.3/ $\beta 2a$: 4; Cav2.3/ $\beta 2e$: 2; Cav1.3_L/ $\beta 3$: 6). **C.** Normalized I_{AP} decay after predefined time points for Cav2.3 with $\beta 3$, $\beta 4$, $\beta 2a$ or $\beta 2e$ and Cav1.3_L (with $\beta 3$). Color-code and n-numbers as in panel E. Statistical significance was determined using one-way ANOVA followed by Bonferroni post-hoc test: *** $p < 0.001$; ** $p < 0.01$; * $p < 0.05$.

Source data provided in Figure 3-Source Data 1.xlsx.

Figure 4. β -subunit-dependent run-down of Cav2.3 channel Ca^{2+} current in tsA-201 cells.

Data for Cav2.3 co-expressed with $\alpha 2\delta 1$ and $\beta 2a$ (orange) or $\beta 3$ (green) are shown. **A.** Run-down during a 0.1 Hz square pulse protocol (20 ms to V_{max} , hp -89 mV). Currents were normalized to the I_{Ca} of the sweep with the maximal peak inward current observed during the recording. After a full block with 100 μM Cd^{2+} currents recovered to the amplitude preceding the Cd^{2+} application. **B.** Cells were held at -89 mV and then stimulated using the regular SN DA neuron pacemaking protocol for 30 s, 1 min, and 2 min each followed by 20 s long pauses (vertical dashed lines) at hyperpolarized potentials (-89 mV) to allow channel

recovery from inactivation. I_{AP} of individual APs was normalized to the inward current of the first AP. The current run-down component can be estimated from the non-recovering current component (horizontal dashed lines). Traces represent means \pm SEM from the indicated number of experiments (N=2). BS, bath solution.

Figure 5. Effects of different β -subunits on Cav2.3 currents during a simulated SN DA neuron three-spike burst and post-burst APs in tsA-201 cells.

The burst command voltage was elicited after ~5-6 min (β 2a, β 2e) or ~1-2 min (β 4) of regular pacemaking to reach steady-state I_{AP} (β 2a and β 2e: ~30% of the initial I_{AP} , β 4: ~6% of the initial I_{AP} , see Figure 3). **A.** Normalized current responses of Cav2.3 channels co-expressed with β 2a, β 2e or β 4 subunits (and α 2 δ 1) induced by a command voltage (top panel) simulating a typical three-spike burst followed by a hyperpolarization phase at hyperpolarized potentials (lowest voltage: -82 mV) for 1.5 seconds. Remaining Cd^{2+} -insensitive current components (100 μ M Cd^{2+}) were subtracted off-line to extract pure Cav2.3 mediated I_{Ca} . One of at least four experiments with similar results is shown. **B.** The integrated I_{Ca} during a single AP before the burst (obtained as the mean of the three preceding APs) was set to 100 % and compared with I_{Ca} during the three-spike burst integrated over the time period equivalent to one AP (left) or the first APs after the pause (right). All investigated β -subunits resulted in increased integrated I_{Ca} during the burst. Data represent the means \pm SEM for the indicated number of experiments (N = β 2a: 4; β 2e: 2; β 4: 2). Statistical significance was determined using one-way ANOVA followed by Bonferroni post-test (whole burst) or Kruskal-Wallis followed by Dunn's multiple comparison test (post-burst APs): *** $p < 0.001$; ** $p < 0.01$; * $p < 0.05$. **C.** Square-pulse protocol (top) used to determine recovery from inactivation after the indicated time intervals for β 2a and β 4-associated Cav2.3 channels (see Methods for details). Data represent the means \pm SEM for the indicated number of experiments (N=3). For statistics see Table 2.

Source data provided in Figure 5-Source Data 1.xlsx.

Figure 6. Voltage-dependence of gating of R-type currents in mouse SN DA neurons recorded in brain slices.

A. I_{Ca} recorded in SN DA neurons without (Control, black, n=16) or after preincubation ("R-type", blue, n=19) of slices with a Cav channel blocker cocktail to inhibit Cav3 (10 μ M Z941), Cav1 (1 μ M I), Cav2.1 and Cav2.2 (1 μ M ω -conotoxin-MVIIC) (see Methods). Left panel: representative current traces of recordings at -20 mV test potentials (hp -100 mV); notice that similar amplitudes of control and R-type current were chosen to facilitate comparison of current kinetics. Right panel: voltage-dependence of steady-state activation and inactivation,

curve fits to a Boltzman equation of all individual data points are shown. Data are means \pm SEM. For parameters and statistics see Table 3. **B.** SNX-482-sensitive currents (light blue) were obtained by subtracting current measured in the presence of SNX-482 (green) from the respective control I_{Ca} before addition of SNX-482 (black) (n=9). Left panel: Representative recording of a SNX-482 sensitive current component compared to the respective control (hp -100 mV, -10 mV test potential). Steady-state activation and inactivation of control and SNX-482-sensitive current. Test protocols: hp -100 mV; voltage-dependence of activation: 150 ms test potentials to indicated voltages; voltage-dependence of inactivation: 5-s conditioning pulses to indicated voltages preceded ($I_{control}$) and followed by 20-ms test pulses to V_{max} . **C.** Exemplary neuron as seen under the patch-clamp microscope with patch pipette next to it (left; BF, brightfield) and a neuron after histochemical staining for tyrosine hydroxylase (TH, green) and neurobiotin (Nb, red). Detailed parameters and statistics are given in Table 3. Source data provided in Figure 6-Source Data 1.xlsx.

Figure 7. SNX-482-sensitive R-type currents in cultured mouse midbrain DA neurons.

A. Representative traces illustrating the inhibition of non-L-type I_{Ca} by 100 nM SNX-482 (red). Cells were initially perfused with a bath solution containing 3 μ M isradipine (black). Full block was obtained using 2 μ M Cd^{2+} (blue). Square pulses (50 ms) were applied to 0 mV from a holding potential of -70 mV (top). **B.** Current amplitude values plotted as a function of time. After stabilization of I_{Ca} with ISR (black circles), 100 nM SNX-482 was applied. The remaining currents was blocked by 2 μ M Cd^{2+} . Current run-down in the absence of drugs during 150 s was less than 1% ($0.48 \pm 0.18\%$; n=4 cells). **C.** SNX-482 inhibition expressed as % of control I_{Ca} after LTCC block using 3 μ M ISR. **D.** Mean current amplitude at the end of ISR application and at the end of SNX-482 application. Absolute current amplitude decreased from 529 ± 57 pA (95% CI: 409-649) to 313 ± 33 pA (95% CI: 245-381, n=20, $p < 0.01$, paired Students t-test). Data represent the means \pm SEM for the indicated number of experiments (N=4). Statistical significance was determined using paired Student's t-test: *** $p < 0.001$; ** $p < 0.01$; * $p < 0.05$.

E. Left: Depolarizations of 50 ms were repeated every 10 s to the indicated potentials from a holding potential, hp, of -70 mV (inset). The voltage dependence of the conductance, $g(V)$, was calculated with the equation $g(V) = I_{Ca}/(V - E_{Ca})$ with $E_{Ca} = +65$ mV for the currents recorded in the presence of 3 μ M ISR (control; black squares; n=9-14 per voltage) and after subtraction of the currents insensitive to 100 nM SNX-482 (n=4-7) to yield (SNX-sensitive R-type; blue circles). Data were fitted to a Boltzman function. At each test potential (V) I_{Ca} was estimated at the peak of the current trace. Right: representative current traces recorded during pulses to -50, -40, -30 and 0 mV. **F.** Left: To determine the voltage-dependence of steady-state inactivation, test pulses of 50 ms to 0 mV were preceded by 1 min prepulses to

voltages from -80 to -10 mV. This stimulation protocol (inset) was better tolerated by cultured DA midbrain neurons than the classical protocol used previously with other cells (Calorio et al., 2019; Pinggera et al., 2015). SNX-sensitive R-type currents (blue) were obtained after subtraction of the currents insensitive to 100 nM SNX-482 ($n=3-8$ per voltage) from non-L control current (black, $n=8-15$). Right: representative traces recorded at 0 mV from a hp of -20, -40, -60, and -80 mV. Inactivation curves could be best fit to Boltzman functions with the following parameters: R-type: $V_{0.5,inact} = -58.1 \pm 0.6$ mV, $k = -7.1 \pm 1.2$ mV; control: $V_{0.5,inact} = -48.0 \pm 0.9$ mV, $k = -11.1 \pm 1.2$ mV. The R-type currents (E, F) appear smaller than expected from the data in panels B and C (30-40% of non-L-type currents). This is due to a run-down of SNX-sensitive current during the repeated depolarizations used to determine the voltage-dependence of gating. This has only minimal effects on gating parameters. When accounting for a linear run-down of 40%, the $V_{0.5,act}$ would shift only from -58 to -56 mV. Source data provided in Figure 7-Source Data 1.xlsx.

1493

1494

Legends to figure supplements

Figure 1-figure supplement 1. Determination of the expressed Cav2.3 splice variants in SN DA neurons.

A. Cartoon of the exon structure of all Cav2.3 splice variants. The murine *Cacna1e* gene, coding for the Cav2.3 α 1-subunits contains 48 exons with six major alternative splice variants (right panel). The splicing events include the variable use of exon 19, 21 nucleotides of exon 20 and exon 45. The outer and inner primer pairs chosen for identification of the different splice variants are located in the II-III loop and the C-terminus, covering the three described splicing sites. Expressed exons are shown as white boxes and splicing sites are indicated in red. **B.** Agarose gel electrophoresis image showing two PCR products (363 bp II-III loop nested PCR fragment and 498 bp C-terminus nested PCR fragment) coding for the Cav2.3e splice variant of Cav2.3 (*Cacna1e*) found in mouse laser-dissected SN DA neuron derived cDNA (n=40, left). In contrast, all five PCR products (363 bp, 399 bp and 420 bp in the II-III loop and 369 bp and 498 bp in the C-terminus nested PCR fragments) coding for all six major splice variants were found in whole brain tissue-derived cDNA (as positive control, right panel).

Figure 1-figure supplement 2: Effect of β 2a palmitoylation on the biophysical properties of Cav2.3 and Cav1.3 Ca^{2+} channels in tsA-201 cells.

Since palmitoylation is reversible and regulated in an activity-dependent localized manner (Bijlmakers & Marsh, 2003; Matt et al., 2019), we also investigated the contribution of palmitoylation of β 2a for Cav2.3e modulation under our experimental conditions. To mimic the de-palmitoylated form, we replaced the two N-terminal cysteines to serines ($\text{C}_{3\text{S}}/\text{C}_{4\text{S}}\beta$ 2a) which prevents plasma membrane anchoring of β 2a (Gebhart et al., 2010; Qin et al., 1998).

Data are shown for Cav1.3 (C-terminally long splice variant, Bock et al., 2011) or Cav2.3 α 1-subunits co-expressed with α 2 δ 1 and β 2a (orange), $\text{C}_{3\text{S}}/\text{C}_{4\text{S}}\beta$ 2a (red) or β 3 (green). Respective command voltages are given in each panel. To disrupt palmitoylation-mediated membrane anchoring, the two N-terminal cysteines of β 2a (see Figure 2-figure supplement 1) were replaced by serines in $\text{C}_{3\text{S}}/\text{C}_{4\text{S}}\beta$ 2a. **A, B.** Inactivation kinetics during a 5 s long depolarizing step to V_{max} for Cav1.3_L (**A**, 15 mM Ca^{2+} , hp -89 mV) or Cav2.3 (**B**, 2 mM Ca^{2+} , hp -119 mV). Curves represent means \pm SEM for the indicated number of experiments. For statistics see Table 1 and Supplementary file 6. **C, D.** Voltage-dependence of activation (solid lines, normalized conductance G) and inactivation (dashed lines, normalized I_{Ca} of 20 ms test pulses) for Cav1.3_L (**C**, 15 mM Ca^{2+} , hp -89 mV) or Cav2.3 (**D**, 2 mM Ca^{2+} , hp -119 mV). Means \pm SEM. For statistics see Table 1 and Supplementary file 6.

$\beta 2a$ significantly shifted $V_{0.5, \text{inact}}$ of Cav2.3 to more positive voltages as compared to $\beta 3$ but to a much smaller extent (< 14 mV) than $\beta 2a$ (+35 mV) (Table 1). Due to this prominent role of palmitoylation on the $V_{0.5, \text{inact}}$ of Cav2.3 channels, the palmitoylation state of $\beta 2a$ should allow further fine-tuning of non-inactivating current components of Cav2.3 channels in SN DA neurons. The effects of $\beta 2a$ palmitoylation on the inactivation kinetics and inactivation voltage of Cav1.3 L-type channels (A, C) were different from Cav2.3, suggesting that palmitoylation/depalmitoylation events would regulate Ca^{2+} channel function in a subtype-selective manner. Unlike $\beta 2a$, $\text{C3S/C4S}\beta 2a$ was unable to slow the inactivation time course of Cav1.3, thus stabilizing faster inactivation similar to $\beta 3$ (Supplementary file 6, Gebhart et al., 2010). In contrast, preventing palmitoylation of $\beta 2a$ did not affect the inactivation time course of Cav2.3e (Table 1). Moreover, unlike observed for Cav2.3, steady-state inactivation was not significantly different for Cav1.3 co-transfected with $\beta 2a$, $\beta 3$, or $\text{C3S/C4S}\beta 2a$ (Supplementary file 6). Source data provided in Figure 1-figure supplement 2-Source Data 1.xlsx.

Figure 2-figure supplement 1: Binding specificity of $\beta 1$ - $\beta 4$ and $\beta 2a$ - $\beta 2e$ TaqMan assays and expression stability of endogenous control genes.

A. Alignment of the N-terminal amino acid sequence of the investigated β -subunits ($\beta 2a$, $\beta 2d$, $\beta 2e$, $\beta 3$ or $\beta 4$). Residues responsible for membrane anchoring of $\beta 2a$ (palmitoylated cysteine residues are highlighted in orange) and $\beta 2e$ (positively charged amino acids forming a lipid binding motif are highlighted in blue) are indicated. Homologous exons are shaded in grey. Sequence accession numbers (human *CACNB2* ($\beta 2$) splice variants): $\beta 2a$ (NP_000715.2), $\beta 2d$ (NP_963887.2), $\beta 2e$ (NP_963864.1), $\beta 3$ (NP_000716.2), $\beta 4e$ (NP_001307651.1). **B.** The indicated β -subunit isoforms ($\beta 1$ - $\beta 4$; $n=3$; gene names in parenthesis) and $\beta 2$ splice variants ($n=3$) were recognized with high specificity (low CT value) by the corresponding RT-qPCR assay even in the presence of a 10-fold higher concentration of the mismatching DNA fragments corresponding to other isoforms/splice variants ($\beta 1$ -4: $n=1$; $\beta 2$ splice variants: $n=1$). High binding specificity was confirmed by inefficient detection (high CT value) of all non-matching DNA fragments. We additionally performed experiments with a mixture of the specific with mismatching β -subunit DNA at ratios of 1:1, 1:2, and 1:5, and only the 1:10 mix is shown (similar CT values for all combinations). **C.** Average expression stability of endogenous control genes in SN and VTA tissue. All reference genes maintained comparable cDNA concentrations throughout the experiments. Data were normalized to the expression of Glyceraldehyde 3-phosphate dehydrogenase (*Gapdh*) and Transferrin receptor (*Tfrc*) determined by geNorm. Data are given as means \pm SEM ($n=6$, $N=6$).

Source data provided in Figure 2-figure supplement 1-Source Data 1.xlsx.

1568

Figure 2-figure supplement 2: Expression of β 2-subunit splice variants in UV-LMD SN DA neurons.

A. Left: Overview of a cresyl violet (CV) stained coronal midbrain section of a juvenile wildtype mouse after UV-LMD of 10 SN DA neurons (scale bar: 250 μ m, upper). Image of one CV stained SN DA neuron of a juvenile wildtype mouse before and after UV-LMD (scale bar: 10 μ m, lower). Middle: β 2-subunit transcript relative mRNA quantification by reverse transcription quantitative PCR-based in UV-LMD mouse SN DA neurons (n = 10). Right: Capillary gel electrophoresis image illustrating PCR products of β 2-subunit (*Cacnb2*) splice variants amplified from a UV-LMD cDNA template corresponding to 2.9 cells. **B.** Left: Representative images showing β 2a and β 2e (red) or tyrosine hydroxylase (TH (*Th*), green) RNAScope fluorescence signals (combined with nuclear DAPI staining, blue) of individual SN DA neurons from an adult wildtype mouse. Scale bar: 5 μ m. Right: Absolute mRNA transcript numbers per cell for β 2 (*Cacnb2*) - variants β 2a or β 2e in adult SN DA and VTA DA neurons of adult wildtype mice (N = 6, each), as indicated. Tukey's boxplots are shown. Significances are indicated by asterisks: *** p < 0.001, **** p < 0.0001. For statistics see details in Supplementary file 4.

Source data provided in Figure 2-figure supplement 2-Source Data1.xlsx.

Figure 6-figure supplement 1: Inhibition of I_{Ca} in SN DA neurons of adult (12 weeks) mice by 100 nM SNX-482.

To further prove the presence of SNX-482-sensitive R-type currents in SN DA neurons we performed perforated-patch recordings. These allow stable recordings over a long period of time and to test for reversibility of channel block by 100 nM SNX-482. Recordings were performed with the pulse protocol shown in A (holding potential -60 mV) after blocking I_A K^+ -currents known to be present in these cells to exclude block of I_A by SNX-482 (Kimm & Bean, 2014) as described previously (Benkert et al., 2019). 100 nM SNX-482 significantly reduced current to $87 \pm 4\%$ of control I_{Ca} (n=8, p=0.012, one-sample t-test, for statistics see Supplementary file 7) and this inhibition was slowly reversible. **A.** I_{Ca} before (black), during (red) and after (blue) SNX-482 application. **B.** Example of peak I_{Ca} plotted over time during SNX-482 application. The asterisks mark the time points of the recordings shown on the left. Single depolarizing voltage steps to 0 mV were applied from a holding potential of -60 mV every 10 s. **C.** Mean effect of SNX-482 on peak I_{Ca} . *, p<0.05 (n=8; two-tailed paired t-test). **D.** Remaining peak I_{Ca} after SNX-482 inhibition. *, p<0.05 (two-tailed one sample t-test). Box plots: Whiskers indicate minimal and maximal values, '+'-sign: mean, horizontal line: median. No complete concentration-response curves were generated since higher concentrations of SNX-482 are known to also inhibit other Cav channels (Bourinet et al., 2001; Newcomb et al., 1998). Therefore, our experiments may underestimate the overall contribution of Cav2.3

channel to total I_{Ca} , also because a fraction of channels must already be inactivated at the selected holding potential (-60 mV) of these experiments.

E-H. Under identical experimental conditions, nifedipine reduced I_{Ca} to $90 \pm 1.4\%$ of control ($p=0.031$, Wilcoxon-test, for statistics see Supplementary file 7), and this inhibition was fully reversible. **E.** Perforated patch-clamp recording of I_{Ca} before (black), during (red) and after (blue) nifedipine application. **F.** Example of peak I_{Ca} plotted over time during nifedipine application. The asterisks mark the time points of the recordings shown on the left. Single depolarizing voltage steps to -10 mV were applied from a holding potential of -60 mV every 10 s. **G.** Mean effect of nifedipine on peak I_{Ca} . *, $p<0.05$ ($n=6$; two-tailed paired t-test). **H.** Remaining peak I_{Ca} under nifedipine. $p<0.05$ (two-tailed Wilcoxon signed-rank test). Box plots: Whiskers indicate minimal and maximal values, '+'-sign: mean, horizontal line: median. For statistics see Supplementary file 7.

I. Current clamp recording of a DA neuron in the SN pars compacta to demonstrate the pre-identifying electrophysiological properties including sag potential during hyperpolarization, broad action potentials, and regular pacemaking. Arrowhead: largely reduced slow afterhyperpolarization due to partial block of K^+ channels by Cs^+ diffusion into the neuron during the perforation process. **J.** Post recording analysis shows co-localization of biocytin (recorded neuron; magenta) and tyrosine hydroxylase (TH, green).

Source data provided in Figure 6-figure supplement 1-Source Data1.xlsx.

Figure 7-figure supplement 1: SNX-482 effects on pacemaking of cultured mouse midbrain DA neurons.

A. Representative recording of spontaneous firing activity of cultured midbrain dopaminergic neurons before, during and after the application (wash-out) of 100 nM SNX-482. Below, enlargements of action potentials within the highlighted regions are shown. **B.** Firing frequency [Hz], coefficient of variation of the interspike interval [%], and AHP peak [mV] before (control) and during the application of 100 nM SNX-482. Data represent the means \pm SEM for the indicated number of experiments. Statistical significance was determined using paired Student's t-test.: *** $p<0.001$; ** $p<0.01$; * $p<0.05$. **C.** Left panel: Phase-plane plot analysis (time derivative of voltage (dV/dt) vs. voltage (V)) before (control) and during the application of 100 nM SNX-482. Right panel: corresponding AP trace in control and in the presence of SNX-482 (obtained from trace in panel A, as indicated by the asterisks).

SNX-482 significantly reduced the spontaneous firing frequency from 4.1 ± 0.8 Hz (control, $n=10$, $N=3$; 95% CI: 2.1-6.1) to 1.1 ± 0.2 Hz (SNX-482, $n=10$, 95% CI: 0.2-2.1, $p=0.0036$, paired Student's t-test) and decreased the regularity of pacemaking (coefficient of variation of the mean interspike interval increased from 0.25 ± 0.06 (control, 95% CI: 0.15-0.39) to 0.78 ± 0.13 (SNX-482, 95% CI: 0.49-1.09, $p=0.0032$, paired Student's t-test). Slowing of firing was

associated with hyperpolarization of the most negative voltage reached during the afterhyperpolarization (AHP) immediately after the spike (AHP peak), which decreased from -43.2 ± 1.3 mV (control, 95% CI: -45.8 - -40.7) to -47.0 ± 1.2 mV (SNX-482, 95% CI: -49.4 - -44.6 , $p=0.0005$, paired Student's t-test). Other changes in the AP waveform, which could represent indirect effects from the slowing of AP frequency or result from inhibition of Cav2.3 channels, were also noted: a reduced mean AP half-width (control: 5.1 ± 0.3 ms, 95% CI: 4.4 - 5.8 ; SNX-482: 4.2 ± 0.3 ms, 95% CI: 3.7 - 4.8 ; $p=0.0050$, paired Student's t-test), and a trend towards increased maximum time-derivative of voltage (control: 45.3 ± 4.9 mV/ms, 95% CI: 34.4 - 56.3 ; SNX-482: 74.3 ± 13.5 mV/ms, 95% CI: 47.0 - 101.5 , $p=0.0625$, paired Student's t-test, estimated from the phase-plane plot of in C). The latter is likely due to the recruitment of more voltage-gated Na^+ -channels during the AP onset from the more hyperpolarized interspike membrane potential (Guarina et al., 2018; Tomagra et al., 2019).

Source data provided in Figure 7-figure supplement 1-Source Data1.xlsx.

Legends to supplementary files

Supplementary file 1: Names, cellular functions and assay ID's of endogenous control genes.

For details see methods.

Supplementary file 2: TaqMan assays for β 1-4 isoforms and N-terminal β 2 splice variants including cDNA specific primer sequences for standard template cloning.

Additional Sall and HindIII restriction enzyme sites (see Methods) are underlined; the reverse (rev) primer used for standard template cloning including the HindIII restriction site was the same for β 2a-e subunit variants; rev, reverse; fwd, forward.

Supplementary file 3: Quantitative RT-PCR standard curve parameters.

SE-B, SE-Y, standard error of B and Y-intercept; Y-int., Y-intercept (CT value); R^2 , squared correlation coefficient; LOD, limit of detection (number of transcripts); LOQ, limit of quantification (number of transcripts); E (%), Efficiency in % ($E=10^{-1/\text{slope}-1}$), 100% efficiency corresponds to a slope of -3.32.

Supplementary file 4: Single cell gene expression data.

Data and statistics of genes as indicated for graphs shown in Figure 2-figure supplement 2A (middle) and B (right). n represents number of analyzed dopaminergic neurons derived from N individual mice. Significances according to two-way ANOVA followed by Tukey's multiple comparisons test: ***, $p < 0.001$.

Supplementary file 5: Multiplex PCR (outer) and nested PCR (inner) primers for qualitative PCR

F: forward primer, R: reverse primer

Supplementary file 6: Voltage-dependence of activation and inactivation of Cav1.3 co-transfected with α 2 δ 1 and different β -subunits in tsA-201 cells

All values are given as mean \pm SEM for the indicated number of experiments (n, N=2). Parameters were obtained as described in Materials and Methods from a holding potential of -89 mV using 15 mM Ca^{2+} as the charge carrier.

Voltage-dependence of gating: Parameters are as given in legend to Table 1. Statistical significance was determined using one-way ANOVA with Bonferroni post-hoc test ($V_{0.5}$, V_{rev} , act thresh, $V_{0.5,\text{inact}}$, k_{inact} , plateau) or Kruskal-Wallis followed by Dunn's multiple comparison

test (k). Statistical significances of post hoc tests are indicated for comparison vs. β_2a (*, **, ***) or vs. β_3 (§, §§, §§§): *** $p < 0.001$; ** $p < 0.01$; * $p < 0.05$.

Inactivation time course: The r values represent the fraction of I_{Ca} remaining after 50, 100, 250, 500, 1000 or 5000 ms during a 5-s pulse to V_{max} . Statistical significance was determined using one-way ANOVA with Bonferroni post-hoc test. Statistical significances of post hoc tests are indicated for comparison vs. β_2a : *** $p < 0.001$; ** $p < 0.01$; * $p < 0.05$).

Supplementary file 7: Inhibition of I_{Ca} in identified SN DA neurons of adult (12 weeks) mice by 100 nM SNX-482 and 10 μ M nifedipine (perforated-patch clamp)

For details see results. Experiments were performed as described in detail in the Methods section and Figure 6-figure supplement 1.

1706 **Tables**

β -subunit	Cav2.3 - Activation 2 mM Ca^{2+}						Cav2.3 - Inactivation 2 mM Ca^{2+}			
	$V_{0.5}$ [mV]	k [mV]	V_{rev} [mV]	act thres h [mV]	current density [pA/pF]	n	$V_{0.5, \text{inact}}$ [mV]	k_{inact} [mV]	plate au [%]	n
no β					-10.7 ± 1.1	23				
$\beta 2a$	-14.8 ± 1.2	4.8 ± 0.2	37.1 ± 0.9	-32.0 ± 0.9	-130.0 ⁺⁺⁺ ± 15.2	26	-40.6 ± 1.6	7.3 ± 0.5	0.4 ± 1.1	13
C3S/C4S $\beta 2a$	-13.9 ± 1.7	4.7 ± 0.3	38.2 ± 1.1	-30.9 ± 0.7	-105.7 ⁺⁺⁺ ± 21.4	12	-62.6 ^{***/###/SSS} ± 1.6	8.3 ^{##} ± 0.4	3.8 ± 1.6	9
$\beta 2d$	-15.9 ^s ± 1.1	4.6 ± 0.2	37.2 ± 1.1	-32.1 ^s ± 0.7	-107.7 ⁺⁺⁺ ± 13.4	17	-69.9 ^{***/###} ± 2.0	8.2 ^{##} ± 0.2	2.0 ± 0.7	10
$\beta 2e$	-14.1 ± 0.9	4.8 ± 0.2	40.3 [*] ± 0.6	-31.5 ± 0.7	-96.8 ⁺⁺⁺ ± 14.3	32	-39.9 ± 1.9	6.5 ± 0.3	3.8 ± 1.2	24
$\beta 3$	-10.5 ± 0.7	5.2 ± 0.2	39.8 ± 0.9	-29.2 ± 0.7	-64.6 ⁺⁺ ± 12.8	17	-76.2 ^{***/###} ± 1.0	7.0 ± 0.1	4.1 ± 0.7	14
$\beta 4$	-13.1 ± 0.7	5.0 ± 0.2	38.5 ± 0.5	-31.0 ± 0.5	-74.8 ⁺⁺⁺ ± 11.9	17	-70.3 ^{***/###} ± 1.2	7.5 ± 0.1	2.4 ± 0.4	11
Cav2.3 - 5 s Inactivation time course 2 mM Ca^{2+}										
β -subunit	r50 [%]		r100 [%]		r250 [%]		r500 [%]	r1000 [%]	r5000 [%]	n
$\beta 2a$	71.3 ± 2.1		52.4 ± 2.8		27.8 ± 2.9		14.3 ± 2.3	6.5 ± 1.2	1.3 ± 0.3	17
C3S/C4S $\beta 2a$	67.4 ^{SSS/%%} ± 5.2		47.3 ^{##/SSS/%%} ± 6.4		23.4 ^s ± 5.3		11.6 ± 3.3	6.2 ± 1.7	3.4 ± 1.1	11
$\beta 2d$	57.4 ^{*/###/SSS} ± 2.8		32.6 ^{***/###/SS} ± 2.4		11.3 ^{*/###} ± 1.7		4.4 ^{**/###} ± 0.9	2.4 ^{**/###} ± 0.6	1.7 ± 0.5	21
$\beta 2e$	77.5 ± 2.9		64.2 ± 3.3		41.1 ± 3.2		22.3 ± 2.8	10.1 ± 2.0	3.3 ± 0.8	27
$\beta 3$	32.9 ^{***/###} ± 2.9		14.2 ^{***/###} ± 1.5		6.1 ^{***/###} ± 1.0		4.4 ^{**/###} ± 0.7	2.9 [#] ± 0.5	1.6 ± 0.3	16
$\beta 4$	50.3 ^{***/###/SS} ± 2.7		27.1 ^{***/###} ± 2.5		8.6 ^{**/###} ± 1.4		3.7 ^{**/###} ± 0.8	2.0 ^{**/###} ± 0.5	1.0 ± 0.2	15

Table 1. Voltage-dependence of activation and inactivation, and time course of inactivation of Cav2.3 co-transfected with $\alpha 2\delta 1$ and different β subunits in tsA-201 cells.

All values are given as means \pm SEM for the indicated number of experiments (N = $\beta 2a$: 5; C3S/C4S $\beta 2a$, $\beta 2d$, $\beta 2e$: 2; $\beta 3$, $\beta 4$, no β : 3). Voltage-dependence of gating: $V_{0.5}$, Half-maximal activation voltage; k, slope factor; V_{rev} , estimated reversal potential; act thresh, activation threshold; $V_{0.5, \text{inact}}$, half-maximal inactivation voltage; k_{inact} , inactivation slope factor; plateau, remaining non-inactivating current. Near physiological recording conditions (2 mM Ca^{2+} , low 0.5 mM EGTA Ca^{2+} buffering) and calculation of the parameters of voltage-dependence of activation and inactivation are described in Materials and Methods. Statistical significance was determined using one-way ANOVA with Bonferroni post-hoc test ($V_{0.5}$, V_{rev} , $V_{0.5, \text{inact}}$, k_{inact} , plateau) or Kruskal-Wallis followed by Dunn's multiple comparison test (k, act thresh, current

1720 density). Statistical significances of post-hoc tests are indicated for comparison vs. $\beta 2a$ (*, **, ***), vs. $\beta 2e$ (#, ##, ###), vs. $\beta 3$ (§, §§, §§§) and vs. no β (+, ++, +++): $p < 0.05$, $p < 0.01$, $p < 0.001$.

1722 Inactivation time course: The r values represent the fraction of I_{Ca} remaining after 50, 100, 1723 250, 500, 1000 or 5000 ms during a 5 s pulse to V_{max} (voltage of maximal inward current). 1724 Statistical significance was determined using one-way ANOVA with Bonferroni post-hoc test 1725 (r100) or Kruskal-Wallis followed by Dunn's multiple comparison test (r50, r250, r500, r1000, 1726 r5000). Statistical significances of post hoc tests are indicated for comparison vs. $\beta 2a$ (*, **, 1727 ***), vs. $\beta 2e$ (#, ##, ###), vs. $\beta 3$ (§, §§, §§§) or vs $\beta 4$ (% , %% , %%%): $p < 0.05$, $p < 0.01$, $p < 0.001$.

1728 Source data provided in Table 1-Source Data 1.xlsx.

1729

Cav2.3 - recovery from inactivation 2 mM Ca ²⁺					
β -subunit	r100 [%]	r1500 [%]	r4000 [%]	r10000 [%]	n
β 2a	15.7 ±2.4	39.3 ±4.6	53.4 ±4.5	74.2 ±3.6	17
β 4	12.7 ±1.7	35.6 ±2.4	51.3 ±2.8	72.0 ±1.9	9

Table 2. Recovery from inactivation of Cav2.3 channels co-transfected with either β 2a or β 4 in combination with α 2 δ 1 in tsA-201 cells.

All values are presented as the mean \pm SEM for the indicated number of experiments (N=3).

The r values represent the fraction of recovered I_{Ca} after 100, 1500, 4000 or 10000 ms at -89 mV between depolarizations to V_{max} . No statistical significance was observed (unpaired Student's t-test).

Source data provided in Table 1-Source Data 1.xlsx.

	Activation			Inactivation		
	$V_{0.5,act}$ (95% CI) [mV]	k_{act} (95% CI) [mV]	n/N	$V_{0.5, inact}$ (95% CI) [mV]	k_{inact} (95% CI) [mV]	n/N
Control A (without Cav-blocker cocktail)	-37.8 (-39.3, -36.3)	9.17 (7.90, 10.6)	16/8	-52.7 (-53.9, -51.5)	10.5 (-11.6, -9.48)	16/8
+ Cav blocker cocktail ("R-type")	-29.9 (-30.8, -29.1)***	5.49 (4.73, 6.30)***	19/5	-47.5 (-48.7, -46.4)***	9.15 (-10.2, -8.16)	19/5
Control B (before SNX-482)	-34.4 (-35.7, -33.2)	9.68 (8.59, 10.8)	9/6	-52.9 (-53.7, -52.1)	9.30 (-10.9, -8.61)	9/6
SNX-482 - sensitive current	-34.9 (-37.7, -32.0)	10.6 (8.26, 13.3.)	9/6	-44.6 (-46.9, -42.2)***	10.1 (-12.1, -8.24)	9/6

Table 3. Voltage-dependence of activation and inactivation of Ca^{2+} -currents in SN DA neurons

Whole-cell voltage-clamp experiments to evoke Cav-currents were performed as described in Methods in SN DA neurons under control conditions (control A) or after preincubation with a Cav-blocker cocktail blocking all but R-type Cav channels (10 μ M Z941, 1 μ M isradipine, 1 μ M ω -conotoxin-MVIIC). In a second set of experiments, I_{Ca} steady-state current activation and inactivation parameters of individual SN DA neurons were first recorded in the absence (control B) and again after 10 min perfusion with 100 nM SNX-482. SNX-482-sensitive current parameters were obtained by subtracting currents in the presence of SNX-482 from the respective individual currents before drug wash-in. Voltages were not corrected for liquid junction potential (-5 mV). Data are given means \pm SEM. N: number of mice; n: number of recorded neurons. Pooled data from all experiments were fitted to the Boltzman equation. Statistically significant differences were determined by comparing fits using the extra sum of squares F-test (Prism 9.1): ***, $p < 0.001$, difference vs Control A; +++, $p < 0.001$ vs Control B). Source data provided in Table 1-Source Data 1.xlsx.

1756 **Source data files**

1757

1758 Figure 1-Source Data 1: Source data for data shown in Figure 1

1759 Figure 2-Source Data 1: Source data for data shown in Figure 2

1760 Figure 3-Source Data 1: Source data for data shown in Figure 3

1761 Figure 5-Source Data 1: Source data for data shown in Figure 5

1762 Figure 6-Source Data 1: Source data for data shown in Figure 6

1763 Figure 7-Source Data 1: Source data for data shown in Figure 7

1764

1765 Figure 1-figure supplement 2-Source Data 1: Source data for data shown in Figure 1-figure
1766 supplement 2

1767 Figure 2-figure supplement 1-Source Data 1: Source data for data shown in Figure 2-figure
1768 supplement 1, panels B and C

1769 Figure 2-figure supplement 2-Source Data1: Source data for data shown in Figure 2-figure
1770 supplement 2, panels A and B

1771 Figure 6-figure supplement 1-Source Data 1: Source data for data shown in Figure 6-figure
1772 supplement 1, panels C, D and G, H

1773 Figure 7-figure supplement 1-Source Data 1: Source data for data shown in Figure 7-figure
1774 supplement 1, panel B

1775

1776 Table 1-Source Data 1: Source data for data shown in Table 1

1777 Table 2-Source Data 1: Source data for data shown in Table 2

1778 Table 3-Source Data 1: Source data for data shown in Table 3

1779

1780

1781 **Source data 1 files**

1782 Original images:

1783 Figure_2_CI_original: original image file used in Figure 2, panel C

1784 Figure_2_Cr_original: original image file used in Figure 2, panel C

1785 Figure_6_C_BF_original: original image file used in Figure 6, panel C

1786 Figure_6_C_NB_original: original image file used in Figure 6, panel C

1787 Figure_6_C_TH_NB_original overlay: original image file used in Figure 6, panel C

1788 Figure_6_C_TH_original: original image file used in Figure 6, panel C

1789 Figure_1-figure supplement 1_BI_original: original image file used in Figure 1-figure
1790 supplement 1, panel B (left)

1791 Figure_1-figure supplement 1_BI_original_labelled: original image file used in Figure 1-figure
1792 supplement 1, panel B (left) with all gel lanes labeled; lanes selected for the figure are

1793 indicated

1794 Figure_1-figure supplement 1_Br_original: original image file selected for the Figure 1-figure
1795 supplement 1, panel B (right)

1796 Figure_1-figure supplement 1_Br_original-labelled: original image file used in Figure 1-figure
1797 supplement 1, panel B (right) with all gel lanes labeled; lanes displayed in the figure are
1798 indicated

1799 Figure_2-figure supplement 2_All_original: original image file used in Figure 2-figure
1800 supplement 2, panel A (lower, left)

1801 Figure_2-figure supplement 2_Alr_original: original image file used in Figure 2-figure
1802 supplement 2, panel A (lower right)

1803 Figure_2-figure supplement 2_Aul_original: original image file used in Figure 2-figure
1804 supplement 2, panel A (upper left)

1805 Figure_2-figure supplement 2_Aur_original: original image file used in Figure 2-figure
1806 supplement 2, panel A (upper right)

1807 Figure_2-figure supplement 2_B_THu_original original image file used in Figure 2-figure
1808 supplement 2, panel B (upper)

1809 Figure_2-figure supplement 2_B_beta2a_original: original image file used in Figure 2-figure
1810 supplement 2, panel B (upper)

1811 Figure_2-figure supplement 2_B_THu_beta2a_merge_original: original image file used in
1812 Figure 2-figure supplement 2, panel B (upper)

1813 Figure_2-figure supplement 2_B_THl_original: original image file used in Figure 2-figure
1814 supplement 2, panel B (lower)

1815 Figure_2-figure supplement 2_B_beta2e_original: original image file used in Figure 2-figure
1816 supplement 2, panel B (lower)

1817 Figure_2-figure supplement 2_B_THl_beta2e_merge_original: original image file used in
1818 Figure 2-figure supplement 2, panel B (lower)

1819 Figure_6_figure_supplement_1_J_1: original image file used in Figure 6-figure supplement 1,
1820 panel J to generate merged image

1821 Figure_6_figure_supplement_1_J_2: original image file used in Figure 6-figure supplement 1,
1822 panel J to generate merged image

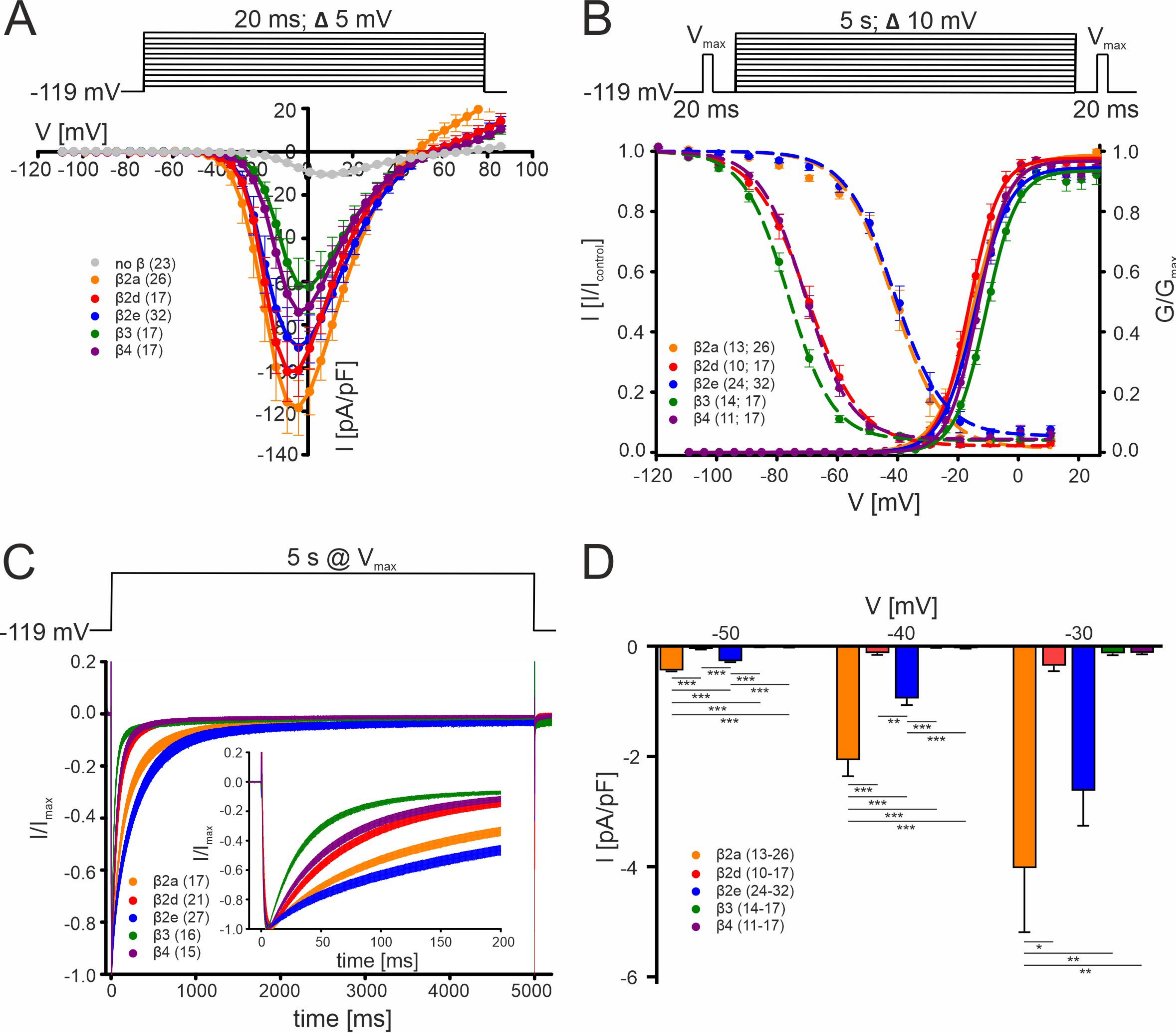


Figure 1

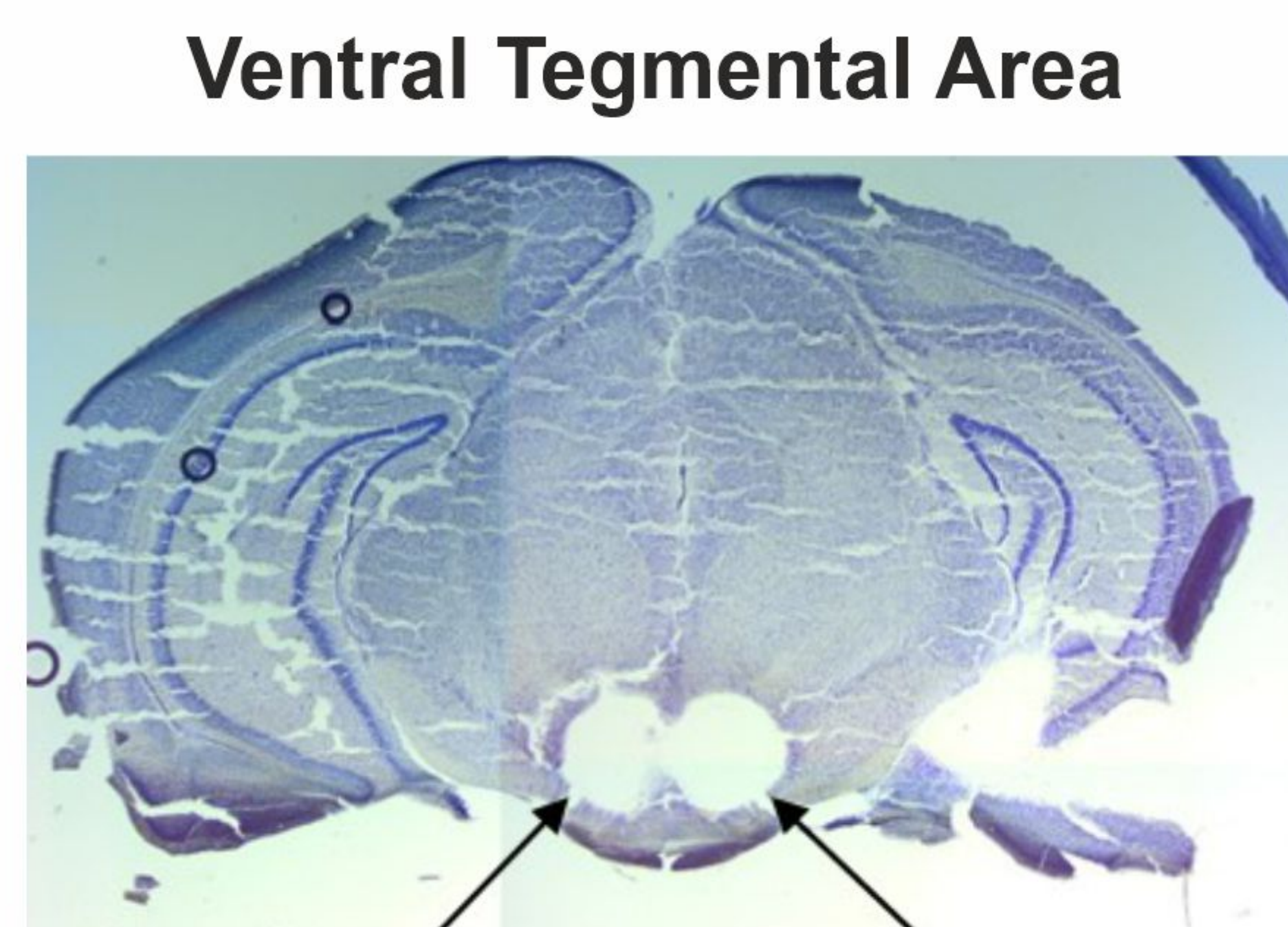
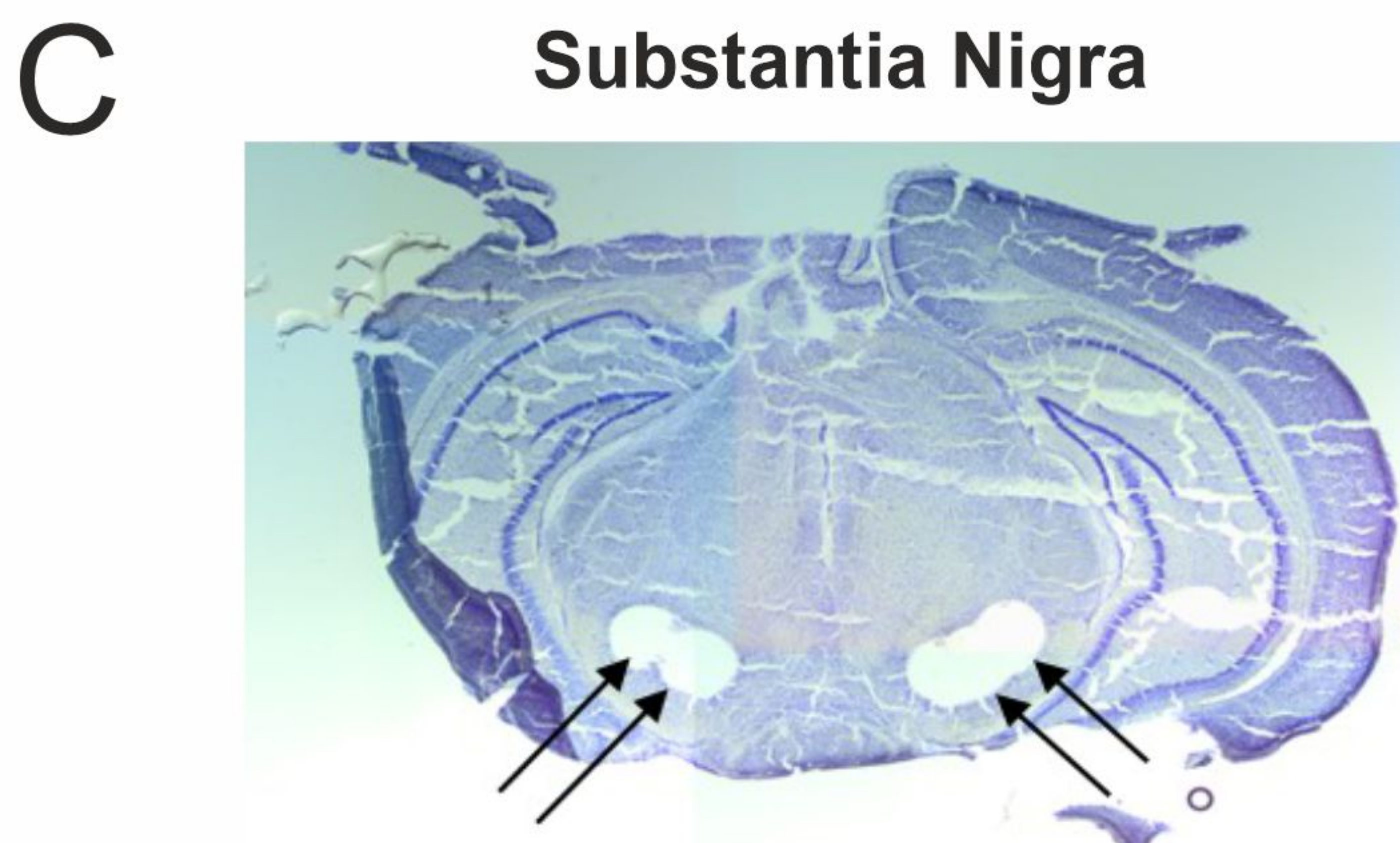
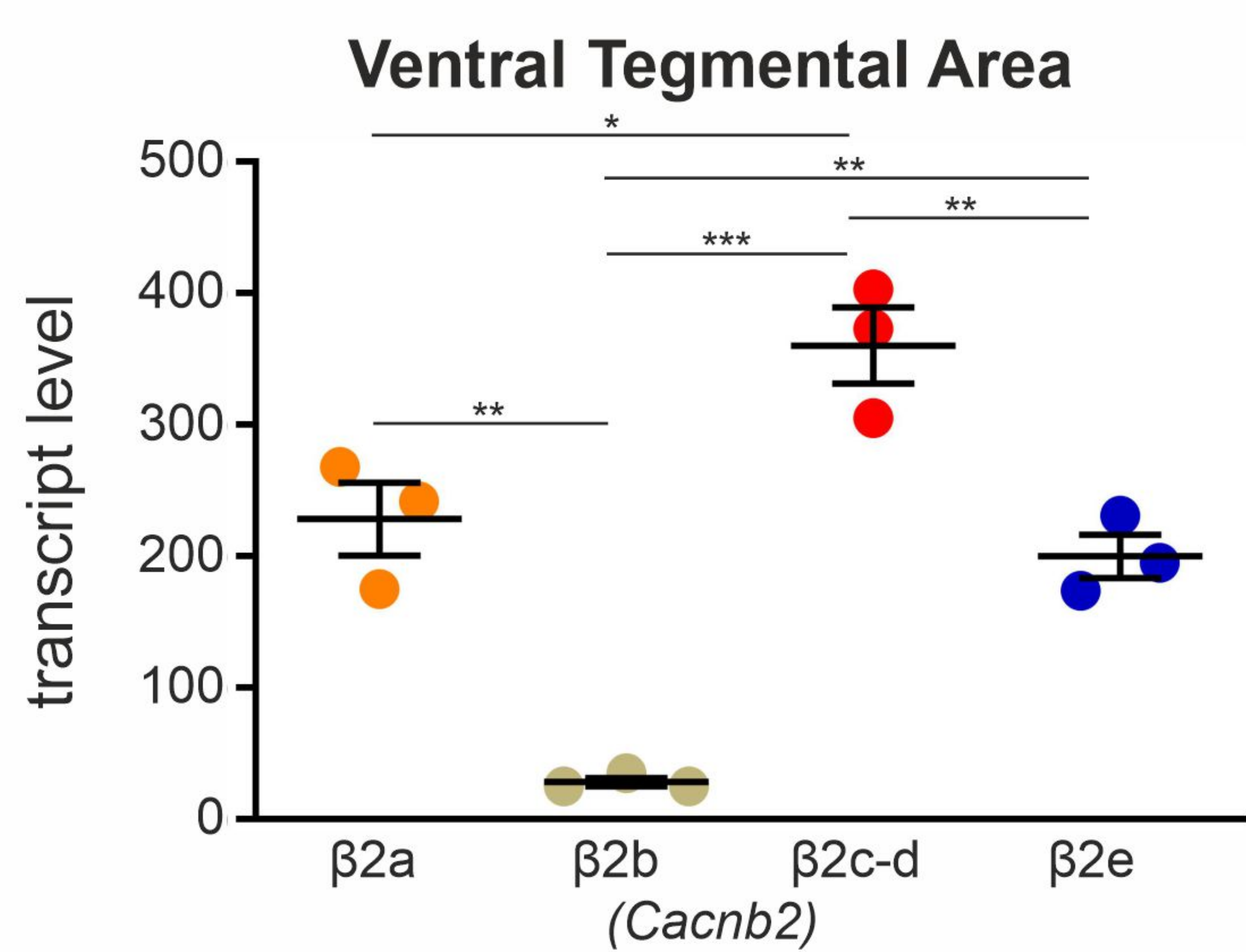
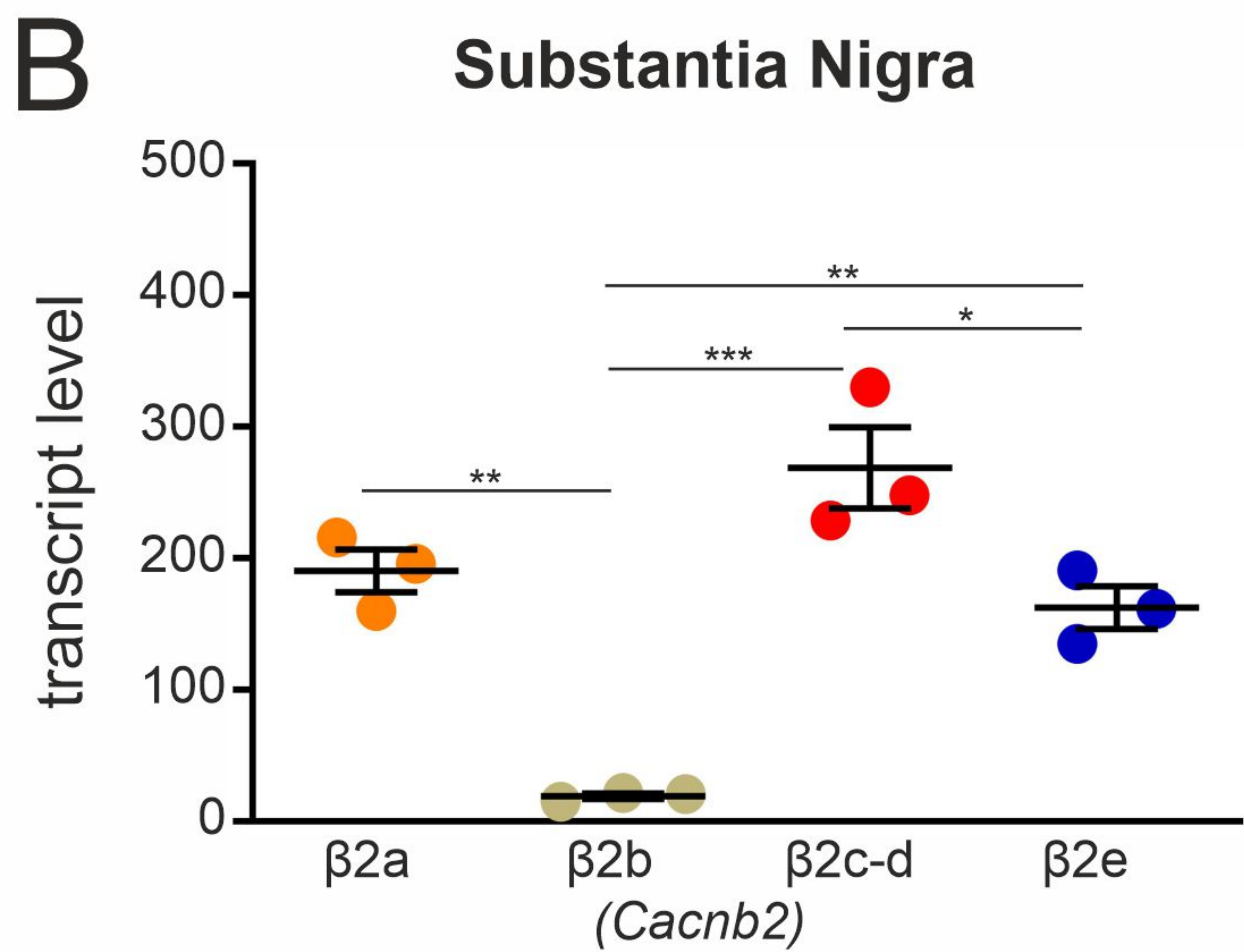
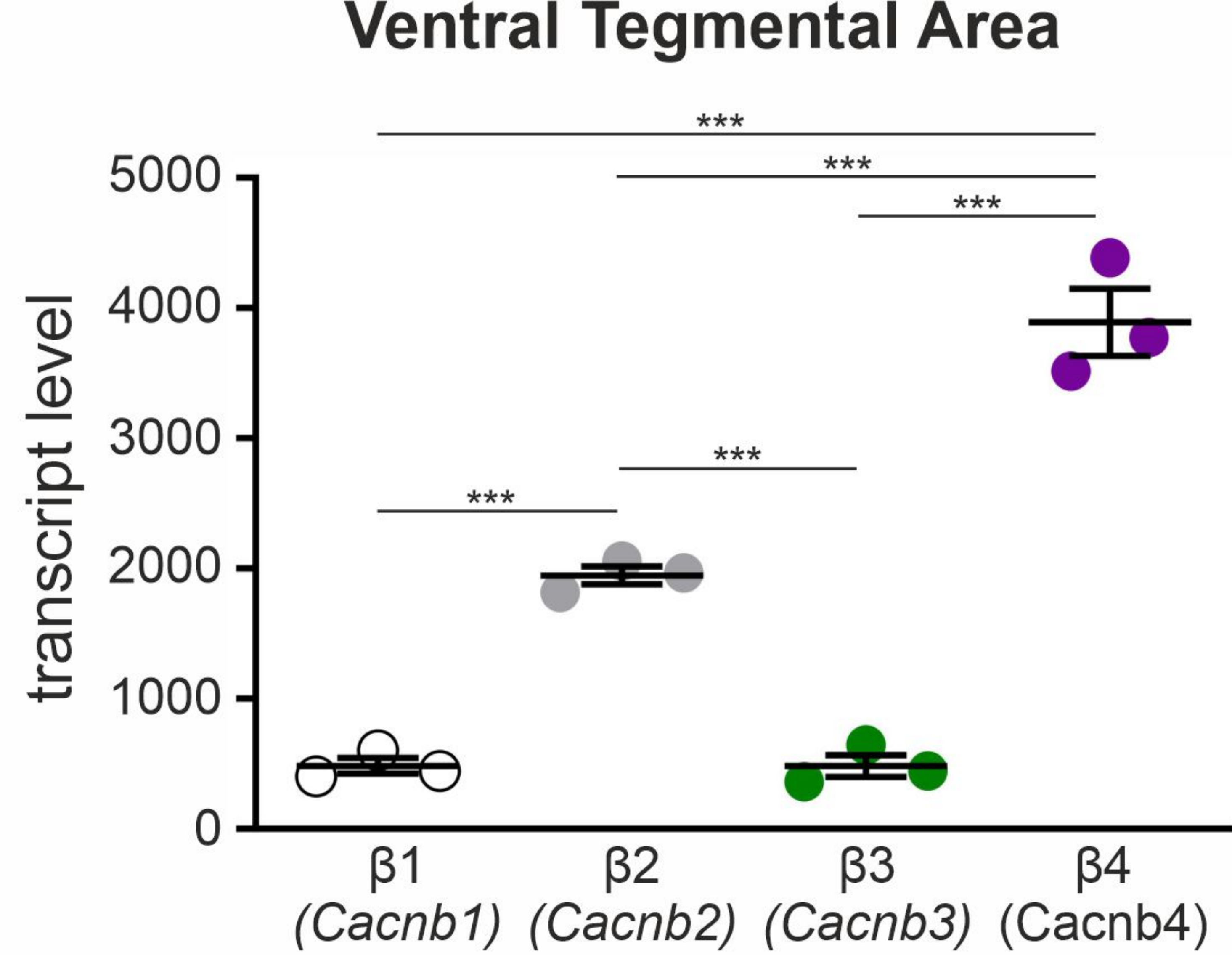
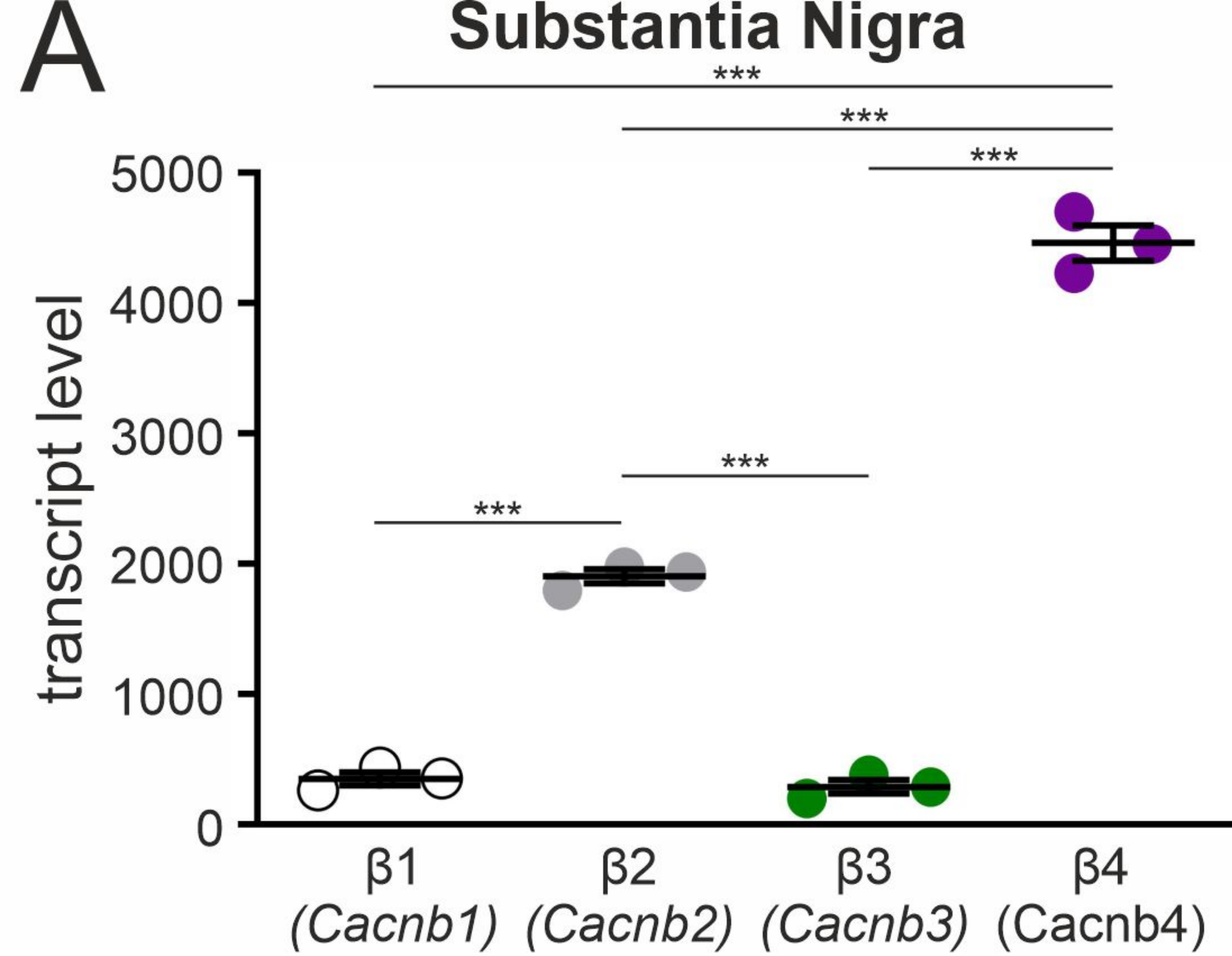


Figure 2

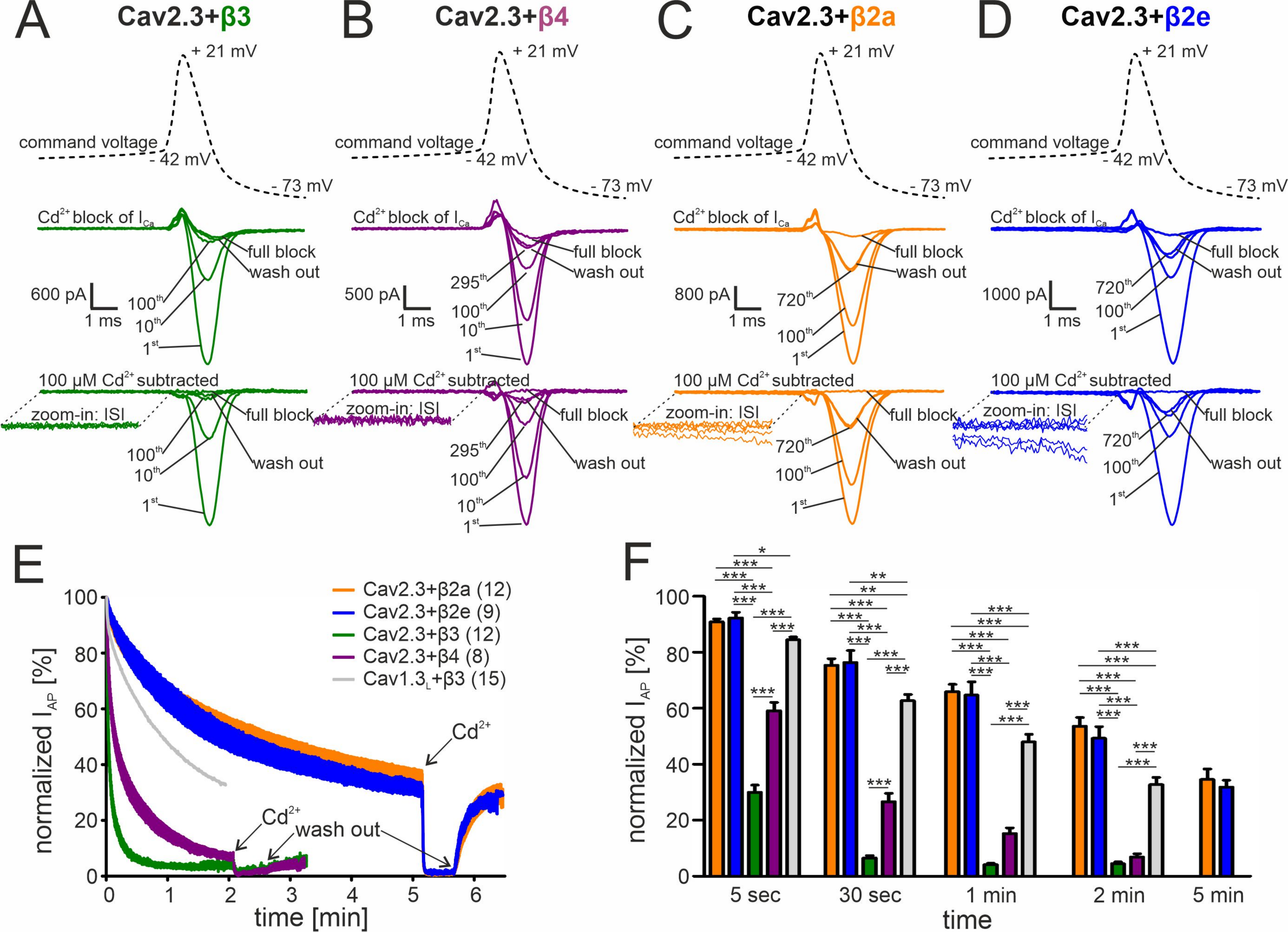


Figure 3

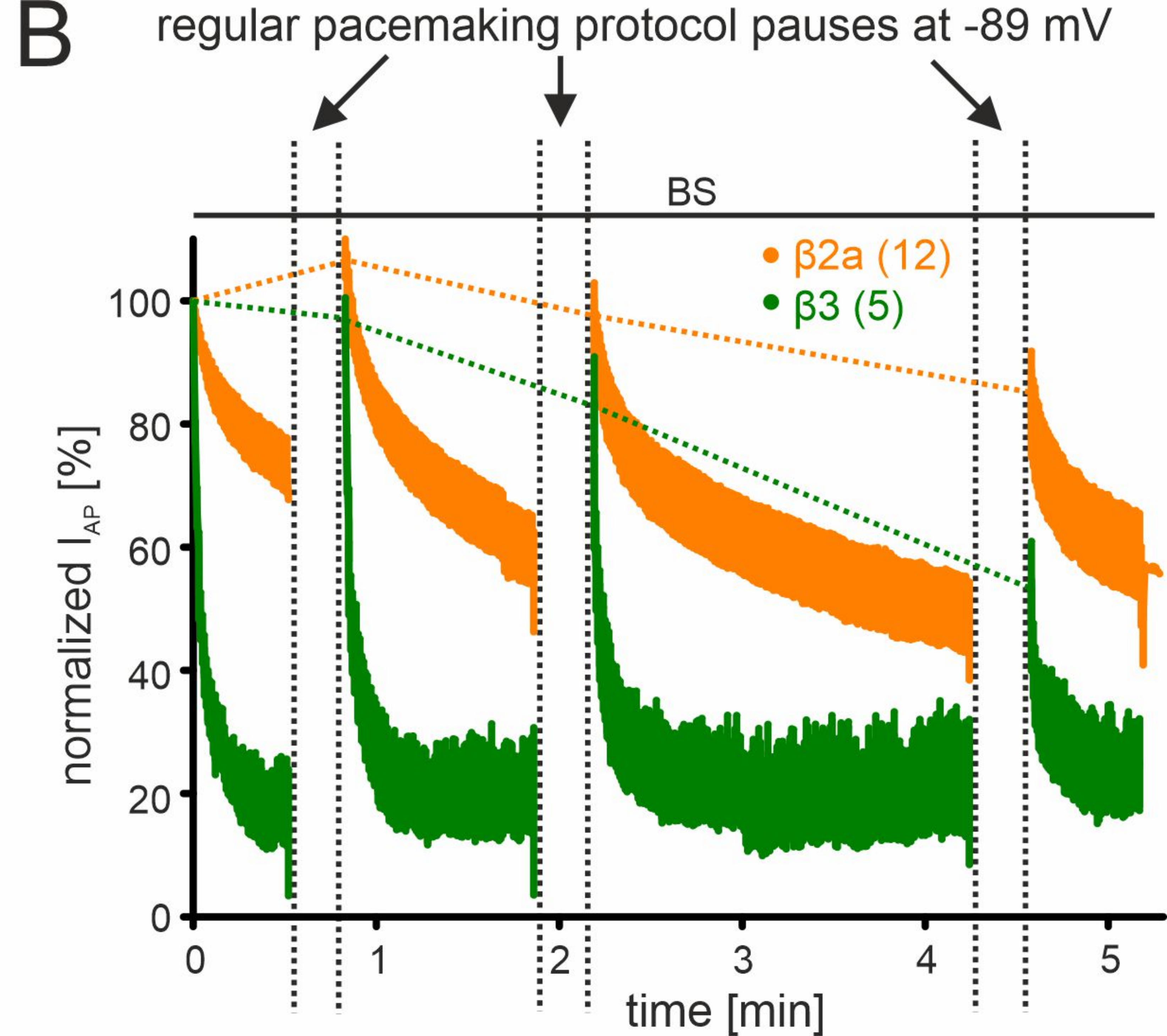
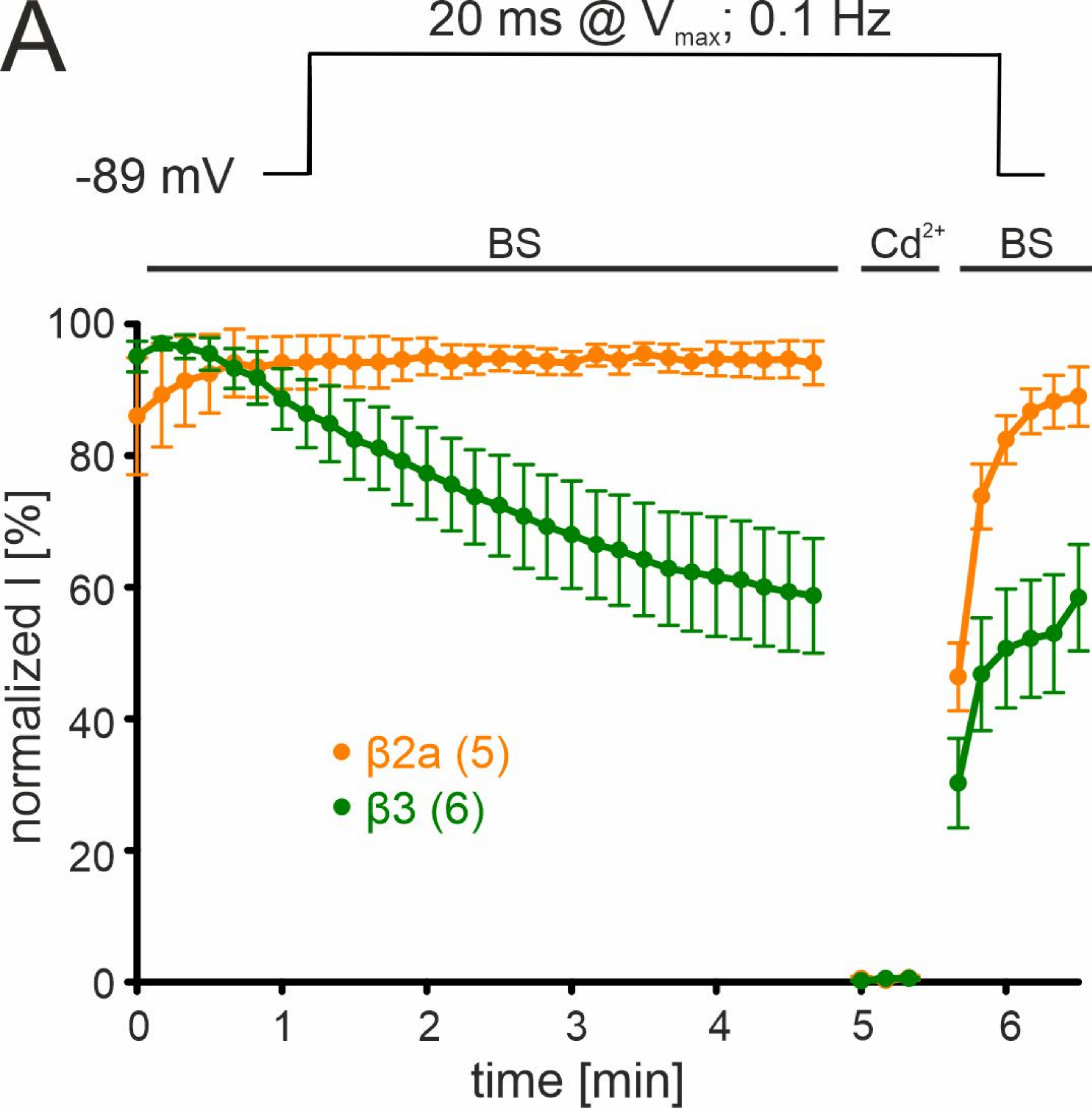


Figure 4

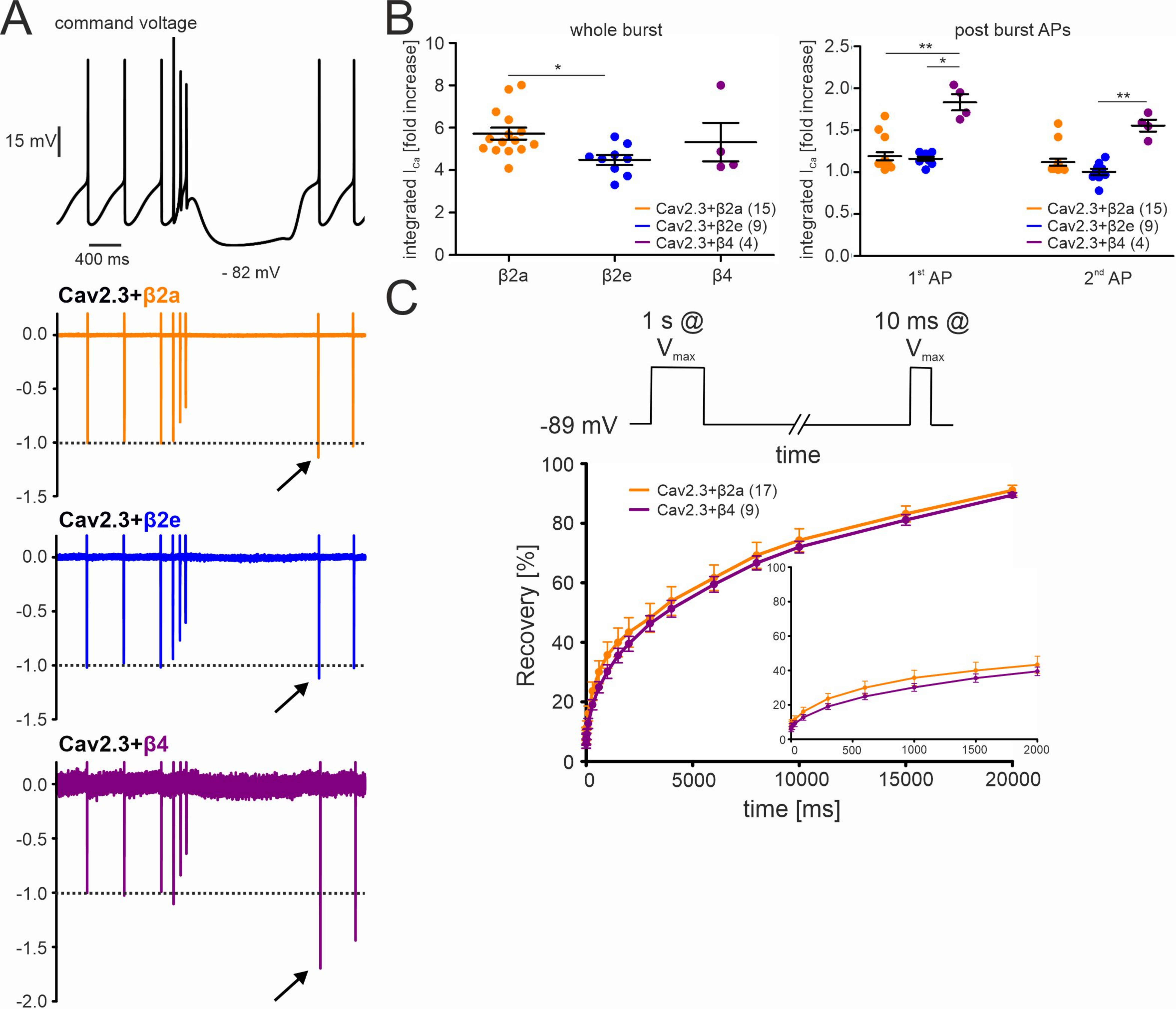


Figure 5

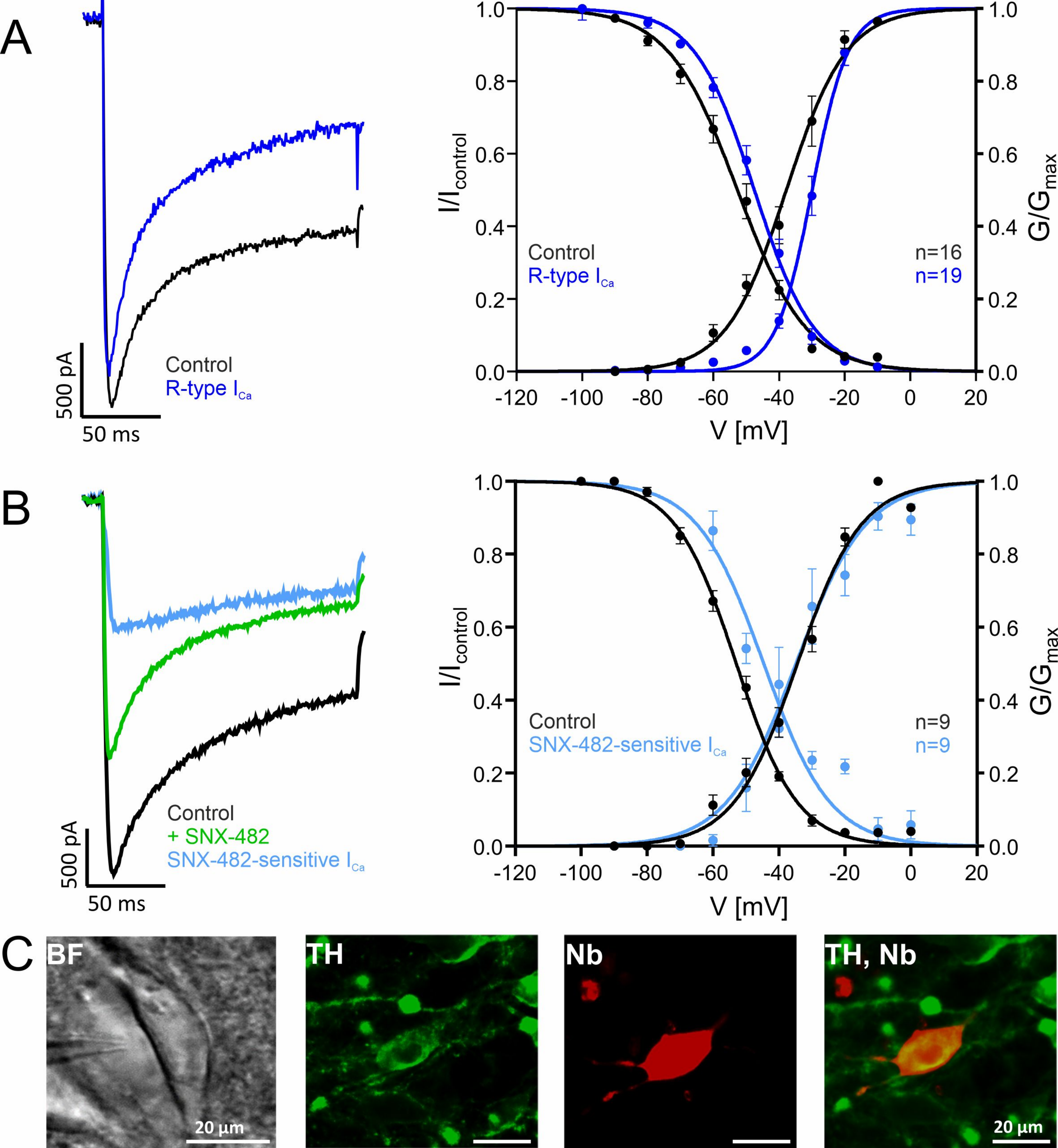


Figure 6

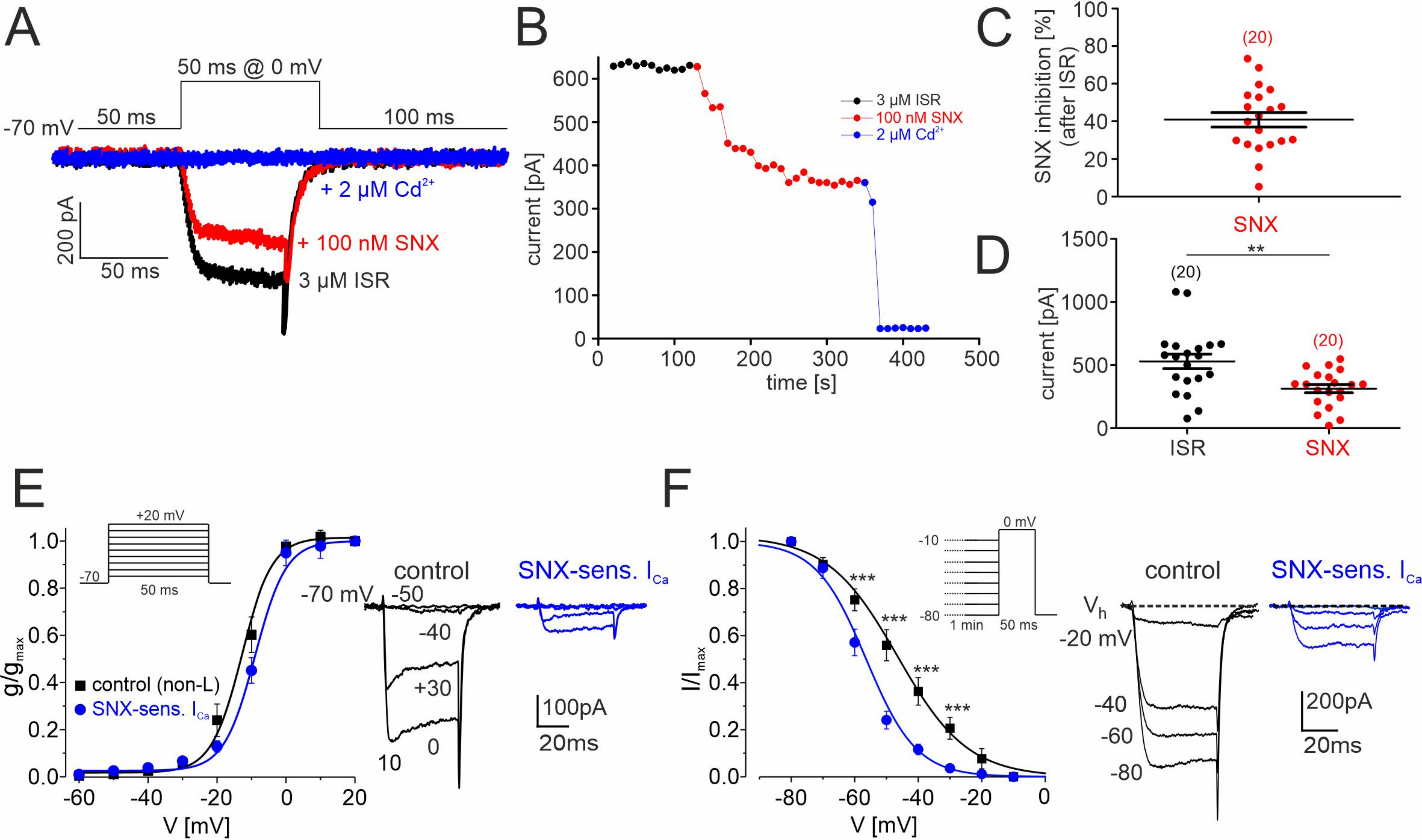


Figure 7

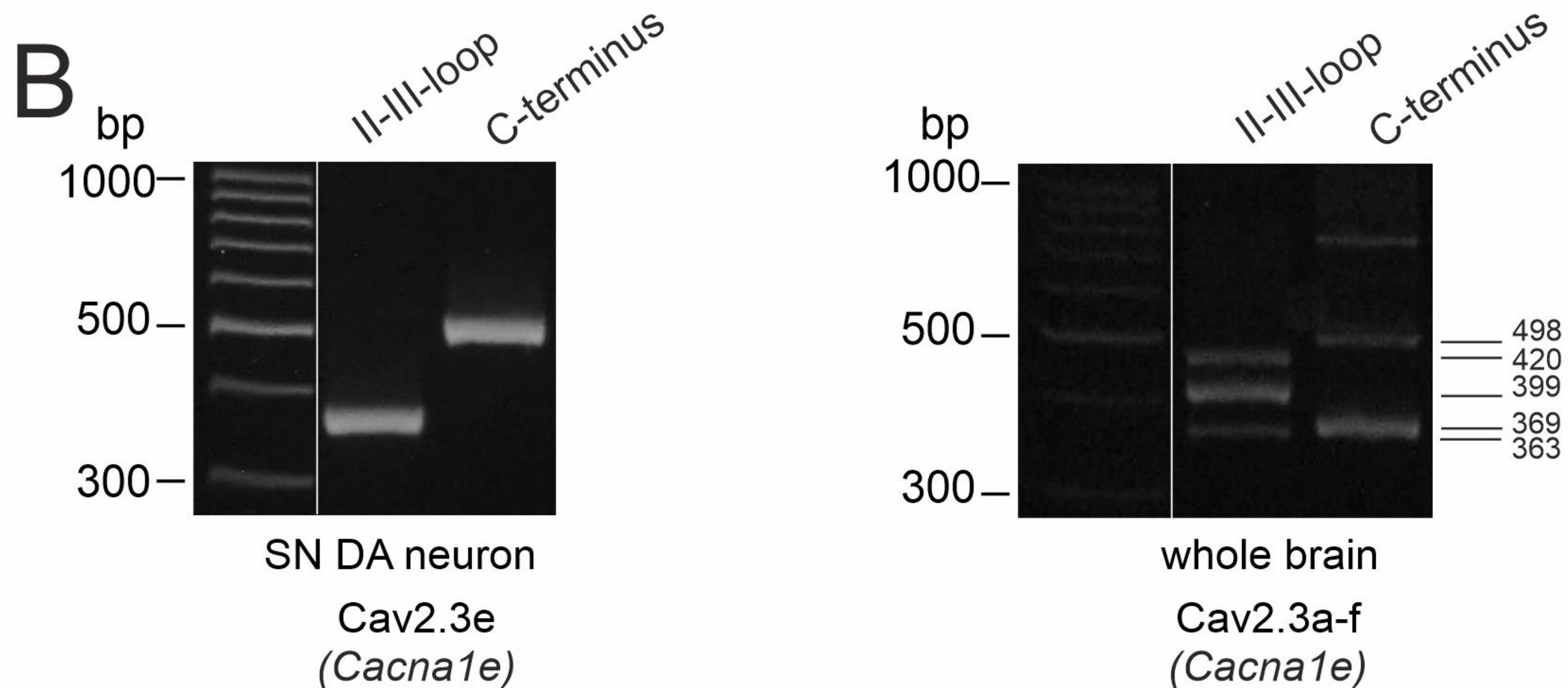
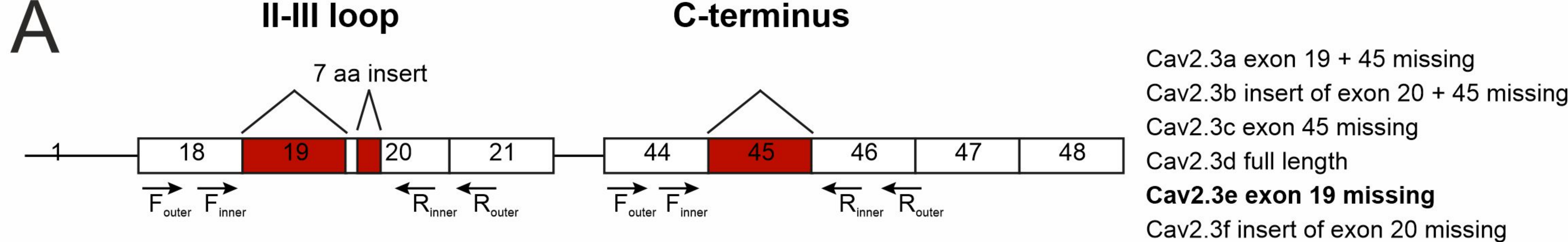


Figure 1-figure supplement 1

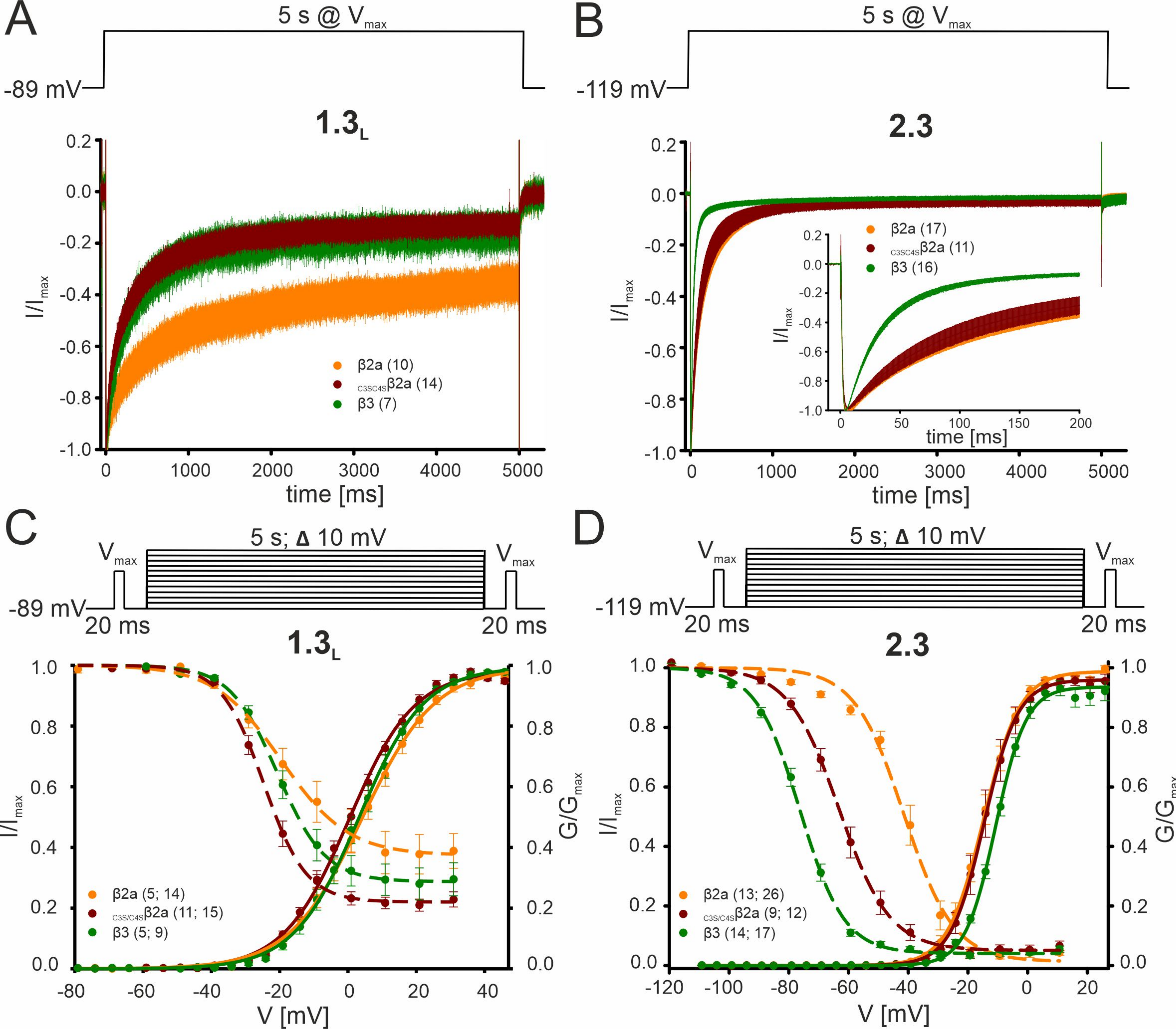


Figure 1-figure supplement 2

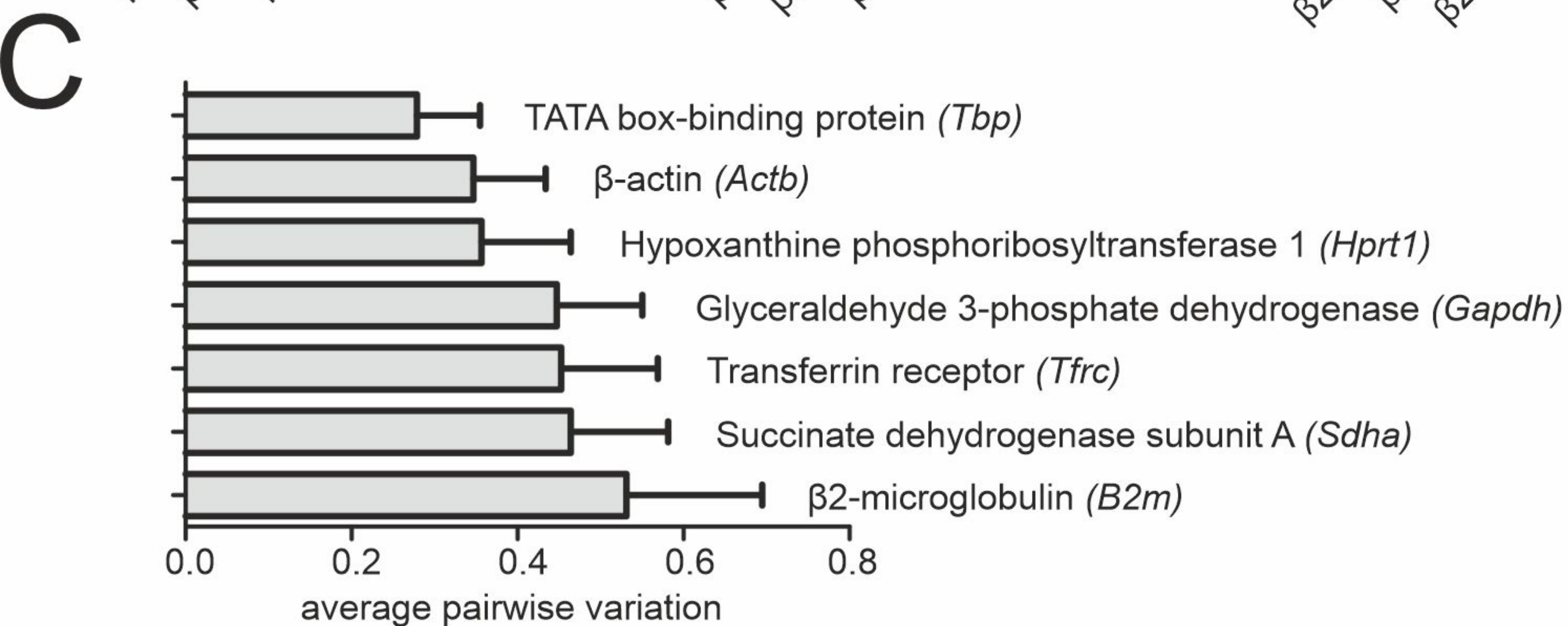
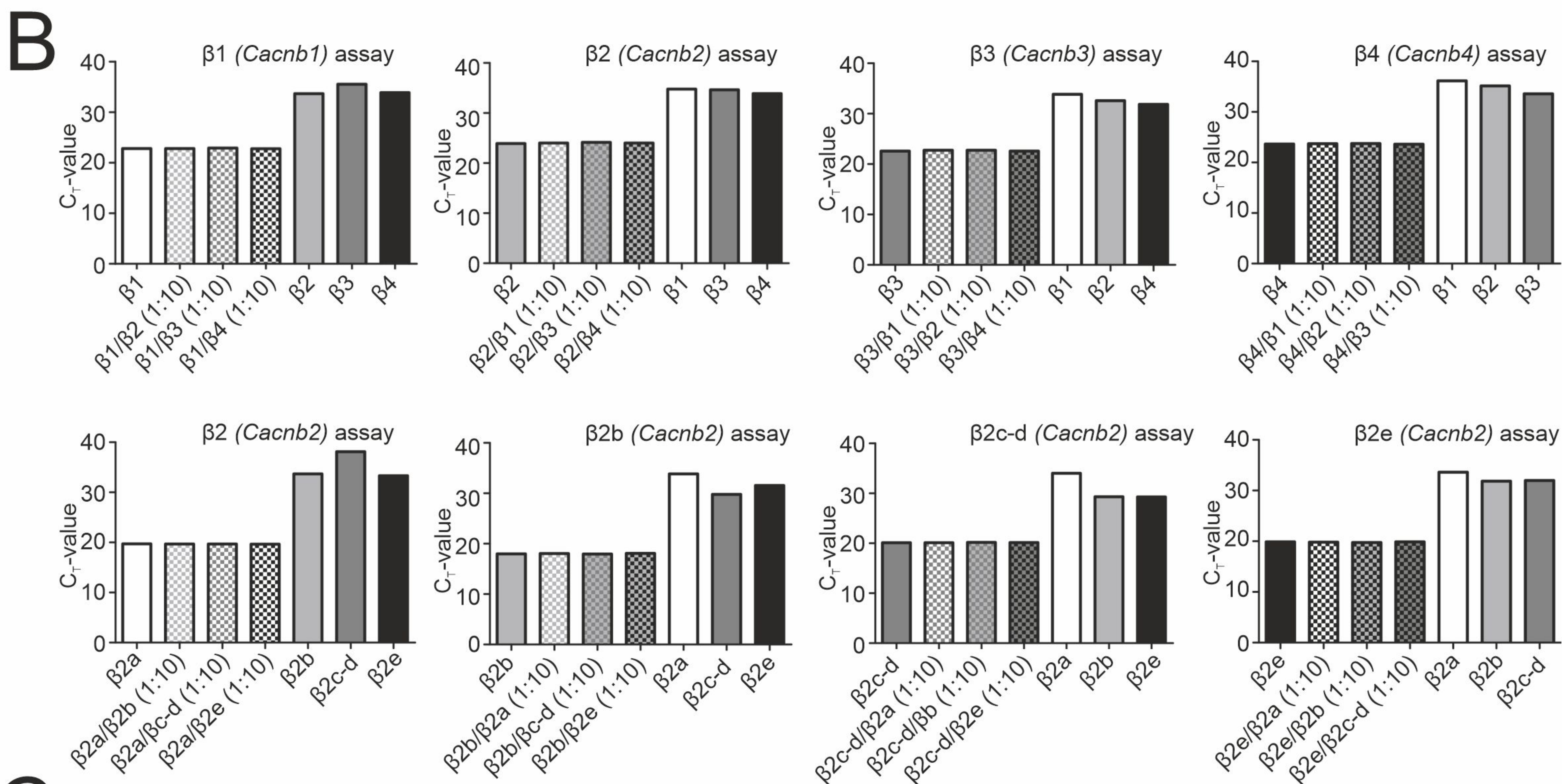
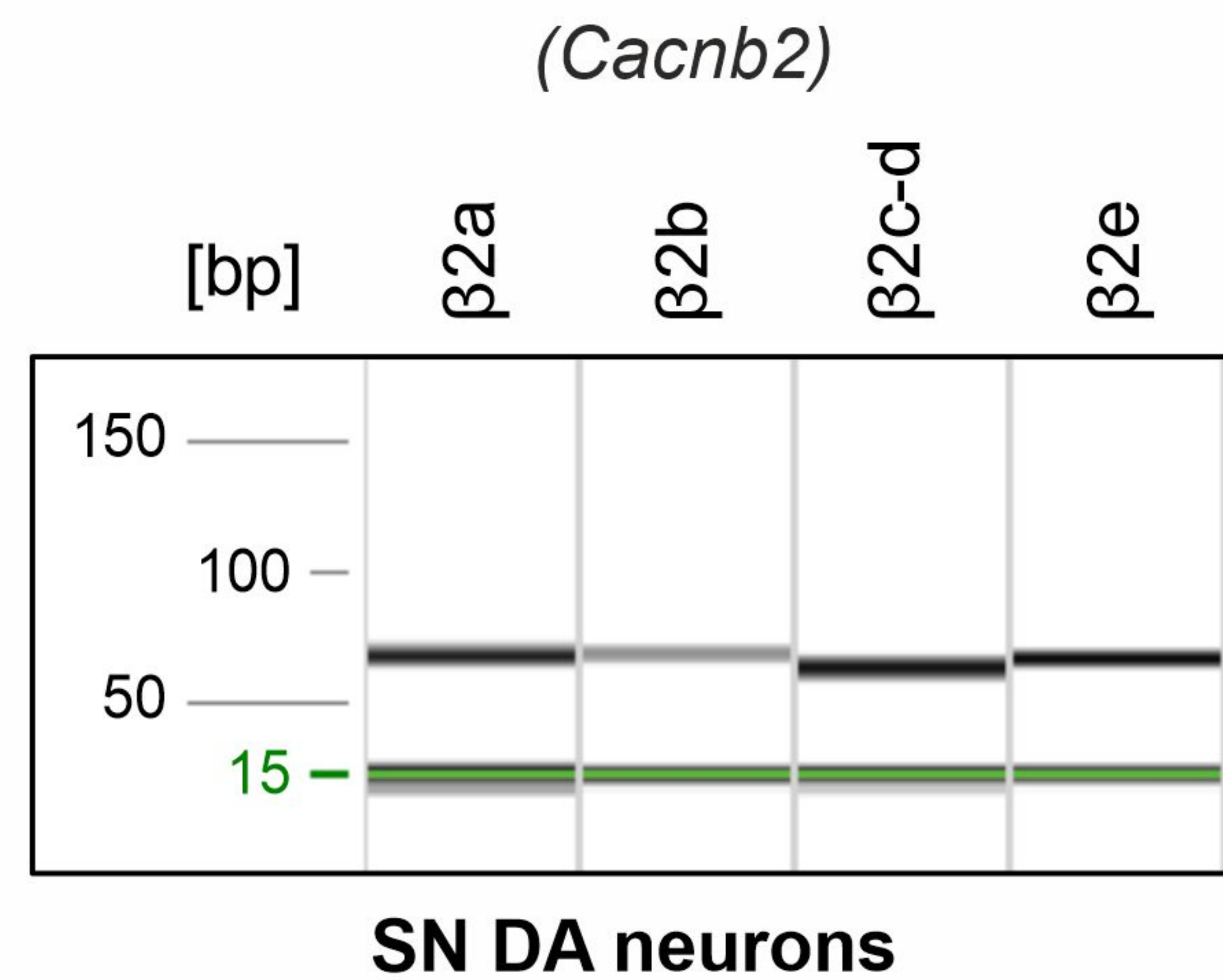
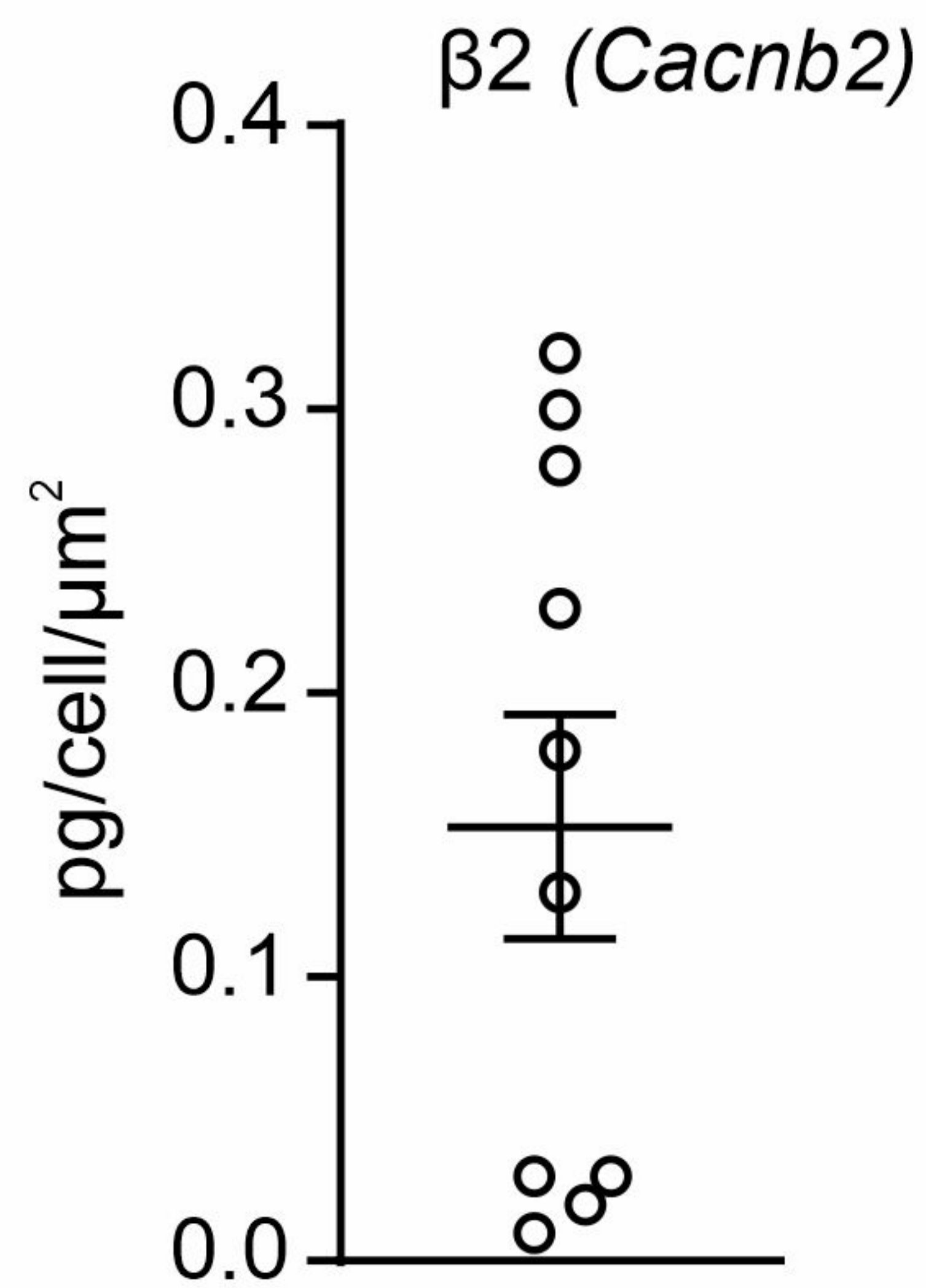
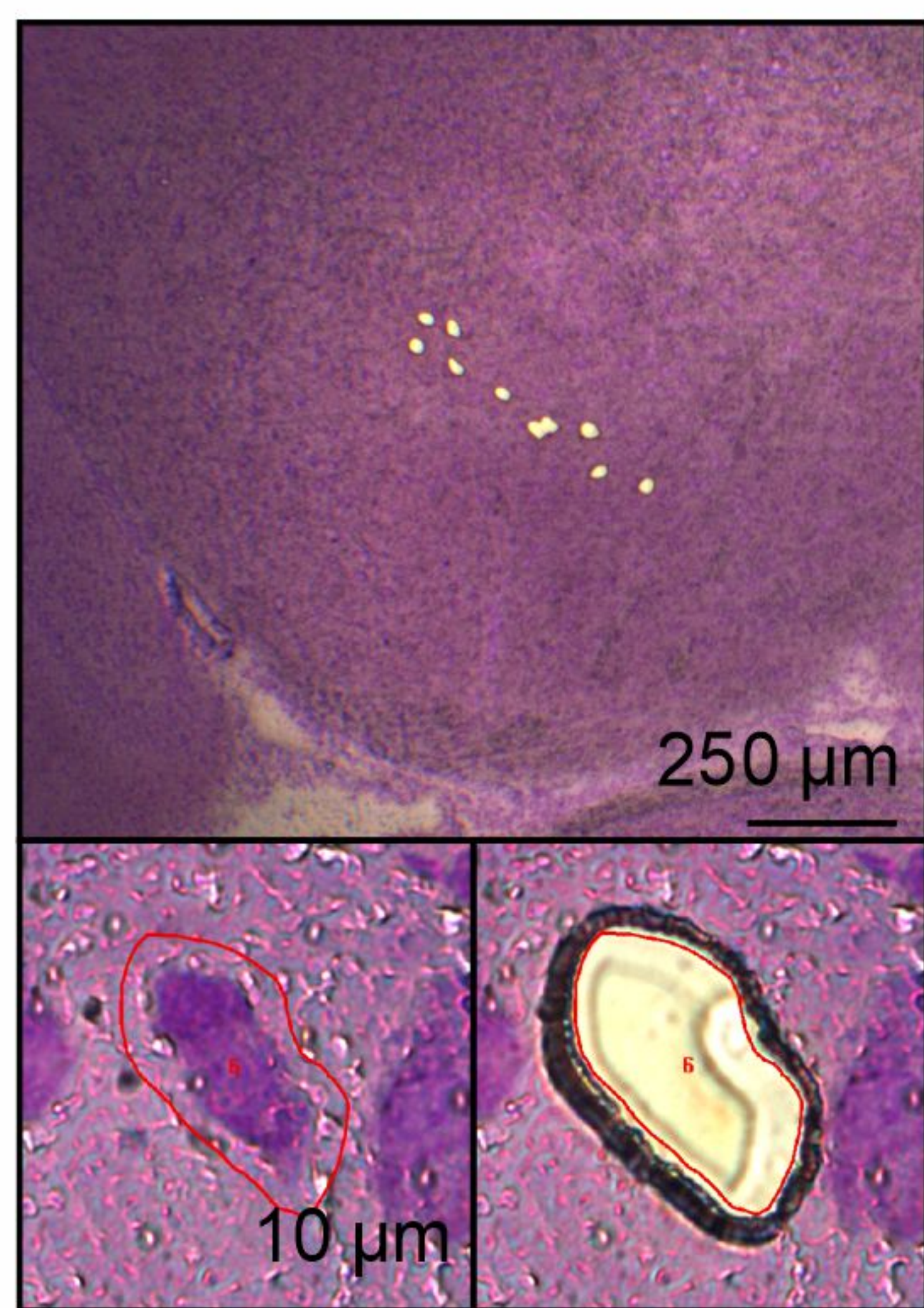


Figure 2-figure supplement 1

A



B

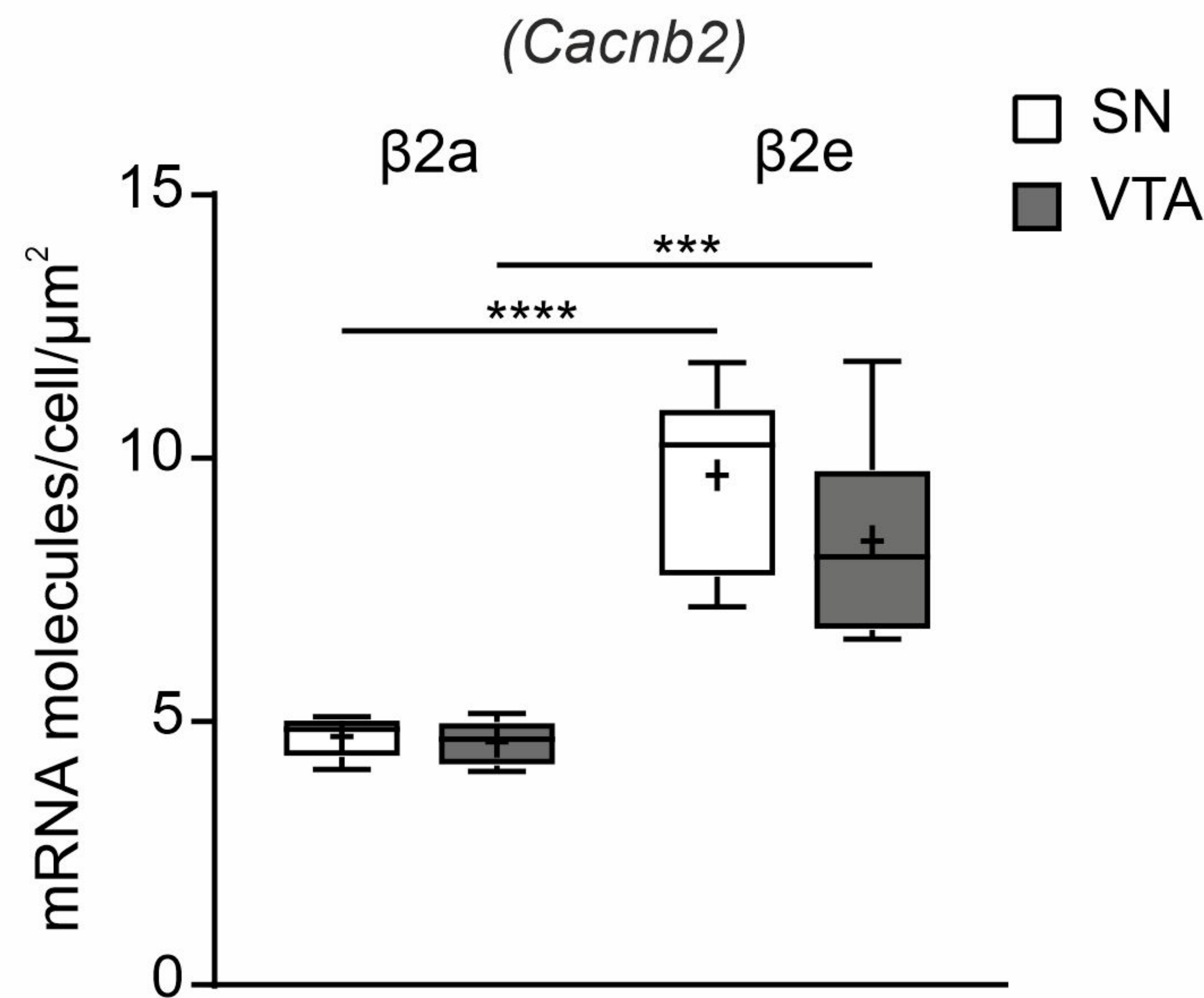
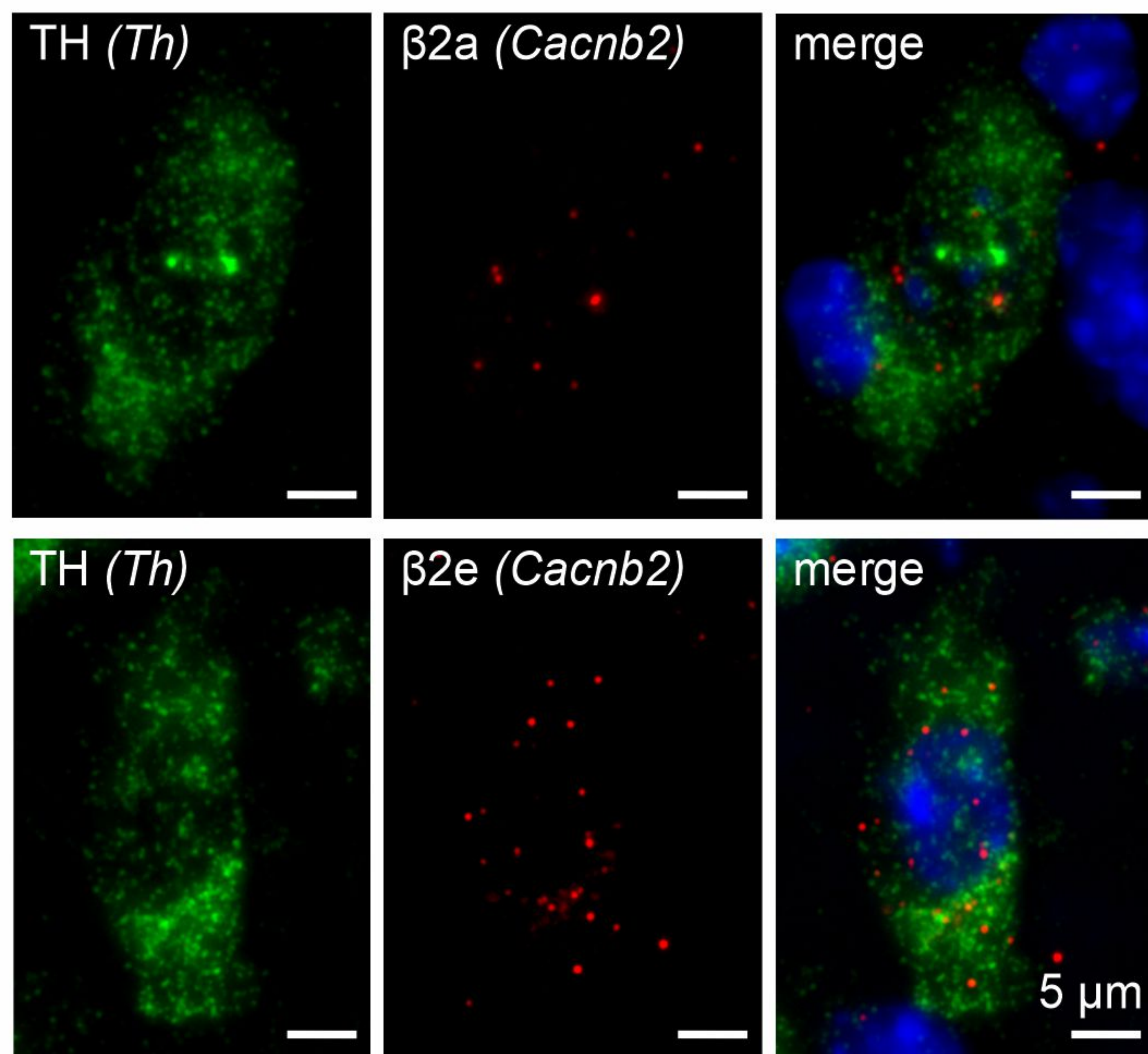


Figure 2-figure supplement 2

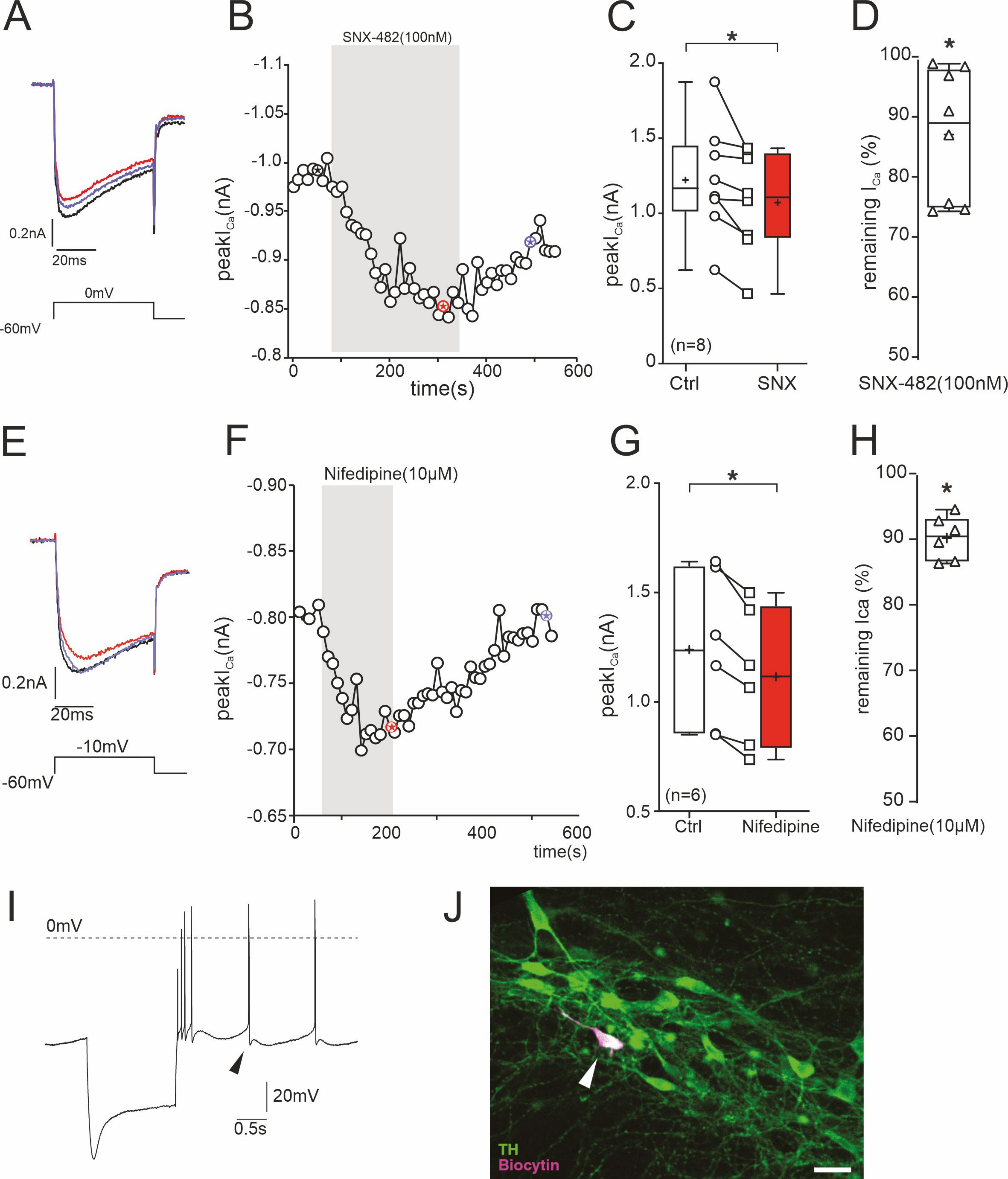


Figure 6-figure supplement 1

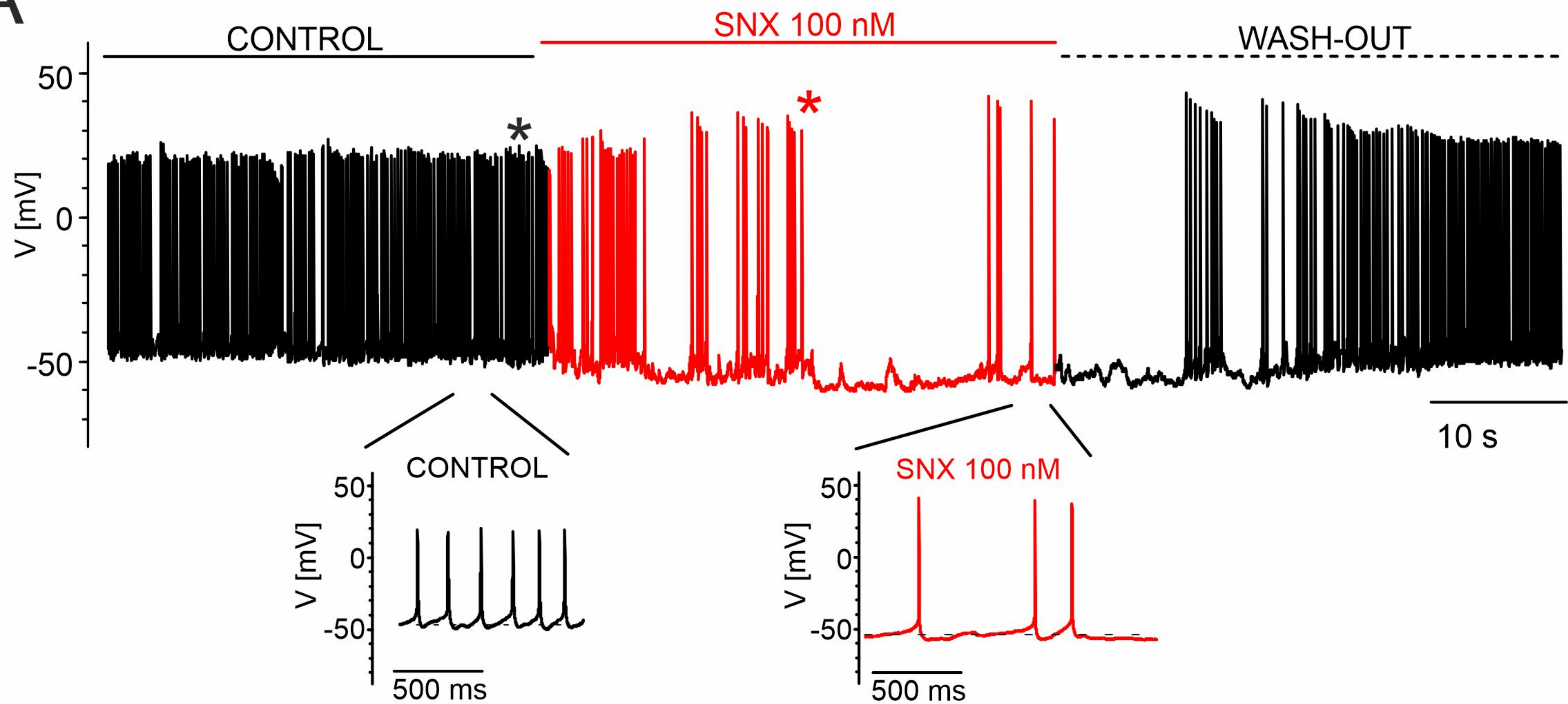
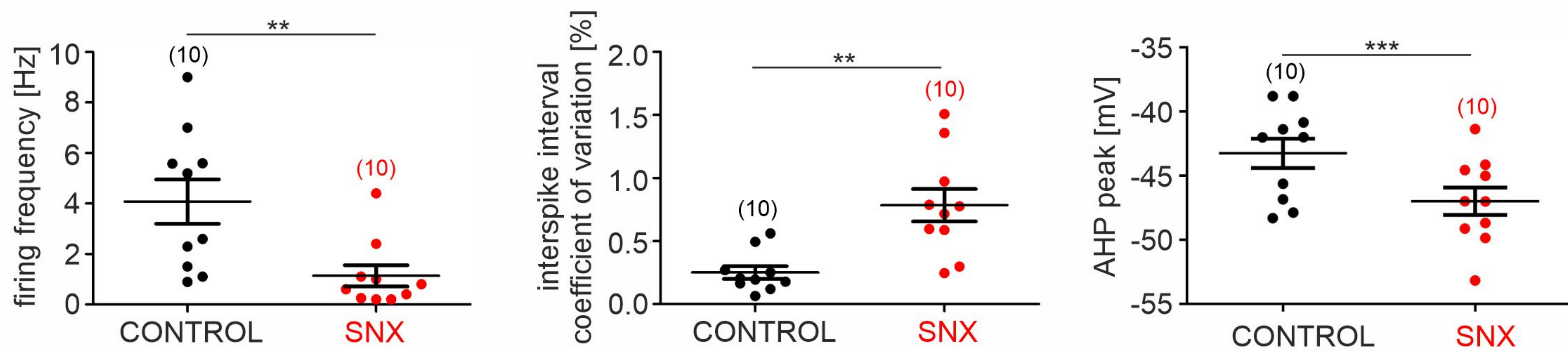
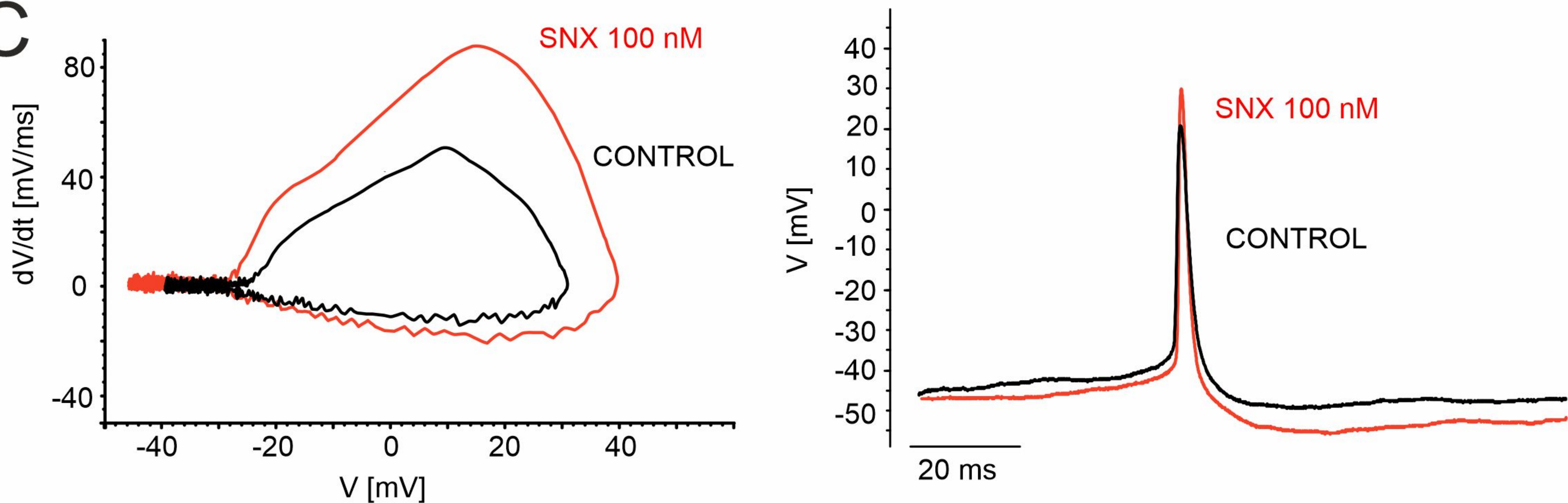
A**B****C**

Figure 7-figure supplement 1